Doctoral Dissertation
Doctoral Program in Energy Engineering (31st Cycle)

Moving forward the thermal-hydraulic modeling of superconducting magnets for ITER: from the Insert Coils to the full magnets

By

Alberto Brighenti

******

Supervisor:
Prof. L. Savoldi, Supervisor

Doctoral Examination Committee:

Prof.
Prof.
Prof.
Prof.
Prof.

Politecnico di Torino
2019

Declaration

I hereby declare that, the contents and organization of this dissertation constitute my own original work and does not compromise in any way the rights of third parties, including those relating to the security of personal data.

Alberto Brighenti

2019

This work has been carried out within the framework of the EUROfusion Consortium and has received funding from the Euratom research and training programme 2014-2018 under grant agreement No 633053. The views and opinions expressed herein do not necessarily reflect those of the European Commission.

The views and opinions expressed herein do not necessarily reflect those of the ITER Organization.

* This dissertation is presented in partial fulfilment of the requirements for **Ph.D. degree** in the Graduate School of Politecnico di Torino (ScuDo).

A Manu, Robi e Laura

Acknowledgements

First, I want to thank my mother, my father, my brother and sisters for their support and understanding during these years, despite the distance separating us.

I would like to thank also my supervisor, Laura, who was the first to believe in me starting from MSc and lately during my entire PhD experience, and Prof. Zanino, whose guidance and expertise helped me to learn and improve my work.

Then, I want to thank all PhD and MSc students I had the opportunity to meet: Stefano, Antonio, Dominic, Siew Sin, Andrea B., Mattia, Andrea Z., Haosheng, Valerio, Pietro, Domenico and Giulia. Thank you also to my office-mates: Giuseppe, Nicolò F., Nicolò A. for the casual breaks used to escalate quickly.

A very special thank is deserved to Roberto, thank for your guidance, advice, support and for being there every day of these three long years. You motivated me when I wanted to give up. I will not forget it.

Finally, I want to thank Manuela, my love and my teammate. During these years, you helped me to stand up and you remembered me the reason to never give up, even in the darkest days. Everything is less hard when you are with me.

Happiness is real only when shared (Christopher McCandless)

Abstract

The International Thermonuclear Experimental Reactor, known as ITER ("the way", in latin) will be the largest superconducting tokamak of the world. It is currently being built in Cadarache, France, and it aims at becoming the first large scale superconducting nuclear fusion reactor to overcome the main challenges faced by the achievement of fusion energy. After the ITER prototype, according to the European roadmap towards electricity form fusion, the next step of fusion research is the development of EU DEMO, the demonstrator which should prove the capability to produce electricity from a fusion power plant on a commercial scale. Due to the huge costs of technology research for fusion, in order to cap the budget, engineers aim at developing optimized computational tools, needed to support the design activities and predict the operation of complex systems never built before.

For example, in superconducting tokamaks like ITER and the EU DEMO, some of the most expensive and complex components are the magnets, which must be built and operated with very tight tolerances and thus their design requires reliable and detailed computational tools. In this framework, the Cryogenic Circuit Conductor and Coil (4C) code, developed at Politecnico di Torino, is the state-of-the-art tool for the thermal-hydraulic analysis of superconducting magnets for fusion application. The code was born in late 2009 to simulate the thermal-hydraulics of the ITER superconducting magnets. In the successive years, the 4C code has been successfully validated against data collected during various experiments, including the ITER Toroidal Field Model Coil (TFMC) and Central Solenoid Model Coil (CSMC), the ITER Insert coils, namely the Central Solenoid, the Poloidal Field insert coils, and more recently, the Toroidal Field insert. In addition to these validation exercises, the code has been used for the thermal-hydraulic analysis of other

magnets, like those of the W7-X, EAST, KSTAR, JT-60SA and the EU DEMO tokamaks.

In this work, the 4C code is used for the analysis of the experimental data collected during the experimental campaigns on the ITER insert coils performed in the last four years. The tests have been carried out in conditions fully relevant for the ITER superconducting magnets operation, thus allowing to challenge the numerical tools in a relevant setup and deduce the constitutive relations for thermal-hydraulic, electromagnetic and thermos-electrical phenomena. The developed models for the Central Solenoid Insert and Toroidal Field Insert coils are used in a series of successful validation and prediction exercises on different kind of transients, including the cooldown, the AC losses assessment and the quench propagation.

Following the model qualification and lessons learnt from the Inserts experience, predictive simulations of the ITER Central Solenoid and Toroidal Field coils operation are performed in normal and off-normal conditions, including e.g. mass flow rate reduction in critical conductors, quench propagation and fast discharge.

The outcomes of the analyses show that the ITER magnets satisfy the design requirements during the normal and off-normal operation, without presenting any critical issues in terms of temperature margin or hot-spot temperature. As a final remark, it is stressed the importance of suitable quench lines for the Toroidal Field magnets to avoid an excessive pressurization of the circuit.

The outcome of the predictive simulations is also useful to the definition of the test plan of ITER Central Solenoid modules in the final qualification tests, foreseen before their installation in the ITER bore. In perspective, the whole chain code development – test of sub-size magnets – interpretation of the results to deduce or validate constitutive relations – application to full-size magnets can be applied to the design of magnets for future tokamaks like the Italian Divertor Tokamak Test (DTT) facility and the EU DEMO.

Contents

List of Figures

List of Tables

Nomenclature

Abbreviations

4C	Cryogenic Circuit Conductor and Coil
AC	Alternate Current
BBs	Bus Bars
BCs	Boundary Conditions
BD	Breakdown
BV	Bypass Valve
BW	Back-Wall (of casing)
CB	Cold Box
CC	Correction Coil
CCC(s)	Casing Cooling Channel(s)
CD	Cooldown
CFETR	China Fusion Engineering Test Reactor
CICC	Cable-In-Conduit Conductor
CS	Central Solenoid
CSI	Central Solenoid Insert
CSIM	Central Solenoid Inner Module
CSOM	Central Solenoid Outer Module
CSMC	Central Solenoid Model Coil
Cu	Copper
CV	Control Valve
DC	Direct Current
DEMO	DEMOnstrating fusion power reactor
DP	Double-Pancake
DTT	Divertor Tokamak Test
EAST	Experimental Advanced Superconducting Tokamak
EM	Electro−Magnetic
EOB	End Of Burn
EU	European Union
FE	Finite Elements
He	Helium
HP	Hexa-Pancake
HTC	Heat Transfer Coefficient
HTS	High Temperature Superconductor
ID	Internal Diameter
IH	Inductive Heater
IM	Initial Magnetization

JAEA	Japan Atomic Energy Agency
JET	Joint European Torus
JT-60	Japan Torus-60
JT-60SA	Japan Torus-60 Super Advanced
KSTAR	Korea Superconducting Tokamak Advanced Research
LHe	Liquid Helium
LN2	Liquid Nitrogen
LTS	Low Temperature Superconductor
MQE	Minimum Quench Energy
NZ	Normal Zone
OD	Outer Diameter
PI	Proportional-Integral
PID	Proportional-Integral-Derivative
PF	Poloidal Field
PW	Plasma-Wall (side of casing)
QD	Quench Detection
QL(s)	Quench Lines(s)
QP	Quad-Pancake
QST	National Institutes for Quantum and Radiological Science and Technology
RH	Resistive Heater
RP	Radial Plate
SC	Superconductor/Superconducting
SHe	Supercritical Helium
SOB	Start Of Burn
SOD	Start Of Discharge
SS	Stainless Steel
SV	Safety Valve
SW(s)	Side-Wall(s) (of casing)
TH	Thermal-Hydraulic
TF	Toroidal Field
TFI	Toroidal Field Insert
TFTR	Tokamak Fusion Test Reactor
V&V	Verification and Validation
WP	Winding Pack
WUCD	Warm-Up Cooldown

Symbols

$\int I^2 dt$	Energy deposited by IH
A	Area
B	Magnetic field
$\overline{B^2}$	Integral average of squared magnetic field

$\dot{B}(t)$	Magnetic field time derivative
dB/dx	Magnetic field spatial derivative
dT/dt	Temperature time derivative
$\cos\theta$	Cosine of the strands average inclination angle due to petal twist
dm/dt	Mass Flow Rate
d_{eff}	Effective diameter of superconducting strands
D	Hydraulic diameter
ΔT^{max}	Maximum temperature difference
ΔT_{marg}^{min}	Minimum Temperature Margin
E	Energy (deposited)
f	Friction factor
FF	Friction Factor multiplier
g	Spiral gap
H_{HB}	Hole-bundle heat transfer coefficient multiplier
h	Enthalpy
I	Transport current
I_C	Critical current
J_C	Critical current density
L	Length
M_λ	Multiplier for HTC
$n\tau$	Coupling loss time constant
P	Linear power density
p	Pressure
$Q-factor$	Gain factor of fusion reaction
q	Energy density
q''	Heat flux
q'''	Volumetric heat generation
Re	Reynolds number
T	Temperature
T_C	Critical temperature
T_{CS}	Current sharing temperature
t	Time
VD	Voltage difference
V_q	Quench propagation speed
x	Spatial coordinate

Greek

α	Magnetic field gradient on cable cross section
γ	Ratio of specific heats
Δ	Difference
δ	Thickness of material

ε	Strain
λ	Thermal conductivity
μ	Dynamic viscosity
μ_0	Vacuum magnetic permeability
φ	Bundle void fraction
ρ	Density
$\rho_{el,xx}$	Electrical resistivity (of material *xx*)
σ	Stefan-Boltzmann constant (5.67 × 10^{-8} $Wm^{-2}K^{-4}$)
τ	Decay time constant

Subscripts

0	Initial value (at $t = 0$ s)
ave	Average
b	Bundle
$coup$	Coupling losses
$dump$	Current dump
ext	External
h	Hole
$hyst$	Hysteresis losses
int	Internal
in	Inlet
jkt	Jacket
out	Outlet
rad	radiative
st	Strands
STR	Structure
$nonCu$	non-copper material
$TSxx$	Temperature sensor at location *xx* (e.g. TS02)

Chapter 1

Introduction

1.1. Nuclear fusion and magnetic confinement

1.1.1. Energy and the role of fusion power

It is well known that the living standards and the quality of life are strictly related to the energy consumption [1]. With upcoming challenges related to energy supply and consumption, nuclear energy is the best candidate to provide a clean and large amount of energy in substitution of the traditional fossil (chemical) energy sources [2]. Nuclear reactions differ from traditional combustion for the mechanism involved in the energy release process [3].

Simplifying, chemical reactions involve reactants and products, which both can be molecules or elements. When a reaction occurs, the products are other molecules, different from the reactants themselves. However, the inventory of primary elements (e.g. carbon, oxygen, hydrogen) remains unchanged, see for instance:

$$2C_8H_{18} + 25O_2 \rightarrow 16CO_2 + 18H_2O + 94eV \qquad (1)$$

where 1 eV = 1.602×10^{-19} J.

On the other side, nuclear reactions, both fission and fusion, change the reactant atoms into different product atoms: in nuclear reactions, passing from reactants to products, only the total number of nucleons (sum of protons and neutrons), is conserved, not the reactant elements type, see for instance:

$$n +_{92}U^{235} \rightarrow_{54} Xe^{140} +_{38}Sr^{94} + 2(n^1) + 200MeV \qquad (2)$$

In the process, the mass is not conserved and the difference (Δm) is transformed into energy according to Einstein's formula $\Delta E = \Delta m \times c^2$. During nuclear reactions, a change in the potential nuclear energy occurs; in other words there is a change in the binding energy between nuclei: the final state is more stable as the binding energy has increased during the reaction, see Figure 1.1, and the energy change corresponds to the right hand side of Einstein's formula.

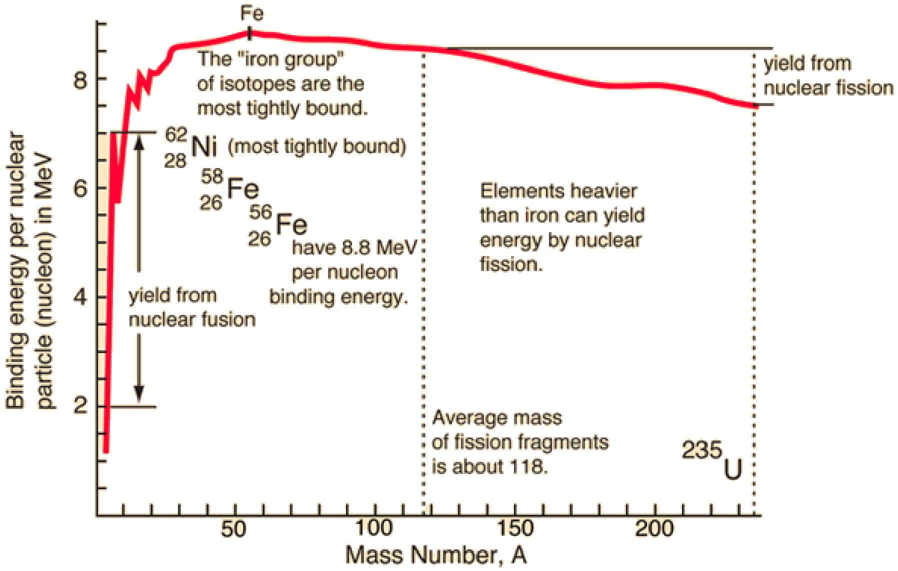

Figure 1.1. Binding energy curve as function of atom mass number [4].

Nuclear energy can be obtained through two different kind of reactions: fission and fusion. The most exploited fission reaction consists in the split of Uranium $_{92}U^{235}$ atoms using "slow" (thermal) neutrons, with the production of energy and lighter (the so-called "daughter") elements, often radioactive. The energy released can be determined using the standard nuclear data, and it turns out that the energy released by 1 kg of nuclear fuel is about 10^6 times larger than the energy produced with the same amount of fossil fuel. Other heavy atoms (and some isotopes) can be used to produce fission reactions, e.g. $_{92}U^{233}$, Plutonium ($_{94}Pu^{239}$, $_{94}Pu^{241}$). Despite the promising performances, fission technology encounters some problems related to the safe operation of the power plants and the management of the radioactive products. This makes the public opinion sceptical about the large deployment of nuclear power plants to cope with the increasing energy demand.

Fusion is another nuclear reaction that specifically involves the merging of light nuclei (e.g. Hydrogen−H, Deuterium−D, Tritium−T and Helium−He) into heavier elements. This is the first and main difference with respect to the fission reaction, as shown in Figure 1.1.

From the engineering point of view, the most interesting fusion reactions are the D−D and D−T reactions:

$$D + D \rightarrow He^3 + n + 3.27MeV \tag{3}$$

$$D + D \rightarrow T + p + 4.03MeV \tag{4}$$

$$D + T \rightarrow \alpha + n + 17.6MeV \tag{5}$$

Nuclear fusion has three main advantages with respect to nuclear fission:

- Fuel reserves: D is naturally present in ocean water: 1 atom of D every 6700 atoms of H, indeed very abundant. The extraction of the whole D inventory present in the ocean would allow to supply the Earth present total energy consumption rate with fusion energy for 2×10^9 years. On the other side, Tritium is radioactive (half-life of 12.6 years) and must be produced on the reactor site by breeding Lithium with the support of neutron multipliers (e.g. Pb). The self-sustained Tritium production for the reactor operation is one of the critical issues for the achievement of fusion energy;
- Environmental impact: fusion reactions do not produce CO_2 or other greenhouse emissions, nor harmful chemicals. The major environmental concerns on nuclear fusion are the onsite presence of T and the activation of structure materials following neutron irradiation, which however have a shorter "safe storage" time (~100 years) with respect to fission products (~1000 years);
- Safety: the basic physics governing nuclear fusion makes impossible to have chain reactions, which instead normally occur in fission reactions (and can lead to uncontrolled, diverging reactions).

Beside the advantages, however, nuclear fusion also has several issues, which involve various aspects:

- Scientific challenges: to obtain the D−T reaction, it is necessary to heat the fuel at a temperature of the order of 10^8 K, which is literally "Hotter than the Sun" [5]. At this temperature, the fuel mixture is fully ionized becoming a plasma that once heated, must be kept in position using an inertial or magnetic confinement;

- Technological challenges include new materials, the design and operation of superconducting (SC) magnets, Tritium production, radiation protection, remote handling and others;
- Economics: fusion reactors are complex machines, still at an experimental stage. The balance between costs and energy price to the final customer is a key issue to make the technology competitive on the market.

1.1.2. Magnetic confinement

The achievement of the environmental conditions allowing fusion reactions is an extremely challenging task. The Lawson Criterion defines a sort of minimum condition in order to reach self-sustained fusion reaction: the machine must be able to exceed the value of 3×10^{21} m^{-3} keV/s for the, so called, triple product [6] of plasma electron density, plasma temperature and confinement time (or rate of energy loss). In addition, the Q-factor, also called gain factor, identifies the ratio between the output and input energy, see (6): if a machine is not able to provide $Q > 1$, it has no practical use in terms of energy production.

$$Q - factor = \frac{E_{output}}{E_{input}} = \frac{Energy\ released\ by\ fusion}{Energy\ injected} \qquad (6)$$

In order to achieve controlled fusion, since no material can get in contact with the hot plasma without being destroyed, the modern and most promising technology focuses on the magnetic confinement of the plasma. Depending on the magnetic system layout, the machine can be called tokamak, stellarator or spheromak.

If the plasma is confined in a toroidal shaped chamber, the machine is called tokamak [7], see Figure 1.2, from Russian тороидальная камера с магнитными катушками (toroidal'naya kamera s magnitnymi katushkami) which means: toroidal chamber with magnetic coils.

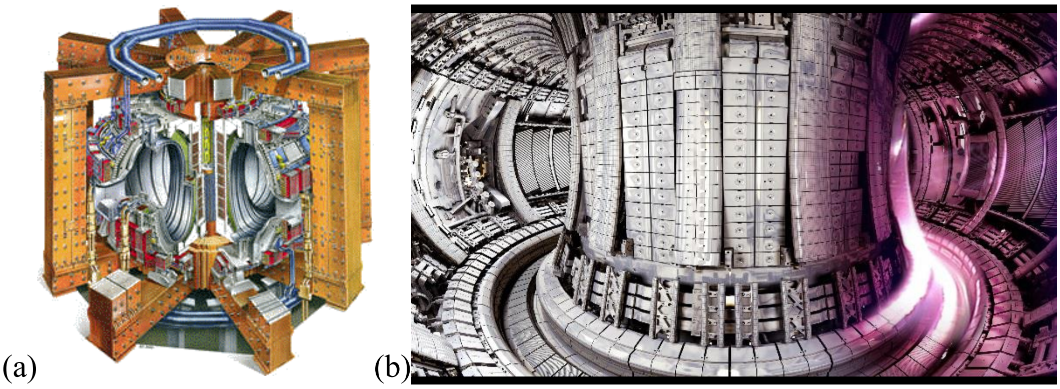

Figure 1.2. (a) Cutaway of the JET torus [8]. (b) Internal view of the JET fusion chamber with a superimposed camera picture of the plasma visible spectrum [9].

Up to now, over 198 tokamaks have been built with different dimensions and magnetic configurations. The first large tokamaks, the American TFTR and the European JET, were built in the 1980’ aiming at the ignition of fusion energy, i.e. Q-factor = 1. However they both failed short from the goal. Then, the JT-60 (Japan) tokamak previously limited to Deuterium-plasmas only for lack of Tritium-handling facility is now being upgraded to the JT-60SA (superconducting) version. The Russian T-15 tokamak was the pioneer for the use of superconducting magnets for the magnetic confinement. The use of superconducting magnets represented a milestone in the fusion research and the tokamak construction, because in order to confine the plasma and aim at the achievement of Q-factor > 1 the high magnetic field needed (~15 T) can be produced only with superconducting magnets. Today several superconducting tokamaks exist all over the world, for instance the EAST tokamak in China, the KSTAR tokamak in Korea and the W7-X stellarator in Germany, and other are being designed (EU DEMO, K-DEMO, Italian DTT, Chinese CFETR) or built (Japanese JT-60SA).

The magnetic configuration of a tokamak must keep the plasma confined and this is done using the superposition of magnetic field lines produced by a set of coils, with different shapes according to their function, see Figure 1.3:

- The Central Solenoid (CS) acts as the primary circuit of a transformer, which works in pulsed mode, so a DC current is induced in the plasma, which acts as the secondary circuit of the transformer;
- The Toroidal Field (TF) coils generate the toroidal magnetic field lines followed by the plasma particles;
- The Poloidal Field (PF) coils are used for plasma (mainly vertical) positioning and shaping inside the chamber of the tokamak.

The size and number of each coil depends on the machine design and required performances: basically, large and efficient machines require large and efficient magnets.

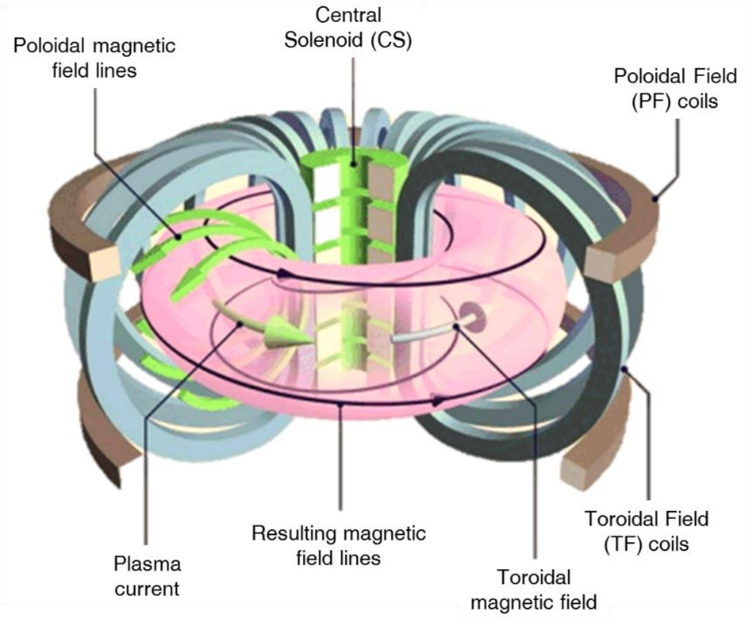

Figure 1.3. Representation of the magnetic system and its field lines in a tokamak (adapted from [10]).

1.2. The ITER project

ITER ("*the way*" in latin) is the world largest superconducting tokamak, see Figure 1.4, currently under construction in Cadarache (France). ITER is an international project, initially participated by the European Union (EU), Japan, Russia, China, India, Korea and the United States, counting more than thirty-five nations.

The ITER project has an ambitious plan [11] to beat the challenges for the realization of fusion energy. First, it aims at producing a stable and well-confined plasma with $Q = 10$ lasting for sufficiently long time to reach quasi-steady-state operation and then, in a second part of the experimental plan, to achieve steady-state operation with $Q = 5$. In addition, the construction of ITER should demonstrate the capability to develop different plasma facing materials, to operate remote handling on large scale, to manufacture large superconducting magnet and to produce Tritium inside the machine, to finally make all the systems working together for a fusion power plant. Finally, since ITER will be operated under nuclear regulations the machine must also demonstrate all safety features of fusion reactors, in terms of D−T reactions and plasma control, with negligible consequences to the environment. Latest news say that first plasma is expected for 2025 [12].

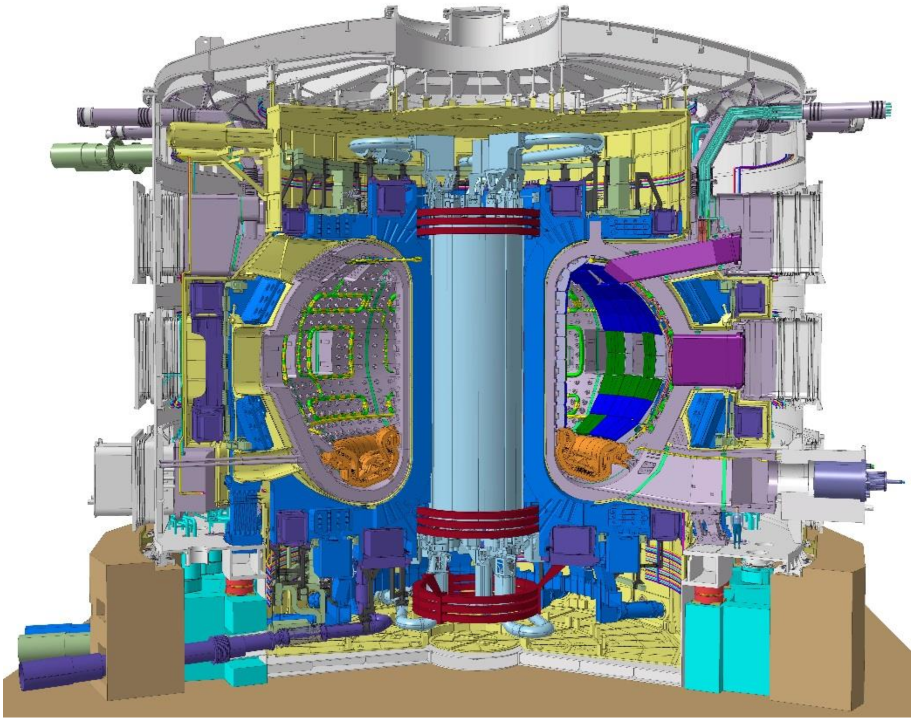

Figure 1.4. A cutaway of the ITER tokamak, produced by the ITER Design Office in January 2013 [13].

1.2.1. Magnet system

The ITER superconducting magnet system is constituted by four separate sub-systems, specifically: the Central Solenoid, eighteen Toroidal Field coils, six Poloidal Field coils and other eighteen Correction Coils (CCs) [14], see Figure 1.5. All the magnets are cooled using supercritical He (SHe) in forced flow with a nominal inlet pressure between 0.5 and 0.6 MPa and a temperature of 4.5 K, to guarantee a sufficiently high temperature margin, i.e. the “distance” from the current sharing temperature (T_{CS}) of the conductors, and avoid the loss of the superconducting properties (also called quench). The heat removed from the coils is transported through dedicated cooling loops towards a liquid helium (LHe) bath, acting like a thermal buffer for the heat load coming from the coil and cools He before it is sent back in the cryogenic refrigerator, see Figure 1.6.

During the machine operation, the CS induces the plasma current by changing its current (and thus its magnetic field). However, these variations generate AC losses in all magnets, heating them up and reducing the temperature margin. The time variations of the magnetic field induce eddy currents also in all the bulky stainless steel (SS) structures of the tokamak. Finally, the TF coils (the closest to the plasma chamber) are also partly subject to the nuclear heat load coming from fusion reactions, since this is not fully shielded by the other components closer to the plasma (first wall, vacuum vessel, neutron and thermal shields).

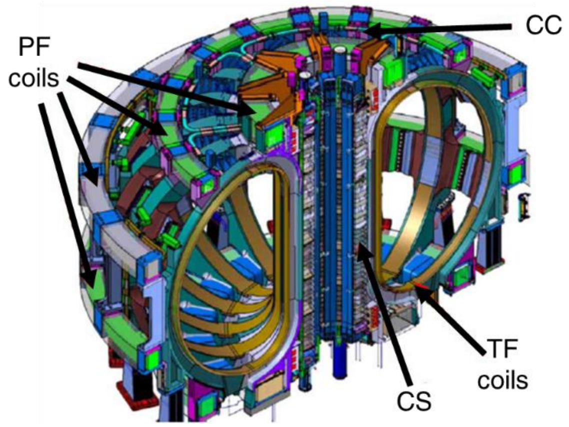

Figure 1.5. ITER magnet system (reproduced from [14]).

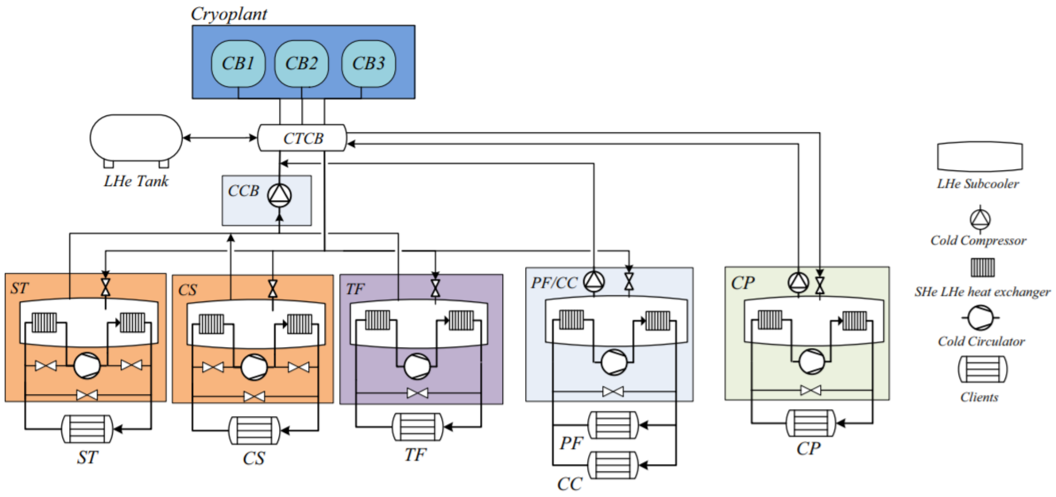

Figure 1.6. Scheme of ITER cryogenic system (reproduced from [15]).

The ITER magnet system is being manufactured separately in different countries participating to the project, see Figure 1.7: the CS will be entirely manufactured by the US; of the total 19 TF coils (18, plus 1 spare), ten winding packs (WPs) were commissioned to the EU and the remaining nine to Japan, which is in charge also of the casing sub-assemblies manufacturing; the PF coils will be mostly produced in the EU (PF2-6) with the single PF1 manufactured in Russia; finally all the CCs will be produced in China.

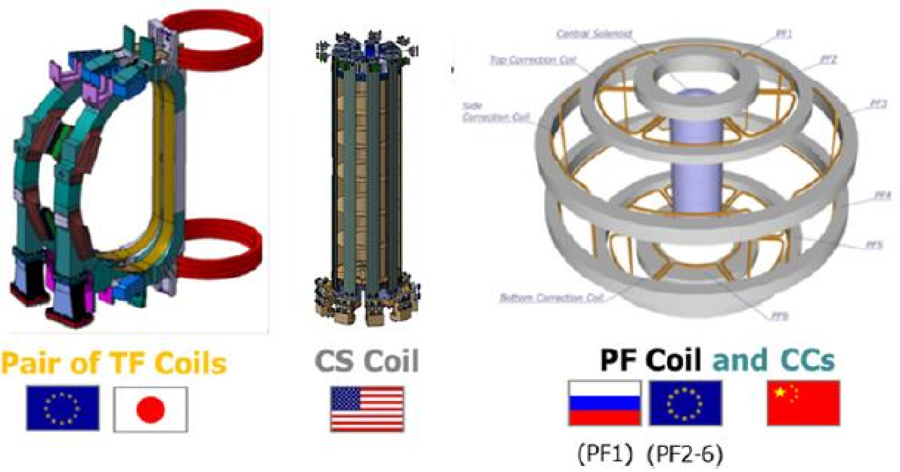

Figure 1.7. Illustration of the ITER magnets and countries in charge for the manufacturing (reproduced from [16]).

1.2.2. Cable in conduit conductors

To produce the large superconducting magnets of fusion machines, the cable-in-conduit conductors (CICCs) concept has been adopted [17]. Different design of CICCs, see Figure 1.8, have been produced [18] depending on the application and the performances required. However, all the CICCs consist of many small wires, called strands, twisted together and inserted within a conduit, called jacket. In the conduit, a coolant, usually supercritical He, flows through one or more paths, see Figure 1.9: one cooling path, namely the bundle, which shares the same cable region of the strands, and variable number of empty channels, usually called holes, acting as pressure relief channels.

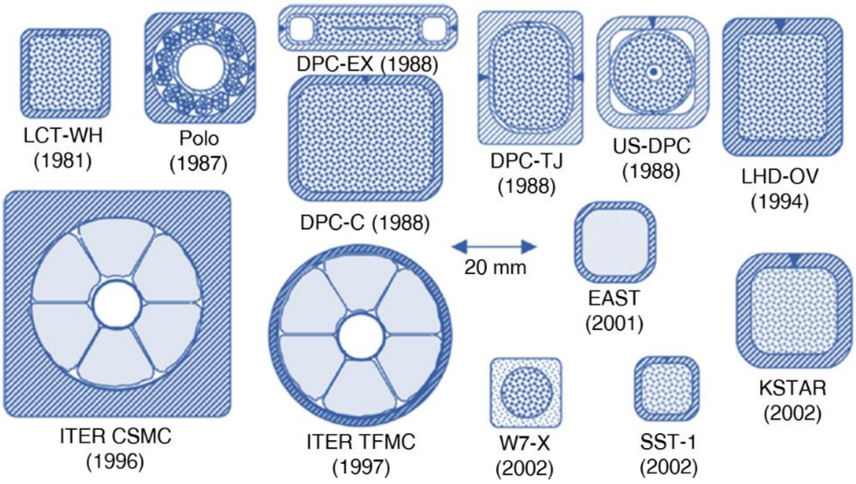

Figure 1.8. Different CICCs layouts developed in the last four decades [18].

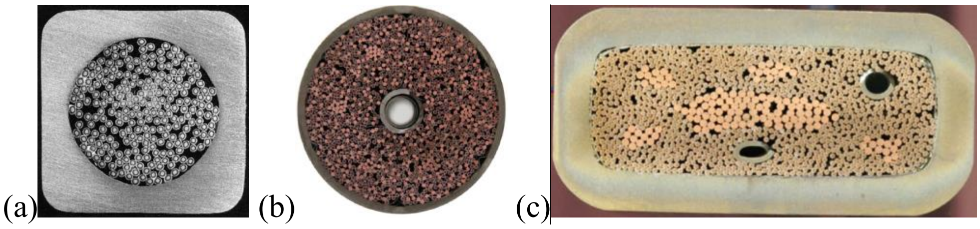

Figure 1.9. Cross section of CICCs for the (a) Wendelstein-7X stellarator (no holes, reproduced from [19]), (b) ITER TF (one hole, reproduced from [20]), (c) EU DEMO TF (two holes, reproduced from [21]) coils.

Each strand inside the cable is basically a copper (Cu) matrix containing thin filaments, see Figure 1.10, of a low-temperature superconducting (LTS) material, usually Nb_3Sn (T_C = 18.3 K) or NbTi (T_C = 10 K). Today researchers are also developing CICCs based on high-temperature superconductors (HTS). For additional details about superconductivity and superconducting magnets please refer to [22] [23] [24].

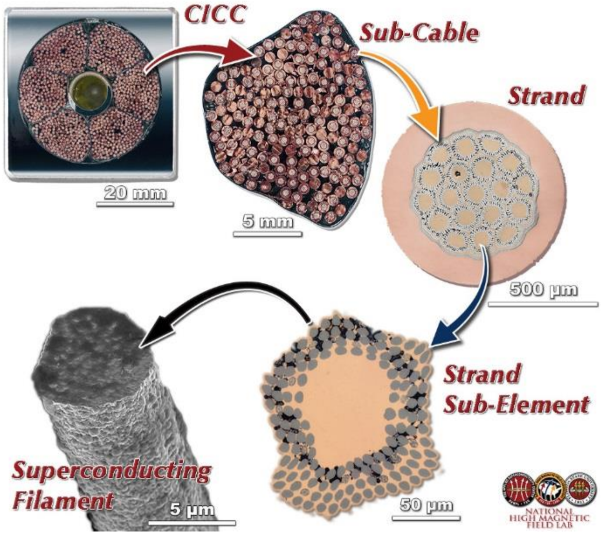

Figure 1.10. Detailed view from the CICC to the SC filament of a typical ITER conductor [25].

CICCs gained great success in large application in view of their numerous advantages, because the adoption of thin wires, instead of a large bulk conductor, allows an easier manufacturing, handling and bending. Moreover, the large surface area around the wires guarantees a good heat transfer with the coolant and an efficient heat removal during the operation of the machine. Finally, the stainless steel conduit protects the wires and, thanks to the large mechanical resistance, allow to tolerate large electro-magnetic forces.

However, there are also disadvantages: since the coolant and conduit walls occupy part of the cross section of the cable, the amount of superconducting wires that can be put in the cable is limited, reducing the maximum transport current and therefore the magnetic field that can be generated. For this reason, CICCs are unsuitable for application needing very large magnetic fields, like accelerators, which instead use Rutherford cables, see Figure 1.11.


(a) (b) (c)

Figure 1.11. Picture of ITER (a) CS, (b) TF CICC [25] and (c) wires for a prototype Rutherford cable [26].

1.3. European roadmap and the EU DEMO

ITER present and future experience should lead to a complete and comprehensive understanding of plasma physics and fusion technology, so that the development of a commercial reactor will be justified. The first European commercial reactor is usually referred to as EU DEMO (DEMOnstrating fusion power reactor) developed by the EUROfusion consortium. However, the road to fusion energy is not a straight line; in fact, in 2012, "A Roadmap to the Realisation of Fusion Energy" was edited [27], listing the main challenges for the achievement of electricity from fusion by 2050. The roadmap has been updated in 2018 [28], but the challenges are unchanged:

- *Plasma regimes of operation*: hot plasma must be confined and kept in safe and stable condition. The magnetic confinement configurations developed for ITER operation are not suitable for DEMO plasma regimes, so new solution must be developed.
- *Heat exhaust systems*: the plasma heat exhaust is deposited in a small region inside the reaction chamber. This region is part of a component called divertor, which must withstand the large thermal loads coming from the plasma. To support the divertor research activities, the DTT (Divertor Tokamak Test) [29] facility will be built in Frascati (Italy), to test new materials and cooling solutions.
- *Neutron resistant materials*: because of the large neutron flux expected in DEMO, new materials with reduced activation and high resistance to radiation damage need to be developed.
- *Tritium self-sufficiency*: Tritium, which must be produced on site and cannot be store for safety reasons. Anyway, DEMO Tritium self-sufficiency is necessary, so an efficient breeding and extraction systems must be developed, together with the complete Balance of Plant, including the heat exchangers (HXs) and the systems for electricity generation, which are indeed not present in ITER.
- *Safety*: even if fusion has some intrinsic safety features, it must be ensured that DEMO protection will be based on passive systems and that, in case of any kind of accidents, even the most severe, no evacuation will be needed.
- *Integrated design*: large importance of remote maintenance, for which a large experience will be gained during ITER operation. However, DEMO will need more efficient solutions as well as highly reliable

components, in order to guarantee the sufficiently high level of reliability and availability required for a power plant.

- *Competitive cost of electricity*: fusion will have to demonstrate economic competitiveness in order to be considered a feasible alternative for electricity production. In view of a commercial stage of fusion energy, the ITER building experience should also demonstrate the capability of producing specific components with reduced costs and on an industrial scale.
- *Stellarators* have been identified as long-term alternative to tokamaks and therefore their development is expected to continue.

It must be stressed that all missions rely on theory and modelling, fundamental to provide design and extrapolation capabilities. Reliable codes can be obtained only passing through several validation exercises which require detailed experimental data. A EUROfusion financing program supports and promotes activities in basic research, modelling and high-performance computing.

1.4. Motivation and aim of this thesis

The achievement of fusion energy needs computational tools in all the engineering aspects of the research process, especially when dealing with important and expensive components, like in the case of the superconducting magnets and the Cryogenic Circuit Conductor and Coil (4C) code [30].

Additionally, codes validation and verification (V&V), a prerequisite for their reliable application, is fundamental not only in fusion research, but in the entire scientific community [31]. Validation exercises can be done with different timings with respect to the experiments: simulations can be performed after the tests, taking advantage of having seen the measurements, or in advance to preform blind predictions, i.e. without knowing the actual results. Moreover, even if ITER is currently under construction, a detailed performance analysis of the entire ITER CS and TF coils, after the test campaigns carried out on the conductor samples, has never been done.

The purposes of the analyses and simulations carried out and presented in this work are:

- to take further steps in the improvement and validation of the 4C code [30]. This means that the code is used to deduce constitutive relations (“calibration”) for thermal-hydraulic, electro-magnetic and thermo-electrical phenomena and then it is validated against experimental data for several transients (e.g. cooldown, AC losses, stability, quench, etc.), in view of the different time and spatial scales involved;

- to *reliably* predict the actual ITER CS and TF magnet operation, after their design and qualification, starting from the analysis of the data collected during the ITER Insert coils experimental campaigns;
- to apply the validated code to make comprehensive thermal-hydraulic predictions of ITER magnets, for instance by planning the ITER CS modules tests taking place at the new General Atomics facility in the US, but also to help the design of magnets for future tokamaks, like DTT and the EU DEMO.

Chapter 2

Test and modelling for an improved thermal-hydraulic analysis of the ITER coils

2.1. Context

In the framework of the R&D activities for ITER, a series of tests has been planned for the conductors' qualification [16]. These tests include the experimental campaign performed on the Central Solenoid and Toroidal Field Insert Coils carried out in 2015 and 2016-2017 respectively.

2.2. The Central Solenoid Insert coil test

In 2015, the ITER Central Solenoid Insert (CSI) coil [32] has been tested at the National Institutes for Quantum and Radiological Science and Technology (QST, former Japan Atomic Energy Agency - JAEA) in Naka, Japan. The tests aimed at assessing the ITER CS conductor performances in ITER-relevant operating conditions.

During the tests, the coil has been inserted in the borehole of the Central Solenoid Model Coil (CSMC) [33] providing the background magnetic field. The tests, and the related analyses carried out, include:

- Cooldown, which is not a specific test it-self, but the analysis of the data allowed to develop the model of the CSI structure lately used in other analyses [34];
- Hydraulic characterization, to measure the pressure drop across the coil with various inlet mass flow rates and therefore to assess the hydraulic impedance of the conductor and the validity of friction factor correlations;
- AC losses assessment, to assess the value and the impact of electromagnetic (EM) cycles on the coupling and hysteresis losses [35] [36];
- Quench propagation, to assess the thermo-electrical performances of the cable and its hot-spot temperature during a quench [37];
- DC conductor performance, to measure the T_{CS} before and after EM cycles and quench tests [38] and to validate the $J_C(\varepsilon,B,T)$ characteristic of the conductor [39];

The outcomes of these analyses are the constitutive relations used to perform predictive simulations of the actual ITER CS coil.

In detail, the CSI is a 43 m long conductor wound in nine turns, separated by means of epoxy resin spacers, on a stainless steel support structure, see Figure 2.1. The cable layout is the exactly the same of the conductor used to wind all the modules of the ITER CS coil: it has a circle-in-square shape, see Figure 2.1c, where a steel jacket surrounds the two parallel helium paths (bundle and hole). The main geometrical parameters of the CSI conductor are reported in Table 2.1.

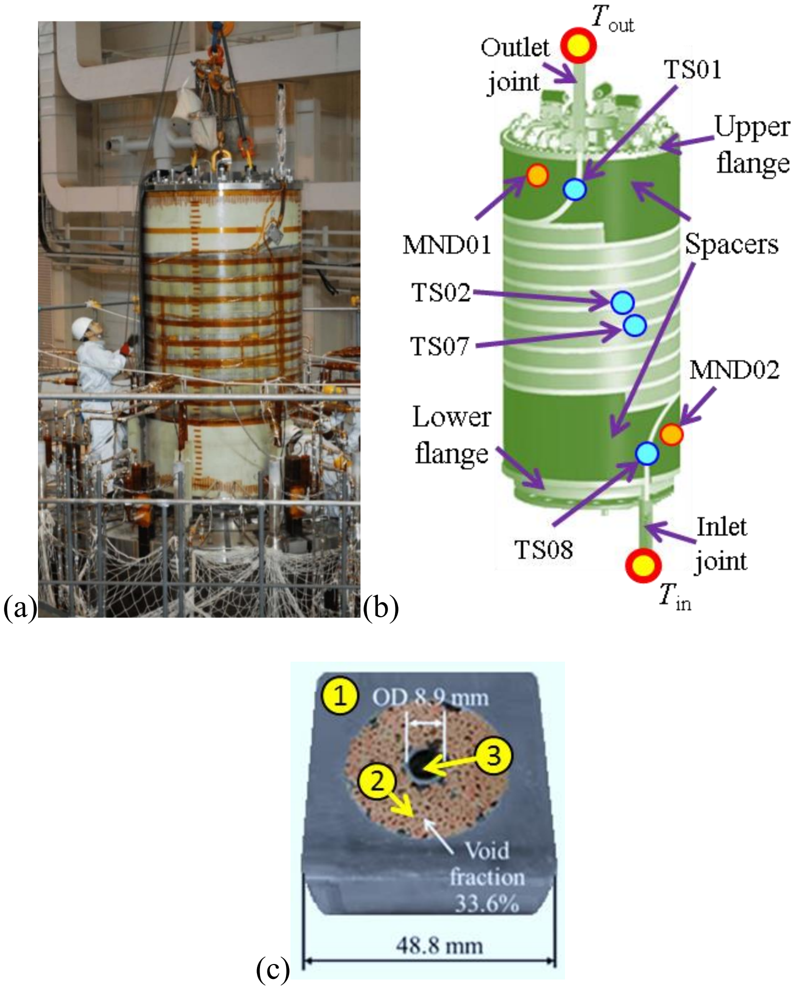

Figure 2.1. (a) Picture of the real CSI coil tested in 2015 (reproduced from [34]). (b) Sketch of the CSI wound on its support structure; some of the available diagnostics is also indicated (TS = jacket temperature sensors, MND = SS spacer temperature sensors, T_{in} and T_{out} are the inlet and outlet He pipes temperature sensors, respectively). (c) Cross section of the CSI conductor showing the (1) jacket, (2) the bundle and (3) the hole.

Table 2.1. Main geometrical parameters of the CSI (and CS) conductor.

Parameter	**Unit**	**Value**
Number of strands (SC+Cu)	-	576+288
Strand diameter (SC/Cu)	mm	0.83/0.83
Cu:nonCu ratio	-	0.97
Central channel ID/OD	mm	7/9
Total He cross section	mm^2	285.35
Jacket external side	mm	48.8
Jacket internal diameter	mm	33.0
Void fraction in bundle region	%	33.6
cosθ	-	0.954
Wrapping area	mm^2	30

2.3. The Toroidal Field Insert coil test

The ITER Toroidal Field Insert (TFI) coil, see Figure 2.2, the last in a series of ITER insert coils, has been tested at QST in 2016-2017.

The TFI is a ~43 m single-layer Nb_3Sn coil, see Table 2.2 for geometrical parameters, manufactured using the same conductor adopted for the ITER TF winding pack [40]. The coil is wound on and kept in position by a SS supporting structure, called mandrel. The TFI assembly has been then inserted in the borehole of the CSMC, providing the background magnetic field, to perform tests in ITER-relevant operating conditions.

As happened for the CSI, several tests have been performed during and the TFI experimental campaign, followed by various analyses, including:

- Thermal-hydraulic (TH) characterization, to validate the existing friction factor correlations and to determine TH constitutive relations of the conductor;

- The assessment of T_{CS} evolution under thermal and electro-magnetic cycling [41];
- Quench propagation, to assess the thermo-electrical performances of the cable and its hot-spot temperature during a quench [42].

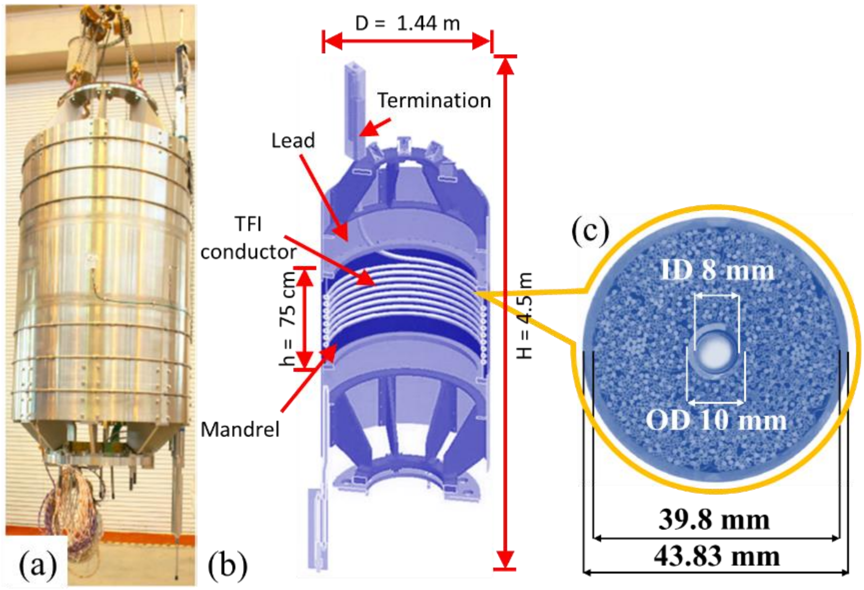

Figure 2.2. (a) Picture of the TFI assembly (courtesy of QST) and (b) drawing of its cross (reproduced from [42]) with (c) zoom on the conductor cross section.

Table 2.2. Main geometrical parameters of the TFI (and TF) conductor [42].

Parameter	Unit	Value
Number of strands (SC+Cu)	-	900+522
Strand diameter (SC/Cu)	mm	0.822/0.821
Cu:nonCu ratio	-	0.954
Central channel ID/OD	mm	8/10
Total He cross section	mm^2	420
Jacket internal / external diameter	mm	39.8 / 43.89
Void fraction in bundle region	%	31.3
$\cos\theta$	-	0.9699
Wrapping area	mm^2	34

2.4. The 4C code

The 4C code [30] [43] is the state-of-the-art tool for the thermal-hydraulic analysis of transient in superconducting magnets for fusion application; it is very flexible and easy-to-use in terms of geometry definition. The code has a modular structure, see Figure 2.3, with each module properly coupled to the others, describing a specific sub-component of the magnet system.

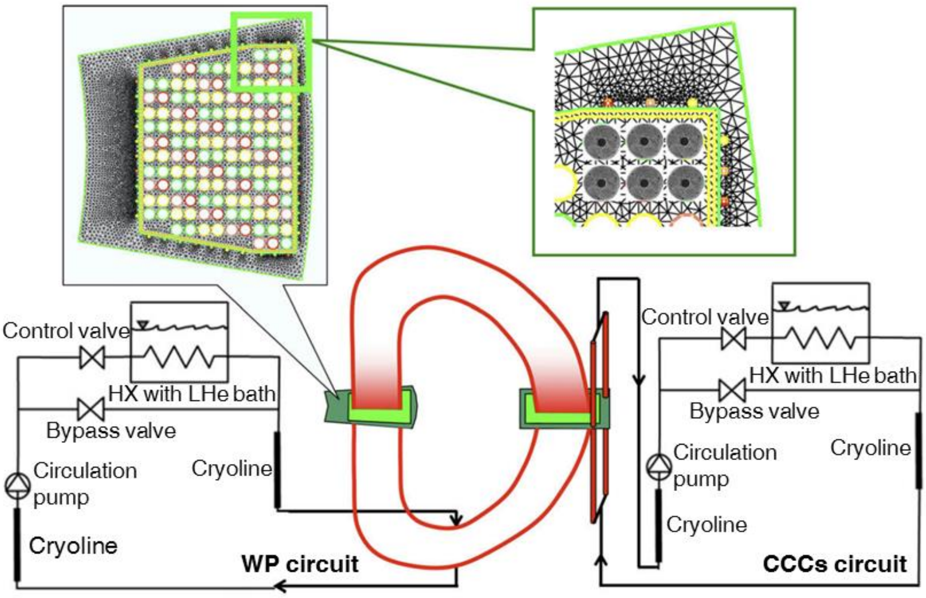

Figure 2.3. Schematic representation of 4C code modules (reproduced from [30]): coil WP, CCCs, structures and cooling circuits. Top left: inboard leg cross section of ITER TF coil; top right: zoom showing some CICCs of the coil winding, CCCs and 2D mesh of the structures; bottom left and right: winding and case cooling circuits, respectively.

The main module simulates the coil winding: the transient in each hydraulic channel is solved using a 1D FE model for the CICC in the axial direction. The mass, momentum and energy equations are solved for each He flowing path, while for the conductor and the jacket, two separate conductive equations are used, thermally coupled with the fluids by means of constitutive relations defining the heat transfer coefficients with a Mithrandir-like model [44] [45]. The hole and bundle region are thermally coupled through the perforated and not-perforated regions of the central spiral, therefore the heat transfer is modelled with a parallel of thermal resistances, see Figure 2.4. The heat transfer coefficient (HTC) between He and solids (jacket-bundle, strands-bundle) is computed using the Dittus−Boelter correlation, as previously described in [44] and supporting literature. The bundle−hole mass transfer, discussed in detail in [44], is driven by the Δp between the two regions and through the perforated fraction of the spiral.

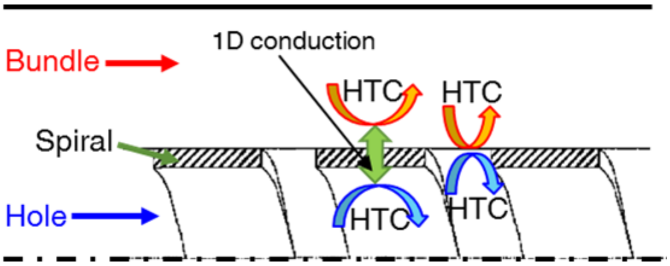

Figure 2.4. Sketch of the heat transfer model between the hole and bundle across the spiral.

The WP is inserted in bulky SS structures, cooled by dedicated casing cooling channels (CCCs), so a separate module is used for the solution of the transient in each of these channels where the mass, momentum and energy equations are discretized using a 1D FE scheme, in the same way as in each of the CICC He regions described above. The pipe wall can also be included in the model with a separate conductive 1D FE equation.

The casing structure thermal analysis is performed solving the 2D heat conduction problem on selected poloidal cross sections. This model is based on the FE solver FreeFem++ [46].

The last module is dedicated to the model of the external cryogenic circuit(s) for the SHe. The module is built using the equation based, object-oriented modeling language Modelica®[1] [47] [48] in the Dymola® [49] environment. The new Cryogenics library, developed as extension of the ThermoPower open-source library [50] [51], contains the model of all the main components of the cryogenic circuit (e.g. pipes, valves, volumes, circulators, LHe bath, controllers and HXs).

2.5. Analysis of the CSI tests

In this section, the 4C model of the CSI is used for the analysis of the hydraulic characteristic of the conductor and for the validation against the data from the CD and the AC loss measurements.

2.5.1. Hydraulic characteristic

The hydraulic tests have been performed measuring the pressure drop on the coil with increasing values of mass flow rate: the facility sets a specific value of the

---

[1] Modelica® is a trademark of the Modelica Association.

mass flow rate at the inlet of the coil, when the steady-state is reached, the corresponding pressure drop is recorded. In addition to the purely hydraulic tests, the mass flow rate-pressure drop dependency can be deduced also during the steady-state cold operation of the coil, for instance for the data recorded at night when no experiments are performed.

From the available data it has been possible to identify several time intervals in which relevant quantities, namely temperatures (*T*), pressures (*p*), mass flow rates (*dm/dt*) and pressure drop (Δp), can be assumed to be reasonably constant for a sufficient long time, of the order of the mean residence time in the conductor (~200 s). On such time intervals, the averages of relevant quantities have been evaluated.

Being the hole and bundle flow in parallel, the pressure drop is the same for both channels and determined as:

$$\Delta p = \Delta p_{hole} = \Delta p_{bundle} = 4f\frac{(dm/dt)^2}{2\rho A}\frac{L}{D} \tag{7}$$

where Δp [Pa] is the pressure drop, *f* [-] the friction factor in the channel, ρ [kg/m^3] the density, *dm/dt* [kg/s] the mass flow rate in the channel, *A* [m^2] the flow area, *L* [m] the hydraulic length and *D* [m] the hydraulic diameter of the considered path. The friction factor correlations, available in literature for this specific conductor layout, for hole [52] and bundle [53] (with a correction coefficient of 1.35 [37]), are defined as:

Hole [52]

$$h^+ = \left(\frac{\delta}{D_h}\right) Re_h \sqrt{\frac{f_h}{2}} \tag{8}$$

$$R(h^+) = 6.4 \cdot (h^+)^{0.1717} \cdot \left(\frac{g}{\delta}\right)^{-0.3428} \tag{9}$$

$$R(h^+) = \sqrt{\frac{2}{f_h}} + 2.5 \ln\left(\frac{2\delta}{D_h}\right) + 3.75 \tag{10}$$

Bundle [53]

$$f_b = FF_b \frac{1}{4}\frac{1}{\varphi^{0.72}}\left(0.051 + 19.5 \times Re_b^{-0.88}\right) \tag{11}$$

In (8) − (10), to be solved iteratively, δ [m] is the spiral thickness, Re_h the hole Reynolds number, f_h the hole friction factor, g [m] the gap in spiral, D_h [m] the hole hydraulic diameter. While in (11), f_b [-] is the bundle friction factor, FF_b is a correction factor (equal to 1.35 [37]), φ [-] the bundle void fraction and Re_b the bundle Reynolds number.

In the present validation exercise, the set of friction factor correlations should be able to reproduce the hydraulic characteristic of the conductor described by the identified experimental points, see Figure 2.5. However, a relative error up to ~31% is observed between the computed and the experimental characteristic that may be due to some *dm*/*dt* measurement issues occurred during the campaign [54].

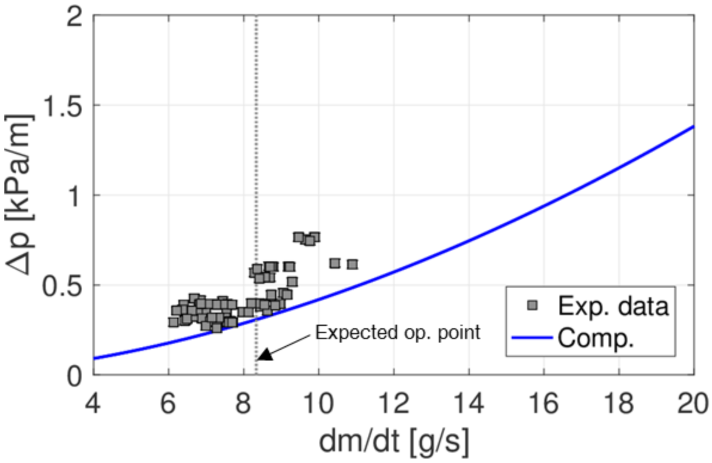

Figure 2.5: CSI test analysis: hydraulic characteristic of the CSI showing experimental data (grey squares) and computed hydraulic impedance (blue line).

In any case, it is not sufficient that the set of correlations captures the hydraulic impedance: for a complete conductor characterization, also the average flow speed, representative of the mass flow rate repartition, must be captured. In fact, similarly to what has been discussed in [21], even if for a given mass flow rate there are infinite combinations of bundle and hole friction factor correlations fitting the pressure drop, only one among these sets is also fitting the average flow rate. This set of correlations already proved this property [37] and the foreseen mass flow rate repartition is ~40% in the bundle and ~60% in the hole, reasonably constant among a wide range of total mass flow rates, see Figure 2.6.

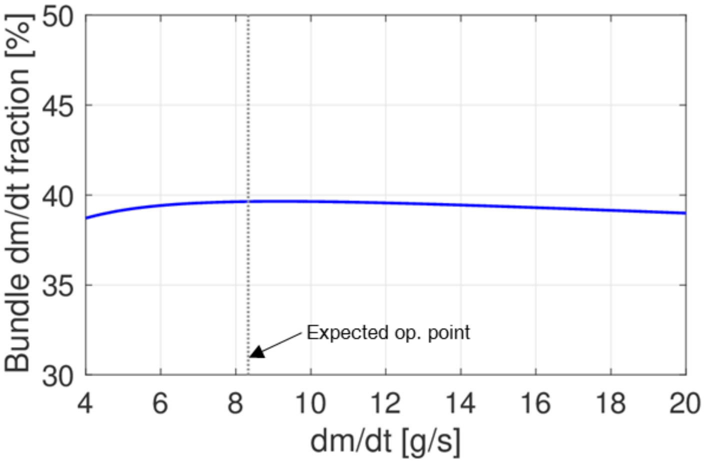

Figure 2.6. CSI test analysis: fraction of bundle mass flow rate in a range of total mass flow rates.

2.5.2. Cooldown[2]

All superconducting magnets must be cooled from ambient to cryogenic temperature before their operation. Here, the 4C code has been validated on a real cooldown (CD) from 300 K to 4.5 K performed during the CSI tests campaign [34].

The CSMC and CSI cooldown

Here, a typical CD is presented, taking as reference that of the CSMC and CSI performed in 2015. The analysis focuses on the temperature evolution in the coils rather than on the operation of the full refrigerator, for which a simplified model has been developed, see Appendix A.

Cold He arriving from the refrigerator is supplied in parallel to the two coils (CSMC and CSI) and the cooling channels of the respective supporting structures. However, despite some small differences, both the CSMC and CSI follows the same CD strategy consisting in two main stages:

- Stage I from ~300 K to 80 K ($t <$ ~250 h in Figure 2.7): the He inlet temperature (T_{in}) decreases with a constant rate of $dT_{\mathrm{in}}/dt =$ ~−1 K/h controlled with the opening of certain valves in the refrigerator. This slow ramp aims at avoiding thermo-mechanical stresses induced by temperature gradients in the coil. Therefore, if the difference between

---

[2] Part of the work described in this section was also published in [34].

T_{in} and outlet temperature (T_{out}) is larger than the prescribed limit of 50 K, the T_{in} is kept constant. However, since this control is performed only between inlet and outlet, it is not guaranteed that the constraint is always satisfied locally, thus a detailed model is needed;

- Stage II below 80 K ($t > \sim 250$ h in Figure 2.7): the T_{in} is decreased expanding the He in a series of turbines inside the refrigerator. The temperature decrease rate depends on the refrigerator operating point and therefore it is influenced by the characteristic of its components; however manual interventions can be carried out, as it happened several times in the considered case study.

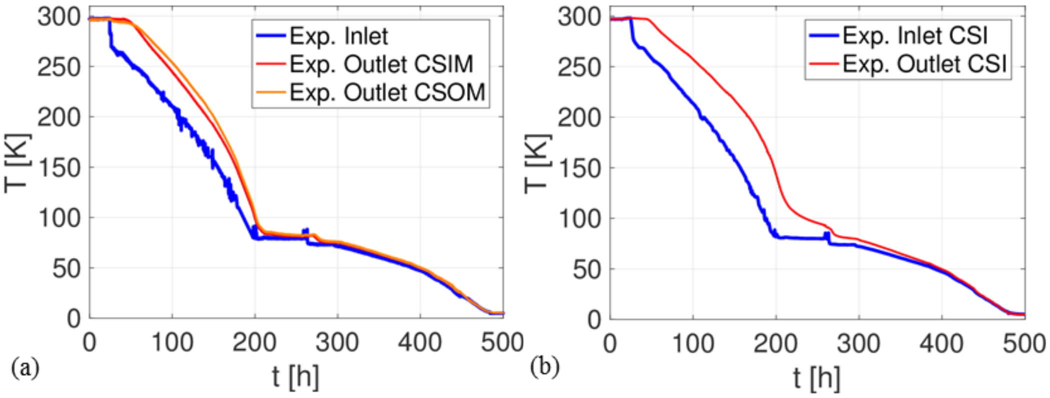

Figure 2.7. CSI test analysis: experimental temperature evolution at: (a) the inlet (thick solid blue) of the CSMC and at the outlet of its inner (CSIM, thin solid red) and outer (CSOM, thin solid orange) modules; (b) inlet (thick solid blue) and outlet (thin solid red) of the CSI.

To simulate the cooldown, a model for the CSI and for the CSMC is needed. The development of such a model is useful when talking about optimization and operational limits of the process. In fact, the CD is a very long and expensive process that can take several weeks and must always satisfy a constraint on the maximum temperature difference (50 K) between any two points inside the coil, conservatively prescribed on the basis of the maximum mechanical stress on the components due to thermal gradients. It is clear that in real situations this value can be roughly estimated only using temperature sensors at the He inlet and outlet of the coil, and in some other limited locations. A detailed model, like the one developed, computes the full temperature map inside the coil, which may help to develop different and optimized CD strategies that still satisfy the constraint.

CSI model

The 4C model of the CSI consists in a 1D flow model for the coil and one separate model for the structure cooling channel, toroidally wound on the bottom and top flanges, see Figure 2.8a. The supporting structure is discretized with a set of eight 2D cross sections along the axial plane, see Figure 2.8b, thermally coupled to each other by means of the advection of the He along the hydraulic channels while, on each section, the heat conduction problem is solved using the finite elements method [30] as described above. The structure model adopts two different cuts meshes, one of which includes the tension rods (diameter suitably rescaled to account for the exact aluminum total volume).

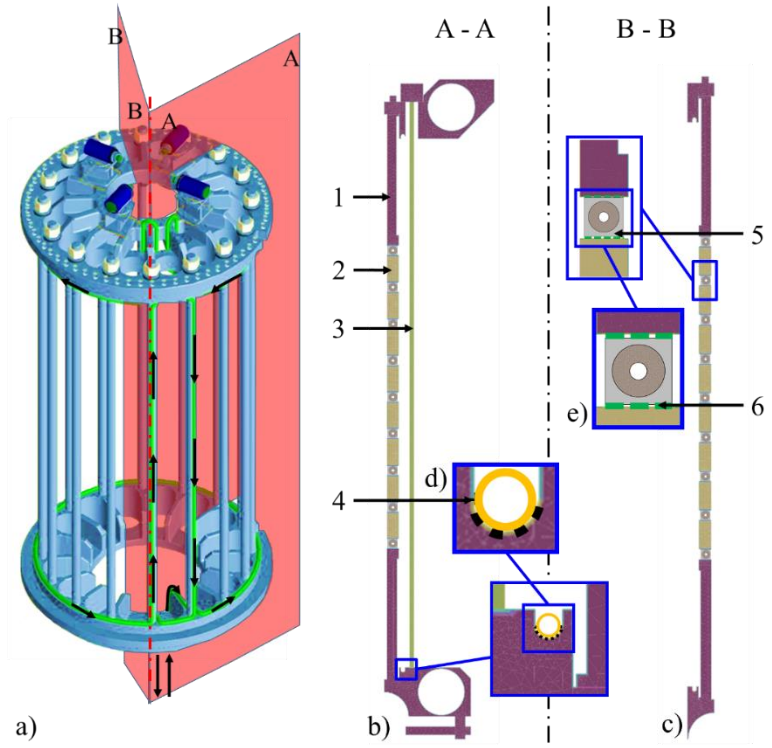

Figure 2.8. CSI test analysis: (a) view of the CSI structures showing only the tension rods and the upper and lower flanges. The black arrows indicate the He path in the cooling channel (in green). (b) and (c) show the 2D cross sections adopted in the 4C structure module, with arrows pointing (1) the SS spacers, (2) the inter-turn epoxy spacers, (3) aluminum tension rods. (d) shows the zoom on the structure cooling channel, with (4) the Cu mesh (dashed black line). Inset (e) shows (5) the CSI CICC and (6) the turn insulation (dashed green line).

The CSI CICC and the structure cuts are thermally coupled through an insulation layer (thickness: 5 mm), modeled as a thermal resistance. The same assumption is used to model the thermal contact between the flange and the cooling channel through the Cu mesh, where the heat flux q'' from the structures is defined as:

$$q'' = M_\lambda \frac{\lambda(T)}{\delta}\left(T_{STR} - T_{pipe}\right) \tag{12}$$

where M_λ is a calibrated multiplier for the thermal resistance, as done in [55], $\lambda(T)$ is the temperature dependent Cu thermal conductivity, δ is the thickness of the Cu mesh, $T_{STR} - T_{pipe}$ is the temperature difference between the structure and the pipe. In addition, the CSI SS spacers outer surface, facing the inner surface of the CSMC layer 1, are subject to the radiative heat transfer q''_{rad}:

$$q''_{rad} = \sigma\left(T^4_{spacers} - T^4_{CSMC,L1}\right) \tag{13}$$

where σ is the Stefan-Boltzmann constant (5.67×10^{-8} $\mathrm{Wm^{-2}K^{-4}}$), T_{spacers} is the SS spacer temperature and $T_{\mathrm{CSMC,L1}}$ is the CSMC layer 1 inlet or outlet temperature to compute the heat flux on the lower or upper spacer respectively.

CSMC model

The model of the CSMC, see Figure 2.9, accounts for all the 36 conductors wound two-in-hands (A and B), resulting in 18 layers organized in the two separate Inner and Outer modules, including layers 1-10 and layers 11-18 respectively. The model diagnostics can accurately describe the thermal-hydraulics of all conductors, even if in the real coil, only some conductors (1A, 5A, 7A, 11A, 15A, 17A) are fully instrumented with pressure drop and inlet and outlet mass flow rate and temperature sensors. The model accounts also for the inter-turn and inter-layer thermal coupling among conductors in contact with each other, extending what was done in [56]. The thermal contact is modeled by mean of series of thermal resistances accounting for the different insulating materials and thicknesses. The He flow, in hole and bundle region, is modeled with a Mithrandir-like model. Finally, the cryostat radiative heat load is neglected and assumed to be removed by the (not included) structure cooling channels; the structure heat capacity, together with that of the pre-load plates, is indeed included in the jackets of the CSMC CICCs.

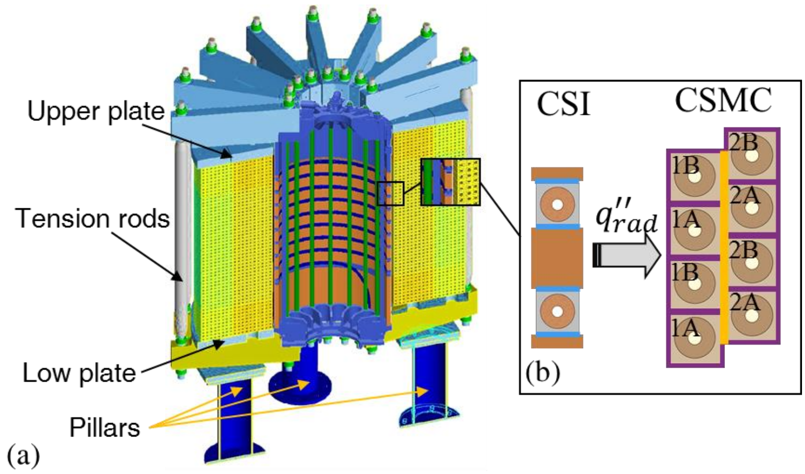

Figure 2.9. CSI test analysis: (a) cross section view of the CSMC with the CSI in its bore-hole. (b) Schematic representation of the radiative heat transfer between the CSI and the CSMC layer 1 (conductors A and B).

Simulation setup

Since the simulation focuses on the thermal-hydraulics of the coils, rather than on the refrigerator operation, the boundary conditions (BCs) for each coil are set using experimental data. In particular, temperature and mass flow rate are prescribed at the inlet and pressure at the outlet. The initial condition is also taken from experimental data at the beginning of the transient.

Comparison between simulation and experimental results

Concerning the results of the simulation for the CSMC CD, the temperature at the outlet of both the inner and outlet modules, see Figure 2.10, has an excellent agreement with the experimental data: the relative discrepancy between the temperature traces reaches a maximum of ~5% (~2% on average) in the first stage of the transient from ~25 to 200 h) and a maximum of ~4.7% (~2.8% on average) during the second stage form ~240 to 400 h; in absolute terms the maximum temperature differences are ~12.9 K (on average ~5.5 K) and ~3.9 K (on average ~1.7 K) during the first and the second stage, respectively. A good agreement in obtained also on the pressure drop, compared for instrumented CSMC conductors see Figure 2.11, at initial and intermediate temperatures during the cooldown. It is worth noticing that the experimental trace of T_{out} reaches the 80 K plateau (from 200 to 280 h) with a certain delay (~40 h) with respect to the computed results. This can be explained with the contribution of the upper and lower CSMC pre-load plates: in the experiment, the bulky SS plates are far from cooling effect of He flowing the WP, and therefore the heat is transferred (slowly) from the plates to the cooling He in the winding by conduction; on the contrary the model accounts for the plates thermal capacity in the jacket of the conductors, so the SS mass is directly (and instantly) cooled by He in the CICCs.

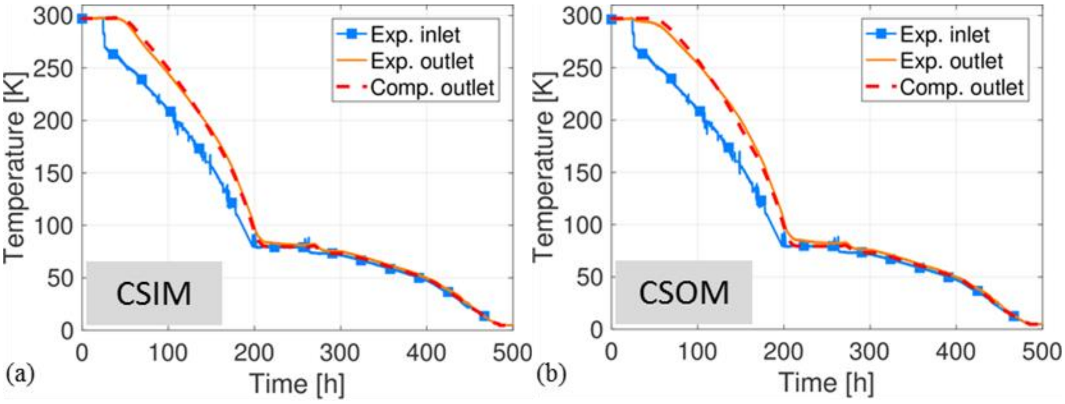

Figure 2.10. CSI test analysis: evolution in the (a) CSIM and (b) CSOM of outlet temperature traces for experimental (thin orange) and computed (thick dashed red) results. The inlet temperature is also reported (light blue with squares).

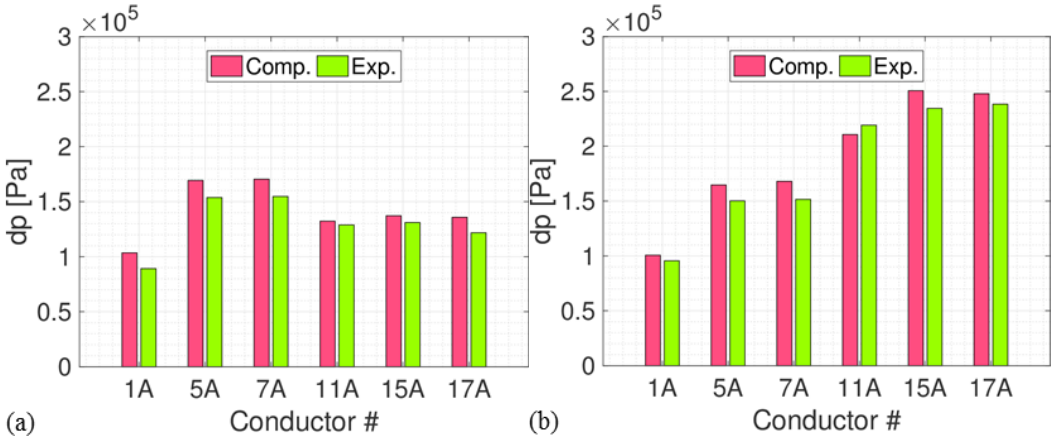

Figure 2.11. CSI test analysis: comparison between computed (pink bars) and experimental (green bars) pressure drops during the CD at (a) 10 h when T_{in} ~300 K and (b) 250 h when T_{in} ~77 K in the instrumented conductors of the CSMC.

Concerning the temperature difference between outlet and inlet ($T_{\text{out}} - T_{\text{in}}$) of both CSMC branches, computed results well capture the experimental measurements, see Figure 2.12, showing an average relative error of ~18% (max 20%) between 40 and 160 h, corresponding to ~6.7 K (max ~13.2 K) in absolute terms. As the 4C model can provide very detailed results during the whole transient, it is worth taking a look at the 2D temperature distribution in the coil during the CD, see Figure 2.13. Even if the total mass flow rate is almost uniformly distributed among all the conductors, with slightly lower values in conductor from 5A to 8B because of their larger hydraulic impedance, since the central channel is delimited by a spring with a smaller diameter (ID = 9 mm, OD = 12 mm) in substitution of the spiral (ID = 10 mm, OD = 12 mm) used in the other conductors [57], the outer layers show an average (and outlet) temperature higher with respect to inner ones: this happens because outer layers, being about two times longer than inner ones, have almost a double heat capacity. In order to reduce the mechanical stress on the coil, it is important to reduce also the radial temperature gradients on the coil cross section.

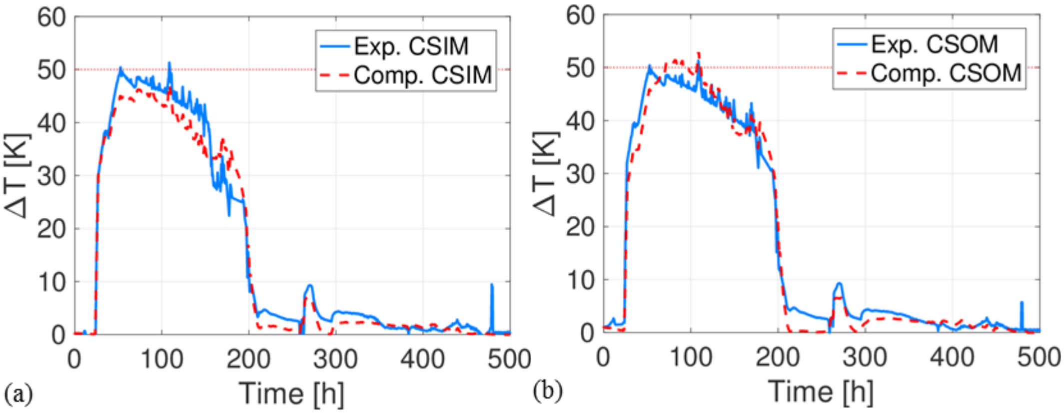

Figure 2.12. CSI test analysis: measured (solid light blue) and computed (dashed red) evolution of the temperature difference between outlet and inlet of (a) CSIM and (b) CSOM.

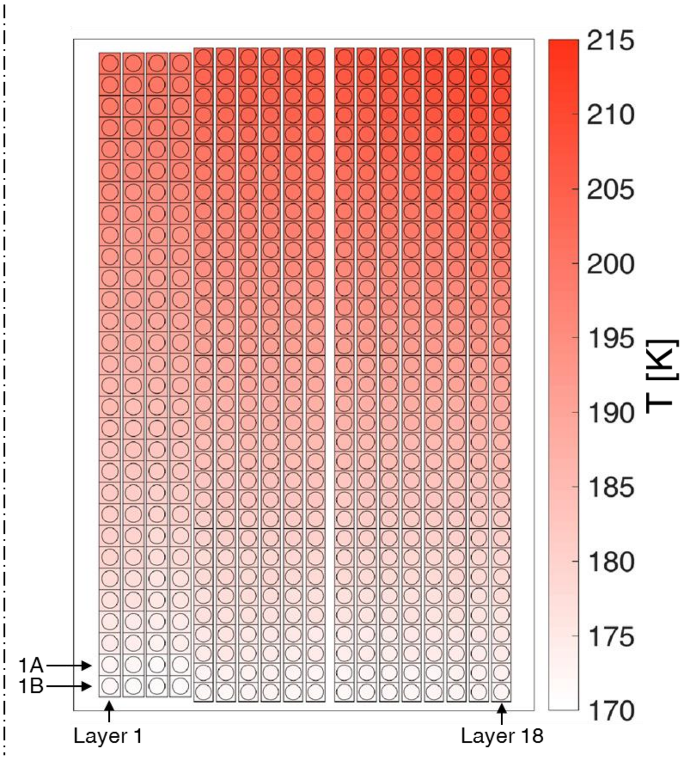

Figure 2.13. CSI test analysis: computed 2D temperature map on the CSMC cross section at ~140 h. The hot-spot temperature is located in the last turn of layer 18 (top right corner). The machine axis is the black dash-dotted line on the left.

Concerning the CSI CD, computed results show a good agreement with experimental measurements, see Figure 2.14. For the structure cooling channel, the sensitivity of the T_{out} has been assessed changing parametrically the value of the heat transfer coefficient multiplier M_{λ}: the best agreement is obtained with $M_{\lambda} = 0.5 \times 10^{-4}$, see Figure 2.14a. Since the structure cooling channel flows near the top and bottom flange, far from the CSI, the coil outlet temperature is almost unaffected by the value of M_{λ}, see Figure 2.14b, because it does not take advantage of the enhanced cooling. Additionally, temperature traces at some locations on the lower and upper spacers on the structures, i.e. sensor T_{MND02} and T_{MND01}, are well reproduced by the computed results see Figure 2.15.

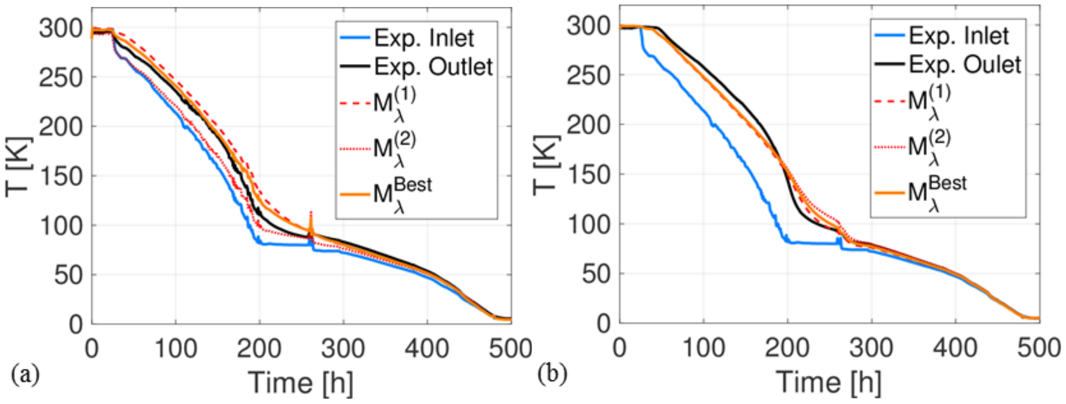

Figure 2.14. CSI test analysis: temperature evolution measured at the inlet (solid light blue) and outlet (solid black) of (a) the structure cooling channel and of (b) the CSI. Computed outlet temperature evolution is reported for different values of M_λ (dashed red, dotted red and solid orange).

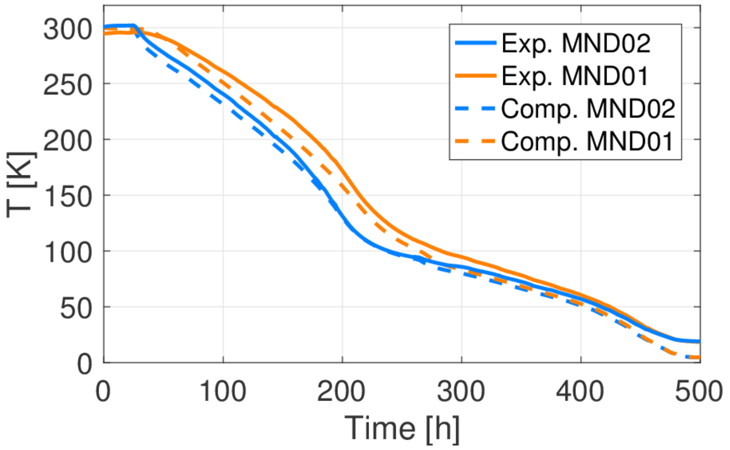

Figure 2.15. CSI test analysis: experimental (solid) and computed (dashed) temperature evolution at temperature sensors on the SS spacers T_{MND02} (light blue, lower spacer) and T_{MND01} (orange, upper spacer)

The comparison between measured and computed maximum temperature difference (ΔT^{max}) on the coil, see Figure 2.16, shows the same qualitative evolution. Nevertheless, the *actual* ΔT^{max} computed is larger. This has been obtained with the difference between the hottest temperature (on the CSI and the structure assembly) and the inlet temperature: at ~200 the temperature difference is ~30–40 K higher with respect to the $T_{\mathrm{out}} - T_{\mathrm{in}}$ measured (and computed) trace. The computed maximum temperatures are located on the top of the upper flange and at the bottom of the lower flange, which are far from the region cooled by the structure cooling channel and CICC. This result advises that to satisfy the constraint on the ΔT^{max}, it would be necessary to install additional temperature sensors not only on the top and bottom of the upper and lower flanges, but in general in the furthermost locations from the cooling channels.

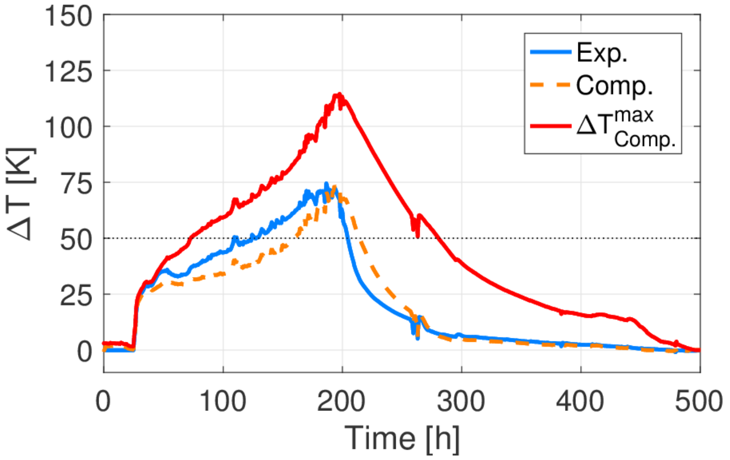

Figure 2.16. CSI test analysis: temperature difference computed as $T_{out} - T_{in}$ for experimental (solid light blue) and computed (dashed orange) results. The computed absolute ΔT^{max} across the CSI and structure is also reported (solid red).

Optimization of the cooldown strategy

Since the validation exercise has been successful and the 4C model developed showed excellent capabilities for the simulation of the CSMC CD and since computational tools should be used to help designers and operators to make better decisions, the model has been used trying to optimize the cooldown strategy, see Appendix B.

2.5.3. AC losses[3]

The tests

As part of the qualification program of the ITER CS conductor, that will be operated in pulsed mode, several tests were carried out to estimate and analyse the AC losses, including also the effect of EM cycling. The tests consist in the exponential dump, with time constant τ_{dump} = ~20 s, of the current I_0 initially flowing in the CSMC (i.e. of the background magnetic field B where the CSI is immersed). During the CSMC current dump, AC losses are induced and therefore the coil temperature increase is

---

[3] Part of the work described in this section was also published in [36].

recorded by the sensors. The recorded data are then used to estimate the energy deposited in the coil through a calorimetric analysis.

Here, the work consists in identifying a set suitable of experimental shots, see Table 2.3, performed after a different number of EM cycles during the campaign. Moreover, since the CSMC and the CSI have a different dump time constant in view of their different inductance, to avoid the superimposition and mix of power deposition caused by currents having different time constants, only shots with zero-current in the CSI has been selected. The calorimetric analysis and a simple mathematical model are used to obtain a general formulation of the AC losses (coupling and hysteresis), to be implemented in the 4C code and then validated against experimental data.

Table 2.3. Operating conditions of selected shot for AC losses analysis ($I_{0,\mathrm{CSI}}$ = 0 kA).

Shot #	**$I_{0,\mathrm{CSMC}}$ [kA]**	**Cycle #**
36-1	23	BoC@
37-1	36.8	BoC
40-1	46	BoC
80-4	23	1000
97-4	23	5000
129-1	23	10000
164-4	23	EoC$
188-4	46	EoC&

@ Test performed before the Beginning Of EM Cycles (BoC).
$ Test performed after the End Of EM Cycles (EoC), namely 16000.
& Test performed after the EoC and after quench tests.

Simplified AC losses analytical model

The simplified analytical model developed, from [36], is able to describe the evolution of the total power deposited and its spatial distribution in the cable during the current dump, by simply using global information deriving from the CSI test.

Coupling losses during exponential magnetic field dump

The evolution of coupling losses per unit length (P_{coup}) in the cable [23] can expressed by:

$$P_{coup}(t) = \frac{n\tau}{\mu_0} \cdot \left(\dot{B}_{int}(t)\right)^2 \cdot A_{st} \tag{14}$$

Variables in (14) are: $n\tau$ [s] the coupling time constant of the cable, μ_0 [H/m] the magnetic permeability of the void, $\dot{B}_{int}$ [T/s] the time derivative of cable internal field and A_{st} [m^2] the total cross section of the composite strands. By assuming $B_{int}(t) = B_{ext}(t)$, equation (14) is applicable for any evolution of B.

Referring to [58] [59], during the exponential dump, a more accurate but less general formulation can be obtained when the cable internal field varies according to:

$$B_{int}(t) = B_{ext}(t) - \dot{B}_{int}(t)\frac{n\tau}{2} \tag{15}$$

with external field provided by the CSMC decaying exponentially for its initial value B_0 according to:

$$B_{ext}(t) = B_0 e^{-\frac{t}{\tau_{dump}}} \tag{16}$$

Solving the differential equation (15) and substituting it in the general formula (14), the final expression for P_{coup}, only during the exponential dump, is:

$$P_{coup}(t) = \frac{n\tau}{\mu_0}\left(\frac{2B_0}{2\tau_{dump} - n\tau}\left(e^{-\frac{2t}{n\tau}} - e^{-\frac{t}{\tau_{dump}}}\right)\right)^2 A_{st} \tag{17}$$

Hysteresis losses

As reported in [23] the hysteresis losses are computed as:

$$P_{hyst} = \frac{2 \cdot J_c \cdot d_{eff} \cdot \left|\dot{B}_{int}(t)\right| \cdot A_{nonCu}}{3\pi} \tag{18}$$

where J_{C} is the local critical current density, A_{nonCu} the cross section of non-Cu material in composite strands and $d_{\mathrm{eff}} = 19.45$ µm is the effective diameter of the superconducting filaments. The latter was determined in [60] by calorimetry, however, since the temperature increase during hysteresis losses measurement (slow linear B ramps, when $P_{\mathrm{hyst}} >> P_{\mathrm{coup}}$) is very small, the value may be affected by a certain degree of uncertainty.

The AC losses model implemented in the 4C code has been used for the CSI experimental tests aimed at measuring specifically the hysteresis losses. In particular, the model has been applied to the simulation of the CSMC charge (first part of shot #36-1), with the current ramping from 0 kA to 23 kA in ~1450 s. The magnetic field inside the CSI is assumed to increase linearly from 0 T to its final value proportionally to the CSMC current.

In the simulation of this transient, both P_{hyst} and P_{coup} are included, but being the latter much smaller (small dB/dt), the effect of P_{hyst} will dominate the heat deposition. A parametric study has been performed on the value of the effective filament diameter d_{eff}.

Unfortunately, the comparison between experimental and computed traces can be done only on temperature TS01, i.e. the sensor at the coil outlet, since it is the only sensors not showing a measurement drift (caused by the magnetic field ramp-up) of the same order of magnitude of the measured ΔT, which is instead observed in all the other sensors.

Figure 2.17 shows that the best results, for the d_{eff} calibration, are obtained with the effective strands diameter increased by ~50%, so the calibrated value corresponds $d_{\mathrm{eff}} = 29.2$ μm. The quite large disagreement between computed and experimental results at the beginning of the transient ($t < 500$ s), is due to the fact that J_C was never measured below 2 T, therefore the model for P_{hyst} is not reliable when $B < 2$ T and that part of the transient cannot be used in the calibration.

As a final remark, note that in principle, the measured inlet temperature TS08 should always be smaller than the temperature TS01 at the outlet: this is not observed, see $t > 1500$ s in Figure 2.17, due to the drift of TS08 signal induced by the magnetic field. Therefore since TS01 returns to its initial value after ~1600 s, it can only be assumed that TS08 is relatively flat, and in any case smaller than TS01 measurement, during the experiment and consequently in the simulation. Therefore, the d_{eff} estimation carried out here is considered acceptable.

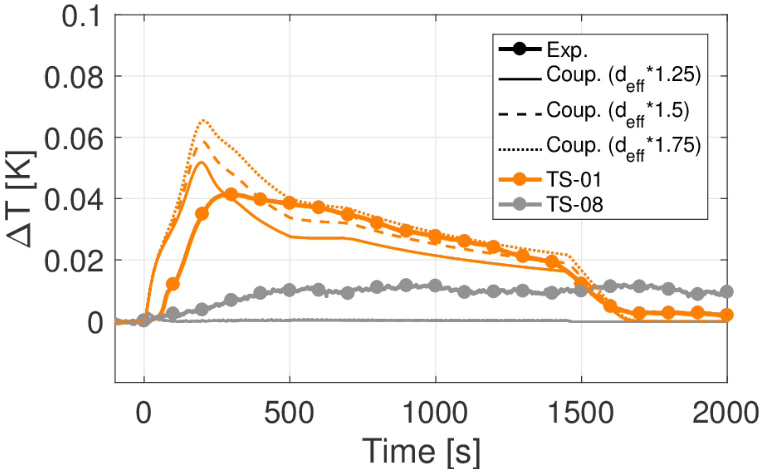

Figure 2.17. CSI test analysis: temperature evolution at TS08 (grey) and TS01 (orange) locations for shot #36-1 during the linear ramp up of the magnetic field; the results for different multipliers of d_{eff} parameter, namely ×1.25 (solid), ×1.5 (dashed), ×1.75 (dotted), are reported.

Using calorimetry to estimate coupling time constant $n\tau$

To obtain the “free” parameters of the constitutive relation for the AC losses, i.e. the value of the coupling time constant $n\tau$, it is necessary to estimate, by means of the calorimetry, the total energy deposited on the cable region between e.g. the temperature sensors TS07 and TS02, see Figure 2.18, which is computed as:

$$E = \int_{t_{dump}}^{\infty} (h_{TS02}(p_{ave}, T_{TS02}) - h_{TS07}(p_{ave}, T_{TS07})) \times \left(\frac{dm}{dt}\right)_{ave} dt \qquad (19)$$

where t_{dump} is the time at which the dump occurs, h_{TSxx} the specific enthalpy evaluated locally for the two sensors and p_{ave} and $(dm/dt)_{\text{ave}}$ are the pressure and mass flow rate averaged between inlet and outlet of the coil.

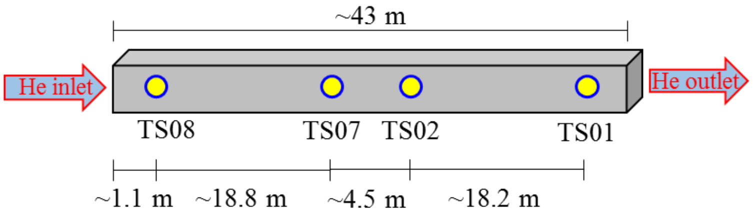

Figure 2.18. CSI test analysis: sketch of the location of considered temperature sensors along the CSI.

The coupling losses (E_{coup}) are obtained by subtracting the energy from hysteresis losses (E_{hyst}) form the total energy deposited:

$$E_{coup} = E - E_{hyst} \tag{20}$$

The time and space integrated value of P_{coup} corresponds to the value of E_{coup} determined from (20), which divided by the volume of the strands, i.e. $A_{st} \cdot (x_{TS02} - x_{TS07})$, returns the energy density per unit volume of composite strands, q'''_{coup}. The value $n\tau$ is found by solving the resulting equality, which can have two different formulations, $n\tau_{\mathrm{A}}$ and $n\tau_{\mathrm{B}}$ respectively, depending of the form of P_{coup} used:

$$n\tau_A = \frac{2q'''_{coup}\tau_{dump}\mu_0}{\overline{B^2}} \tag{21}$$

$$n\tau_B = \frac{2q'''_{coup}\tau_{dump}\mu_0}{\overline{B^2} - q'''_{coup}\mu_0} \tag{22}$$

where the integral averaged square magnetic field between TS07 and TS02 is indicated as $\overline{B^2}$. Equation (21) and (22) are obtained using the P_{coup} formulation from (14) and (17), respectively.

The results of the calorimetric analysis and $n\tau$ estimation are reported in Table 2.4: it is worth noticing that the value of the coupling time constant at the end of EM cycles is larger than the prescribed value of 75 ms [61].

Table 2.4. Main results of calorimetric analysis and $n\tau$ estimation.

Shot #	τ_{dump} [s]	$I_{0,\text{CSMC}}$ [kA]	B_0 [T]	E_{coup} [kJ]	$n\tau_A$ / $n\tau_B$ [ms]
36-1	19.1	23	6.06	0.69	580/590
37-1	19.2	36.8	9.68	1.58	530/530
40-1	18.3	46	12.1	2.17	470/470
80-4	18.5	23	6.4	0.20	174/175
97-4	18.0	23	6.04	0.16	142/143
129-1	18.5	23	6.02	0.14	124/124
164-4	18.9	23	6.04	0.25	220/220
188-4	19.6	46	12.1	0.69	149/149

Benchmark against THELMA model

Using shot #36-1 as reference, to prove the validity of the methodology, the obtained results have been benchmarked against the those provided by the THELMA model [62], the state-of-the art code for electromagnetic analysis in accelerator [63] [64] and fusion superconducting magnets [65], see Figure 2.19.

As described more in [35], in the THELMA model, the hysteresis losses are computed according to the analytical formula (18) and calibrated against experimental data. Concerning coupling losses, the power deposited has been estimated by tuning the transverse conductance per-unit surface between sub-cables to match energy deposited between the temperature sensors TS02 and TS07 determined using (19). For the present benchmark on shot #36-1, the best-fit conductance obtained in [35], is $1.81\times10^9\ \Omega^{-1}\times\text{m}^{-2}$.

Model A (using (21)) and model B (using (22)) take as input the 1D magnetic field profile along the CSI, before the exponential decay with the same time constant of CSMC current dump (τ_{dump} ~19 s). The comparison between computed power evolution and the output of the THELMA model, see Figure 2.19 and Figure 2.20, show that all the approaches are equivalent within 10%, with the power profile reflecting the magnetic field distribution. Small differences are visible among different approaches during the first instants following the current dump, see Figure 2.20, because model A has not an exponential term, like that in (17), which smooths the power peak when *t* ~0 s. Despite this difference, the total energy deposited, corresponding to the E_{coup} value estimated, is the same for all models.

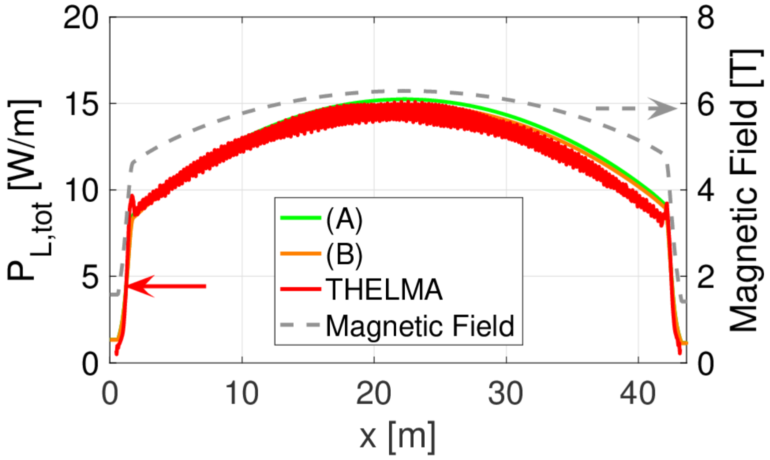

Figure 2.19. CSI test analysis, shot #36-1: total linear power (coupling and hysteresis) density profile, along the CSI, 1 s after the dump start (left axis) according to model A (solid green), model B (solid orange) and THELMA (solid red) results. (b) CSI magnetic field (right axis, dashed grey) profile before the dump.

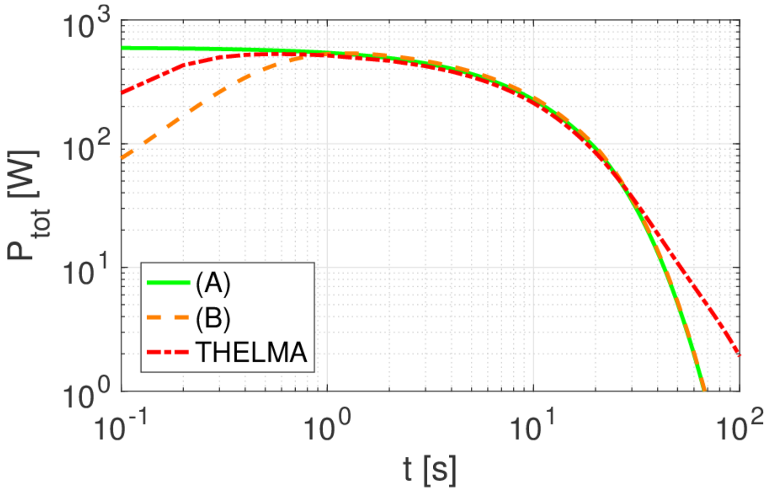

Figure 2.20. CSI test analysis, shot #36-1: evolution of total power deposited in the CSI according to model A (solid green), model B (dashed orange) and THELMA (dash-dotted red) results.

AC losses assessment

After that models A and B have been successfully benchmarked against the THELMA model results, they have been implemented in the 4C code and then validated against experimental data.

Experimental temperature traces at sensors TS07 and TS02 are used as reference for the computed results, see Figure 2.21. The discrepancy between measured and computed temperatures evolution is <11%, see Figure 2.23. Concerning the mass flow rate evolution, the simulation qualitatively captures the phenomenon, see Figure 2.22, but it overestimates the decrease of inlet mass flow rate; the reason behind this are possible issues with the dynamic response of the sensors, as already mentioned in [35].

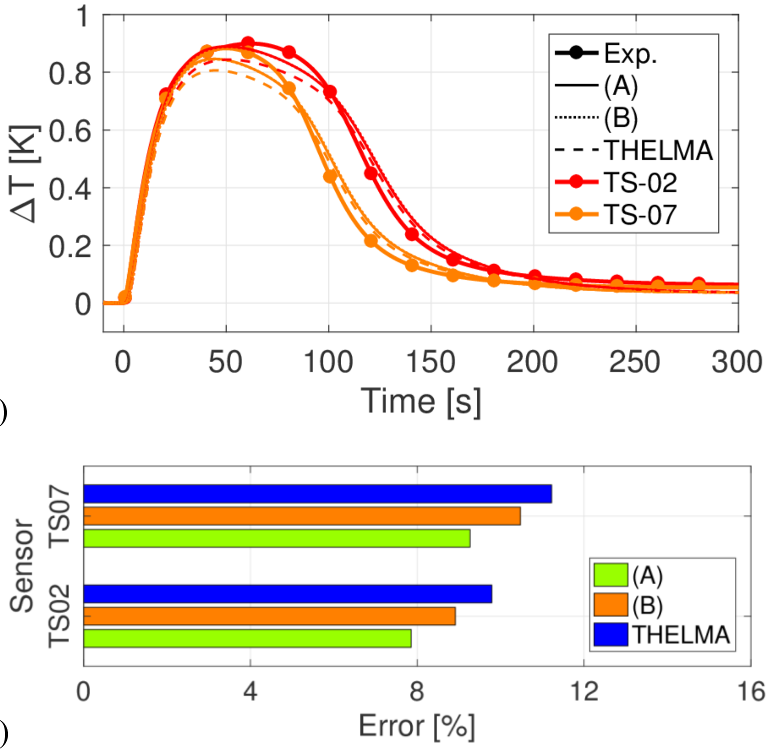

Figure 2.21. CSI test analysis, shot #36-1: (a) temperature evolution at TS07 (orange) and TS02 (blue) sensors locations for experimental data (solid with circles) and computed results using model A (solid line), model B (dotted line) and the input power for THELMA calculations (dashed). (b) Average error between experimental and computed temperature evolution on sensors TS07 and TS02 using model A (green), model B (orange) and THELMA (red).

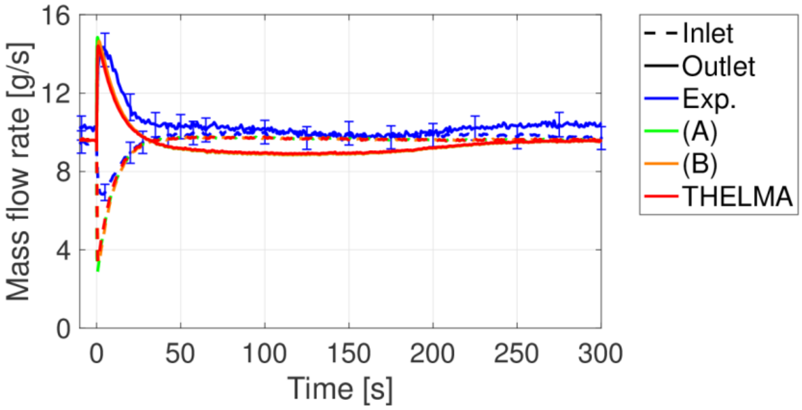

Figure 2.22. CSI test analysis, shot #36-1: mass flow rate evolution at inlet (dashed line) and outlet (solid line) for experimental (blue) and computed results using model A (green), model B (orange) and THELMA (red).

All models are equivalent, but model A is the simplest one and moreover, it is more conservative, with respect to model B, during the initial phase following the beginning of the dump, when the magnetic field and its derivative have the maximum values. For a detailed analysis using a rigorous model derived in the case of linear magnetic field ramps refer to [36]. Here, model A is adopted to validate the methodology against other tests. Results for shot #40-1, see Figure 2.23a, show that the agreement at sensors TS08 and TS01, where the magnetic field has large spatial gradients (dB/dx), is only qualitative. This is a consequence of the fact that the $n\tau$ is computed between TS07 and TS02, where the magnetic field is almost constant and the power deposition is uniform. Near the boundaries this is not true, because of the large B gradients. In any case, since on each turn of the ITER CS, the magnetic field is almost constant, the $n\tau$ value obtained can be applied with a reasonable confidence level.

The mismatch between computed and experimental temperature traces at TS07, TS02 and TS01 location, see Figure 2.23b, is again <11%, while on TS08 it is much larger as a consequence of the large magnetic field gradient in that region. Actually, the temperature increase at TS01 is overestimated as well, since it suffers of the dB/dx like TS08. However. the error on TS01 is smaller, because the sensor is located near the CSI outlet and it measures a higher temperature increase, accounting for the whole energy deposited in the CSI.

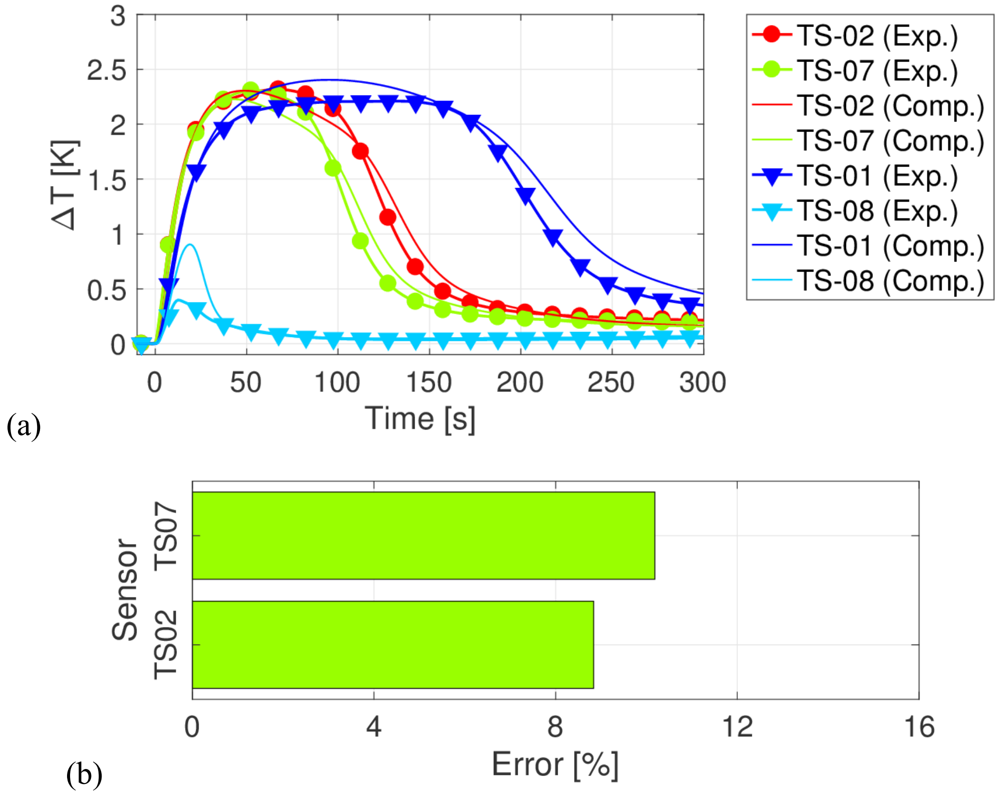

Figure 2.23. CSI test analysis, shot #40-1: (a) Experimental (solid with symbols) and computed (solid line) temperature traces at selected sensors locations using model A. (b) Mismatch on temperature evolution for sensors TS07 and TS02.

2.5.4. Strain

The test performed on the CSI in ITER-like operating conditions allowed to collect data also on the mechanical behavior of the coil. The estimation of the strain applied to the conductor is very important, because of Nb_3Sn critical current sensitivity to strain.

From the analysis of CSI data, the projected value of the strain applied to the ITER CS has been determined [38]: it turned out that the foreseen strain value is smaller, with respect to previous estimation [66], because it has been possible to quantify the beneficial effect of the hoop strain, see Figure 2.24. In fact, the hoop force tends to expand the turns of the CSI coil wound as a solenoid, thus reducing the compressive strain to which the strands are subjected, due to the fact that during the CD the SS jacket shrinks more than the composite strands (thus inducing the thermal strain ε_{cd}). As e.g. the SULTAN tests are performed on a straight, short sample conductor, the hoop force is not present there, while the tests performed in a solenoid inserted in the bore of the CSMC can properly highlight the effect of the same force that will be present in the real coil operation in ITER.

The assessment of the effective strain in the CSI has been carried out in two operation modes: in direct charge, when the CSI and CSMC magnetic field directions are parallel, and reverse charge, when coil currents flow in opposite directions and therefor the CSI is compressed in the hoop direction by the CSMC magnetic field.

As outcome of the analysis carried out in [38], by summing the different strain contributions, namely the thermal ($\varepsilon_{\mathrm{cd}} = -0.59\%$), longitudinal ($\varepsilon_{\mathrm{long}} \approx -0.16\%$) and crush ($\varepsilon_{\mathrm{crush}} = -1.25\times10^{-4}\%$), the effectice strain ε is given by:

$$\varepsilon = -0.4285 - 1.25 \times 10^{-4} \times I \times B\ [\%] \tag{23}$$

where I [kA] is the operating current and B [T] the magnetic field.

Equation (23) will be used in the predictive simulations of the ITER CS operation, see Chapter 3.

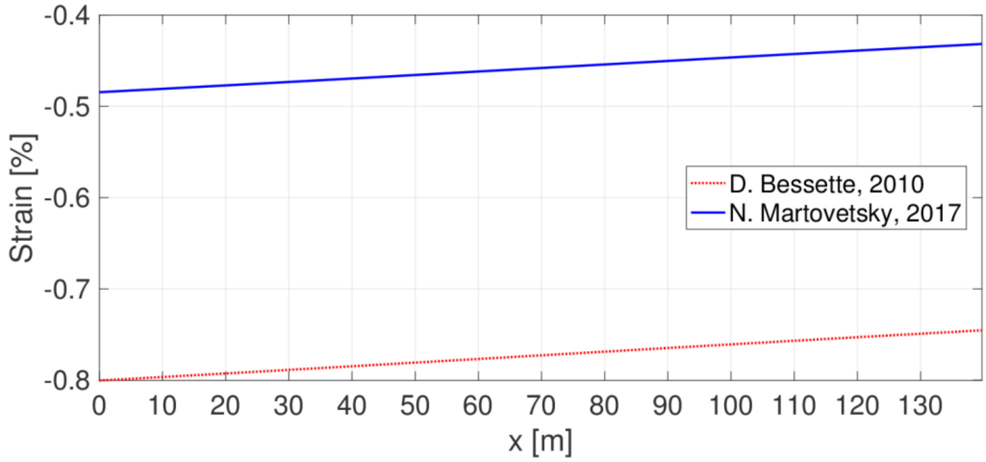

Figure 2.24. Strain profile in pancake #1 of CS1U module at 38 kA according to D. Bessette [66] (red dotted) and N. Martovetsky [38] (blue solid) estimations.

2.5.5. Scaling parameters

The measured scaling parameters of the CSI [38], referred to the scaling formulas in [67], are reported in Table 2.6 and compared to those reported in [67] and [68], here used as reference for the CS operation. The actual effect of the parameters changes on the temperature margin justifies the need for new, detailed simulations of the ITER CS to assess its performance during operation.

Table 2.5. Scaling parameter of the CSI (and CS) conductor. Changes (Δ) with positive effects on T_{CS} are in **bold** characters, those with negative effects are underlined.

Parameter	**Unit**	**Value**		**Δ [%]**
		From [68]	**From** [38]	
C_{a1}	-	45.46	45.74	+0.62
C_{a2}	-	6.52	4.431	-32.04
ε_{0a}	-	2.44×10^{-3}	2.32×10^{-3}	-4.92
ε_{n}	-	-1.7×10^{-4}	-6.41×10^{-4}	-277.1
B_{c20m}	T	30.23	23.9	-20.94
T_{c0m}	K	16.73	16.48	-1.49
C	$A\times T/m^2$	6.4518×10^{10}	8.0771×10^{10}	**+25.19**
p	-	0.56	0.556	**-0.71**
q	-	1.75	1.698	**-2.97**

2.6. Analysis of the TFI tests

In the framework of the TFI experimental campaign, the 4C code has been used to determine the constitutive thermal-hydraulic relations of the conductor and then to predict, i.e. simulate before the test, the quench propagation in coil, in order to assess the predictive capabilities of the 4C code.

2.6.1. Thermal-hydraulic characterization[4]

Experimental data collected during the test campaign have been analyzed to verify the validity of existing friction factor correlations for the hydraulic characterization

---

[4] Part of the work described in this section has been presented in a poster session at the EUCAS 2017 Conference held in Geneva (Switzerland) from Sept. 17-21, 2017. Abstract no.: 3LP1-05.

of the TFI, with dedicated purely hydraulic tests, and to deduce the TH constitutive relations, by means of heat slug tests, to be used in the 4C code for successive analyses, like the quench propagation.

Experimental setup

The TFI conductor, whose geometrical parameters are reported in Table 2.2, is well equipped with lots of sensors installed along the conductor length, see Figure 2.25, including pressure taps, mass flow meters and temperature sensors. The latter are glued on the jacket by removing local insulation, however since the sensors attachment has been performed manually, there are uncertainties on the thickness and the material properties of the glue used, but also on the effectiveness of the thermal contact between sensor and jacket.

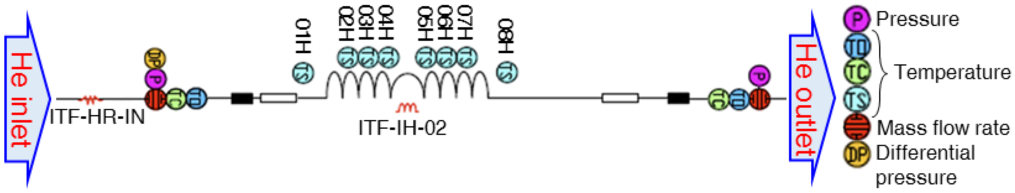

Figure 2.25. TFI test analysis: sketch of thermal-hydraulic diagnostics installed on the TFI.

Thermal−hydraulic constitutive relations in the 4C code

The 4C model of the TFI is based on the Mithrandir-like set of equations, as explained in Paragraph 2.4 and the friction factors adopted in the model are available in literature [69] and are defined as:

Hole

$$f_h = \frac{1}{4}\cdot 0.3164\cdot\left(\left(\frac{dm}{dt}\right)_h\cdot\frac{D_{eh}}{\mu A_h}\right)^{-0.25} \qquad (24)$$

Bundle

$$f_b = \frac{1}{4}\cdot C\left(\left(\frac{dm}{dt}\right)_b\cdot\frac{D_{eb}}{\mu A_b}\right)^{-0.52} \qquad (25)$$

where μ is the dynamic viscosity; in (24) $D_{eh} = 3.18$ mm and $A_h = 0.25 \times \pi \times (D_{int,spiral})^2$; in (25) $C = 2.46$, $D_{eb} = 0.25$ mm and $A_b = \varphi \times 0.25 \times \pi \times (D_{int,jkt}^2 - D_{ext,spiral}^2)$, with φ as the bundle void fraction.

It must be remarked hydraulic impedance of the ITER TF conductor, estimated with the combination of (24) and (25), see Figure 2.26, is smaller than the one obtained with the set of friction factor correlations from [70] used as reference up to the present analyses.

Hydraulic characteristic

Following a similar procedure to that adopted for the CSI (see Paragraph 2.5.1), with the data collected during the pure hydraulic tests and during the steady-state operation of the coil, the results showed that the set of correlations is able to reproduce the hydraulic characteristic in the expected operating range, see Figure 2.26, with an average relative error of ~6% at the expected nominal value of mass flow rate (~8 g/s). Moreover, a 10% increase of the friction factor in both He regions by means of a multiplier (FF_{h} for hole, FF_{B}, for bundle) leads to a better description of the flow speed (v_{ave}), see Figure 2.27. The calibrated value for the multiplier is reasonable given the intrinsic uncertainties of the original measurements and correlations presented in [69]. Friction factor correlations adopted in a previous work [70] turned out to overestimate the foreseen Δp of about ~70%, at the nominal mass flow rate, when compared with experimental data.

The expected mass flow rate repartition at the nominal mass flow rate, see Figure 2.28, is ~49% in the bundle and ~51% in the central channel, coherently with the results obtained in [69]. Note that the mass flow rate repartition is not affected by the value of the friction factor multiplier, because the ratio between the Δp in the hole and in the bundle region is unchanged.

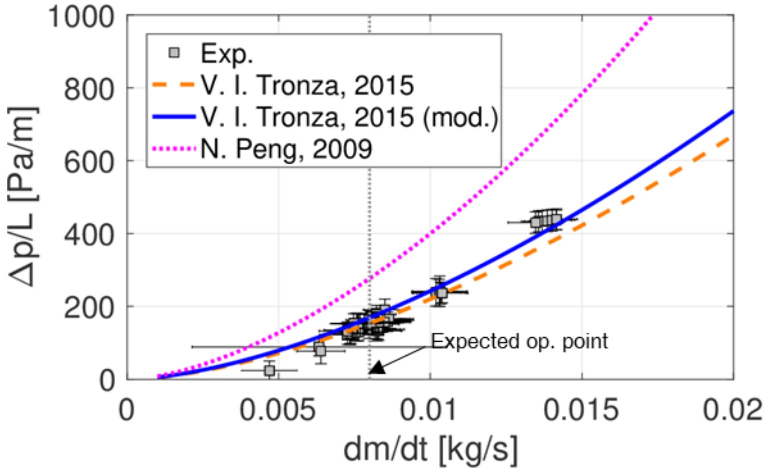

Figure 2.26. TFI test analysis: hydraulic characteristic of the TFI coil showing the experimental data (grey squared) and computed results according to [69] with $FF_h = FF_b = 1.0$ (dashed orange), $FF_h = FF_b = 1.1$ (solid blue) and according to [70] (dotted magenta).

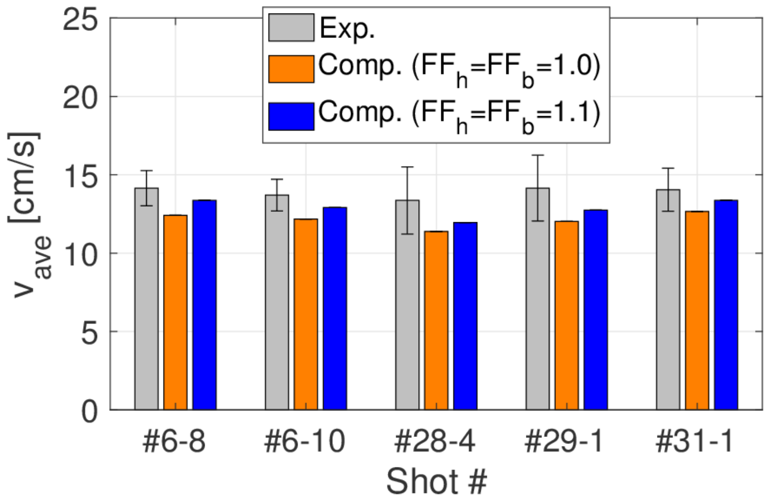

Figure 2.27. TFI test analysis: average flow speed estimated from experimental data (grey bars) computed using correlations from [69] with $FF_h = FF_b = 1.0$ (orange bars) and $FF_h = FF_b = 1.1$ (blue bars).

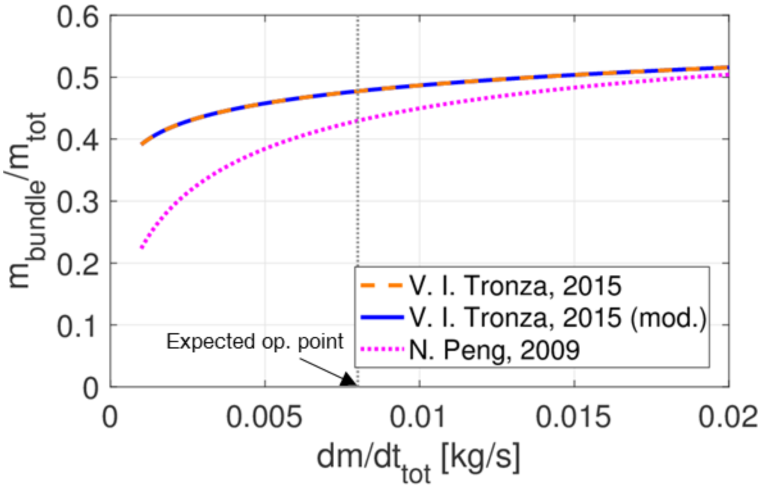

(a)

Figure 2.28. TFI test analysis: fraction of the bundle mass flow rate in the TFI conductor using correlations from [69] with $FF_h = FF_b = 1.0$ (dashed orange), $FF_h = FF_b = 1.1$ (solid blue), and according to [70] (dotted magenta).

Calibration of 4C code thermal−hydraulic input parameters

Hole−Bundle HTC calibration

Adopting the suitable friction factor correlations, dedicated simulations have been performed to calibrate the hole−bundle thermal coupling, taking as reference a heat slug shot (#31-1) performed using a resistive heater (ITF−HR−IN) at the inlet of the TFI, see Figure 2.25. The BCs are prescribed using the experimental data: inlet temperature and mass flow rate and outlet pressure.

To fit the temperature traces of sensors TS08, TS06, TS03 and TS01, the hole−bundle HTC has been calibrated varying parametrically a dedicated multiplier (H_{HB}) of the HTC through the perforated region of the spiral, see Figure 2.4. The best results are obtained with the multiplier $H_{HB} = 8$, see Figure 2.29, similarly to [37] and in the same ball park of other ITER conductors, where H_{HB} is usually ~10. Then to confirm and validate the fitting value of the multiplier (which has thus been frozen), other heat slugs have been simulated (shots: #6-1, #6-2). These shots have been triggered by an inductive heater (ITF−IH−02) located at half length of the conductor and computed results showed an excellent agreement with the experimental measurements, see Figure 2.30.

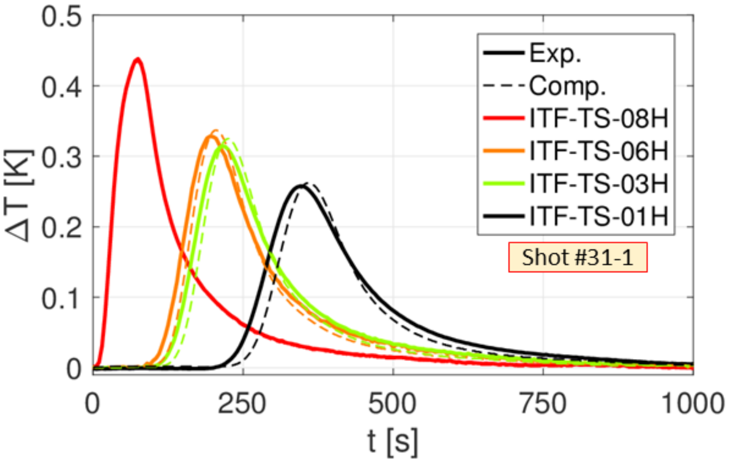

Figure 2.29. TFI test analysis: thermal-hydraulic characterization. Comparison between experimental (thick solid) and computed (thin dashed) temperature evolution at selected sensor locations (TS08 in red, TS06 in orange, TS03 in green and TS01 in black) for resistive heat slug #31-1.

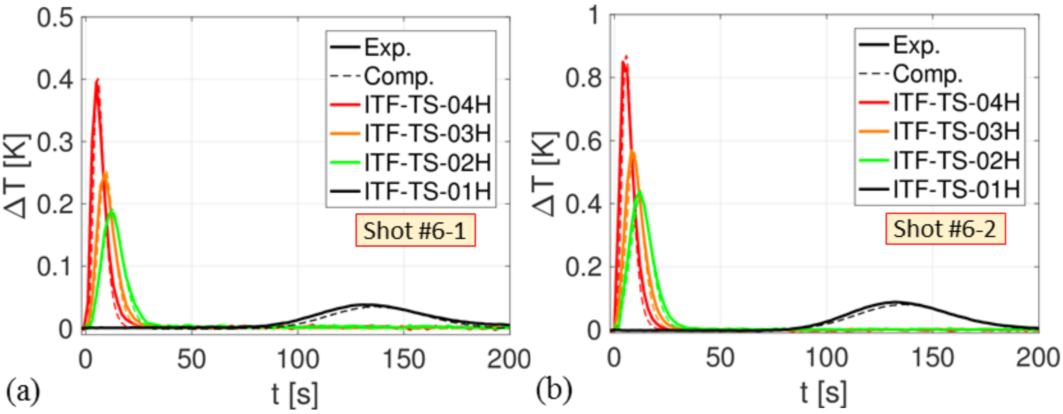

Figure 2.30. TFI test analysis: thermal-hydraulic characterization. Comparison between experimental (thick solid) and computed (thin dashed) temperature evolution at selected sensor locations (TS08 in red, TS06 in orange, TS03 in green and TS01 in black) for inductive heat slugs (a) #6-1 and (b) and #6-2.

Conductor–mandrel HTC calibration

The second parameter to be calibrated is the HTC between the conductor jacket and the supporting structure (HTC_{MND}), on which the coil is wound and kept in position by means of some internal structures built alternating SS clamps and G10 spacers, see Figure 2.31a and b. The calibration of HTC_{MND} is rather interesting since, here, the G10 spacer acts equivalently to the turn insulation of TF conductor in contact with the SS radial plates, like in ITER, or directly with the casing, like in the EU DEMO TF. The structure is included in the model and discretized in eight 2D cross section alternating clamps and spacers accounting for the correct heat capacity, while the heat is transferred through the turn-insulation, which surrounds the conductor inside the grooves of the mandrel, see Figure 2.31c.

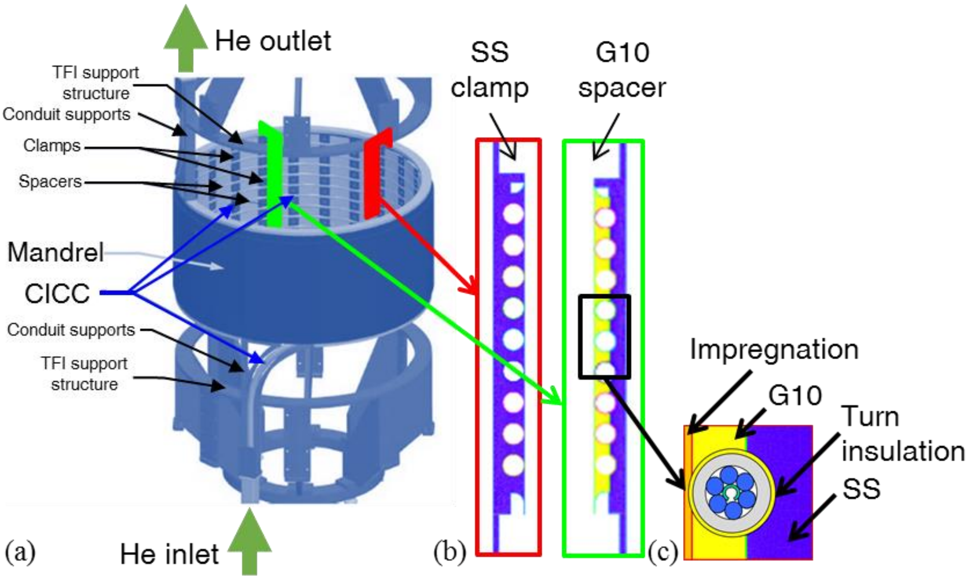

Figure 2.31. TFI test analysis: representation of (a) the supporting structure showing the various components with (b) view of the structures cross sections adopted in the model and (c) the zoom of the contact region between the conductor and the mandrel.

In this framework, the T_{CS} measurement shot #134-1 has been used as reference for the simulation, in particular the portion running until the maximum temperature is smaller than T_{CS}–0.5 K so that the Joule heat generation in the cable can be reliably neglected. The value of HTC_{MND} has been varied parametrically trying to minimize the error on the temperature evolution at different local sensors computed as:

$$\varepsilon_{tot} = \sqrt[8]{\sum_{xx=01}^{08} \frac{\left\| T_{xx,exp} - T_{xx,comp} \right\|}{\left\| T_{xx,exp} - T_{ref} \right\|}} \tag{26}$$

where ε_{tot} is the arithmetic mean value, T_{xx} is the experimental (*exp*) or computed (*comp*) temperature evolution at the eight local sensors (TS)*xx* and T_{ref} = 4.5 K is the reference temperature.

The minimum error is obtained with HTC_{MND} = 1.5 W/mK at 4.5 K, see Figure 2.32a, with simulated results showing a good agreement with experimental measurements on the jacket temperature sensors, see Figure 2.32b.

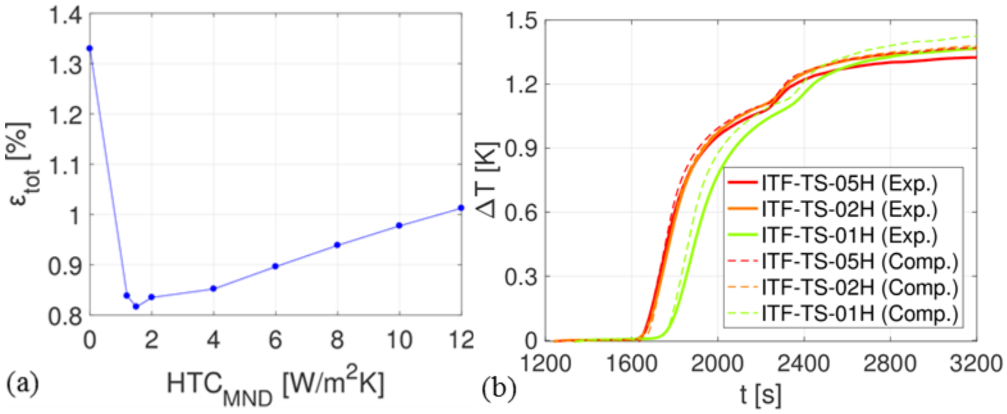

Figure 2.32. TFI test analysis, shot #134-1: (a) geometric error on all temperature evolutions as function of HTC_{MND} at 4.5 K; (b) Comparison between measured (thick solid) and computed (thin dashed) temperature evolution at selected sensors locations (TS05 red, TS02 orange and TS01 green).

2.6.2. Strain

The strain applied to the TFI determined in [41] is smaller than in the previous estimation [66], see Figure 2.33, because of the beneficial effect of the hoop strain previously not accounted. The hoop strain, in fact, helps reducing the compressive strain on the strand induced by the CD as explained in Section 2.5.4.

The effective strain ε in the charged cable has been calculated from the T_{CS}, as measured during the test campaign at different operating currents, according to:

$$E(T) = \frac{E_0}{LA}\int_0^L \int_A \left(\frac{J_{op}}{J_C(B,T,\varepsilon)}\right)^n dAdl \qquad (27)$$

where E [V/m] is the electrical field, A [m^2] the cable area, L the distance between the voltage taps for T_{CS} measurements, E_0 = 10 μV/m is the critical electric field, J_{op} the operating current density, J_{C} the critical current density as function of the magnetic field, temperature and the strain.

Solving for ε after the 5th WUCD, the effective strain used as reference for the simulation of the ITER TF operation, is defined as:

$$\varepsilon = -0.5446 - 2.83 \times 10^{-4} \times I \times B \text{ [\%]} \qquad (28)$$

where I [kA] is the operating current and B [T] the magnetic field. It must be noted that the estimated strain is in the range of the expected range reported in [61].

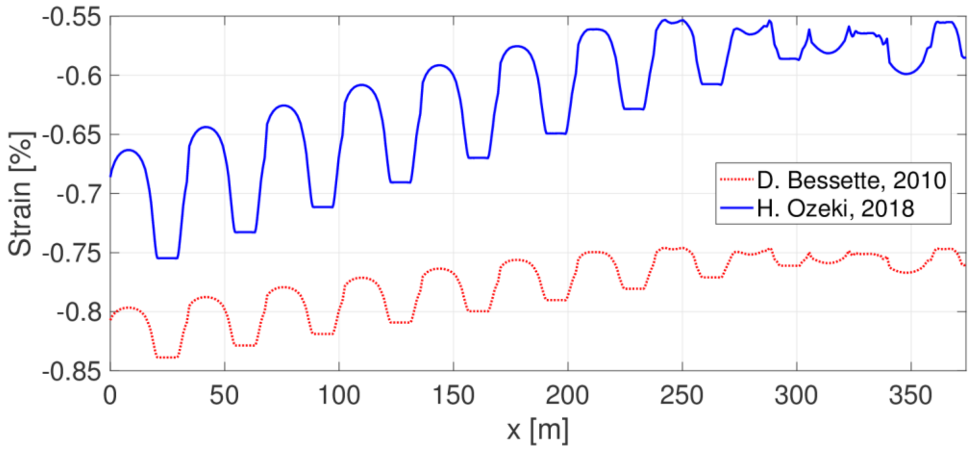

Figure 2.33. Strain profile in pancake P1 of ITER TF coil according to [66] (red dotted) and [41] (blue solid).

Nevertheless, it must be remarked that the hoop strain in the TF coil might not be the same as the hoop strain in the TF insert coil. This is due the fact that the ITER TF coil is supported by very massive and rigid radial plates made of stainless steel, which will presumably prevent the coil from the same level of “expansion” due to the hoop load compared to the situation in the TF insert coil. In other words, the effective strain measured for the TF insert coil may not be straightforwardly applied on the TF coil, but a rigorous projection, as done in [38], has not been performed or published yet to the best of the author’s knowledge and therefore this, maybe overoptimistic assumption has been made.

2.6.3. Scaling parameters

The measured scaling parameters of the TFI are reported in Table 2.6 and compared to those reported in [71] used for ITER conductors. Given the changes in the parameters, it is difficult to estimate the effect in terms of temperature margin, during the operation. Therefore, predictive simulations of the TF coil operation are needed, and these will be presented in Chapter 4.

Table 2.6. Scaling parameter of the TFI (and TF) conductor from [71] and [42]. Changes (Δ) with positive effects on $\Delta T_{\mathrm{marg}}^{\mathrm{min}}$ are in **bold** characters, those with negative effects are underlined.

Parameter	**Unit**	**Value**		**Δ [%]**
		From [71]	**From** [42]	
C_{a1}	-	45.46	47.02	+3
C_{a2}	-	6.52	11.76	**+80**
$\varepsilon_{\mathrm{0a}}$	-	2.44×10^{-3}	2.31×10^{-3}	-5
ε_{n}	-	-1.7×10^{-4}	3.97×10^{-4}	+333.5
B_{c20m}	T	30.23	32.35	**+7**
T_{c0m}	K	16.73	16.22	-3
C	$\mathrm{A}\times\mathrm{T/m}^2$	6.4518×10^{10}	1.2151×10^{11}	**+88**
p	-	0.56	0.84	+50
q	-	1.75	2.57	+47

2.6.4. Effect of electro-magnetic and thermal cycles

During the TFI coil test campaign the evolution of the T_{CS} after electro-magnetic and thermal cycles was observed [41]. Experiments gave evidence that the T_{CS} degradation due to AC losses stops after 1000 EM. However, repeated thermal cycles, i.e. warm-up and cooldown (WUCD) together with quench tests, showed a T_{CS} degradation of ~0.1 K/cycle without any saturation trend, see Figure 2.34. However, the "conservative extrapolation of results to ITER itself shows sufficient margin" [72] satisfying the acceptance threshold of 5.1 K, which is lower with respect older requirements of 5.7 K [61], due to different effects that were not accounted for [73]. The reason behind the observed degradation in still under investigation (conductor or measurement issue?), therefore it will be important to limit as much as possible the number of thermal cycles of the real ITER TF coils.

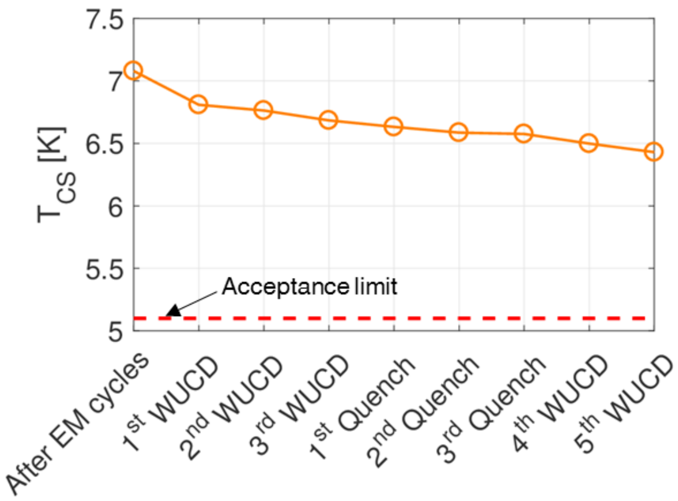

Figure 2.34. TFI test analysis: TFI T_{CS} evolution during EM and thermal cycles, reproduced with data taken from [41].

2.6.5. Quench propagation[5]

One of the most interesting phenomenon for the superconductor science and technology community is the quench propagation. Since the early stages in the 1980s to latest tests on the ITER insert coils, many experimental and computational studies have been devoted to this topic, starting from the QUench Experiment on Long Length (QUELL) [74] [75], followed by a long series of ITER Insert coils [76] [77] [78] [79] [80].

However, even if the quench-related literature database is quite wide, the validation of existing thermal-hydraulic computational tools is far from being ordinary business. When talking about TH predictive simulations of superconducting fusion magnets, the work presented in [42] represents the first attempt ever, to the best of the authors’ knowledge at the time of the paper publication. In this work, the 4C code has been used to strictly predict the quench propagation in the TFI, i.e. performing the simulations before the tests of 2017 campaign.

Experimental setup

During the latest ITER TFI experimental campaign, several tests were devoted to the analysis of the quench propagation, see Table 2.7, with special attention to the propagation speed and hot-spot temperature ($T_{\text{hot-spot}}$). The TFI, in addition to the

---

[5] Part of the work described in this section was also published in [42].

thermal-hydraulic diagnostic shown in Figure 2.25, is equipped with several voltage taps along its length, see Figure 2.35.

Table 2.7. Summary of quench tests performed during the TFI test campaign.

Shot #	t_{delay} **[s]**	**IH**	V_{DC} **[V]**	$\int I^2 dt$ **[A^{2}s]**
109−11	3	IH02	80.0	640
120−6	5	IH02	80.0	652
113−10	7.5	IH02	82.7	676
118−8	3	IH01+IH02	132.2	711
120−5	3	IH02	90.5	806

Quench tests were performed in ITER-like operating conditions, i.e. transport current $I_{\text{TFI}} = 68$ kA and peak magnetic field $B_{\text{peak}} = 11.8$ T (10.8 T CSMC background field plus 1 T self-field). During the tests, one (or two) inductive heater (IH, ITF−IH−02), located on the central turn of the TFI coil, is used to trigger the quench using a 40 ms pulse with increasing amounts of energy deposition ($\int I^2 dt$). The quench detection (QD) system uses the voltage signal across the entire coil (ITF−VD−ALL): if at any instant the time integral of the total voltage on the previous 0.1 s is larger than the QD threshold of 0.01 V × s, a signal of quench detection is triggered by the protection system. Then, the quench freely propagates for t_{delay} seconds (with increasing values: 3 s, 5 s, 7.5 s) before the TFI current is dumped on an external resistor, see Figure 2.36. The CSMC current is dumped about ~0.45 s after the TFI to avoid the burn-out of the TFI due to the transformer effect. Concerning the choice of the delay times, the maximum value of 7.5 s was chosen to have a Joule energy deposition similar to that expected in the ITER TF coil. The ITER design criteria [61] prescribes a delay $\tau_{\text{det}} = 2$ s after the QD, during which the joule energy deposited ($E_{\text{J,det}}$) is equal to:

$$E_{J,det} = R I_0^2 \tau_{det} \tag{29}$$

After the dump, the current will be discharged with a dump time constant of $\tau_{\text{curr}} = 11$ s according to:

$$I(t) = I_0 \exp\left(-t/\tau_{dump}\right) \tag{30}$$

Assuming that during the discharge the electrical resistance is constant, the joule energy deposited ($E_{\mathrm{J,dump}}$) is computed as:

$$E_{J,dump} = R\int_0^{+\infty}\left(I(t)\right)^2 dt = RI_0^2\frac{\tau_{curr}}{2} \tag{31}$$

So the total energy deposited in the ITER TF during a quench is:

$$E_J = E_{J,det} + E_{J,dump} = RI_0^2\left(\tau_{det} + \frac{\tau_{curr}}{2}\right) \tag{32}$$

And therefore, for the TFI it corresponds to:

$$E_J = RI_0^2\left(t_{delay} + \frac{\tau_{curr,TFI}}{2}\right) \tag{33}$$

Since the $\tau_{\mathrm{curr,TFI}}$ is negligibly small (~0.1 s) with respect to t_{delay}, it can be inferred that for the TFI:

$$t_{delay}^{MAX} = \tau_{det} + \frac{\tau_{curr}}{2} \tag{34}$$

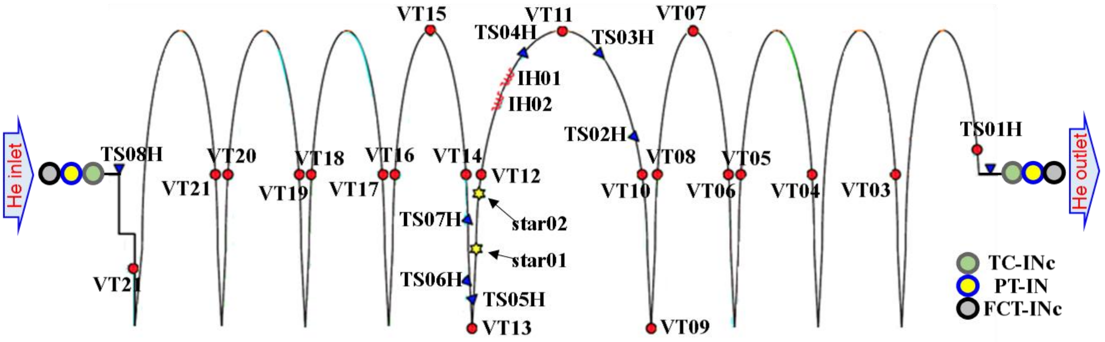

Figure 2.35. TFI test analysis: sketch of the quench-relevant instrumentation on the TFI, indicating voltage taps (VT, star) and temperature sensors (TS).

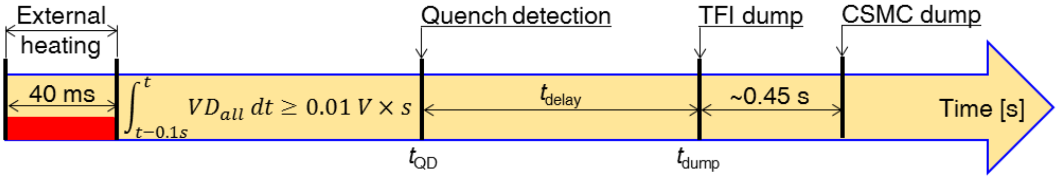

Figure 2.36. TFI test analysis: timeline of a typical quench test on the TFI.

Quench predictive simulations

Simulation setup

TFI quench prediction simulation focused on the case with $t_{\mathrm{delay}} = t_{\mathrm{delay,max}} = 7.5$ s, because since the quench is a reproducible phenomenon, propagations with shorter delay times were naturally included. The simulation stopped at the dump of the TFI current.

The input parameters included:

- Total length, including joint regions, of the conductor and respective BCs: for the sake of simplicity, constant p_{in} ~5.6 bar, p_{out} ~5.5 bar, and fixed $T_{\mathrm{in}} = 5.7$ K, unless backflow occurs at the inlet of the coil;
- Magnetic field map $B(x)$ and hoop strain distribution along the conductor [81], see Figure 2.37. The total strain is given by the superposition of the hoop strain, the thermal strain (−0.7%) and the extra strain (−0.04%). The latter was calibrated with the analysis of TFI T_{CS} measurements in the TFI, as done for the CSI coil [39];
- The n-index = 5 value for the superconducting-to-normal transition, calibrated with the analysis of the T_{CS} measurements for the TFI;
- The initial condition: linear pressure drop profile from the inlet to the outlet, corresponding to the initial mass flow rate value of ~8 g/s, with flat initial temperature profile at T_{in};
- Repartition, between cable and jacket, of the linear power density to be applied for quench initiation (20% cable, 80% jacket), to mimic the IH power deposition. Since the quench propagation is not affected by the quench initiation energy, a sufficiently high energy is used (~110 J), which is not dissimilar to the estimated minimum quench energy (MQE) of ~82 J. The external energy disturbance is deposited during a 40 ms pulse on 0.112 m (corresponding to the IH length and location);
- Constitutive TH relations and scaling parameters as described in Paragraph 2.6.1 and 2.6.3, respectively;
- Numerics: adaptive time-step (from 0.5 to 100 ms) and mesh size (from 0.25 to 100 mm), as result of dedicated convergence study.

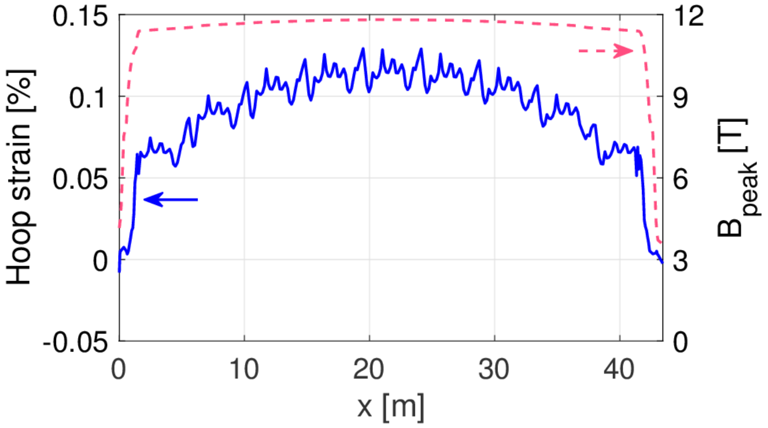

Figure 2.37. TFI test analysis: hoop strain (solid blue, left axis) and peak magnetic field (dashed pink, right axis) profiles along the TFI.

Simulation results

All the results reported are synchronized at the time of the QD, so that they are plotted as a function of $t^* \equiv t - t_{QD}$, since the predictive exercise focuses only on the propagation of the quench and not on the initiating phase, which is indeed beyond the scope of the work.

The take-off of the local voltage signals upstream and downstream the IH, see Figure 2.38, show that the quench propagates progressively in both directions. The slope change in the voltage evolution, for instance at $t^* \sim 0$ s for sensor ITF−VD−1112g or at $t^* \sim 2$ s for sensors ITF-VD−1011g and ITF−VD−1213g, are a consequence of the fact that, at those times, the entire length between the respective taps is normal. Then, looking at ITF−VD−1112g, when $t > 0$ s, the additional voltage increase is slower and related to the well-known increase of Cu resistivity with increasing temperature. Using the local voltage traces, the position of the quench front during the propagation can be deduced and represented on the characteristic (x,t) plane, see Figure 2.39: when the voltage measured between a certain tap A and its neighbour B, in the quench propagation direction overcomes 1 mV (threshold chosen to avoid noise in sensors measurements), the quench front is assumed to pass the A location.

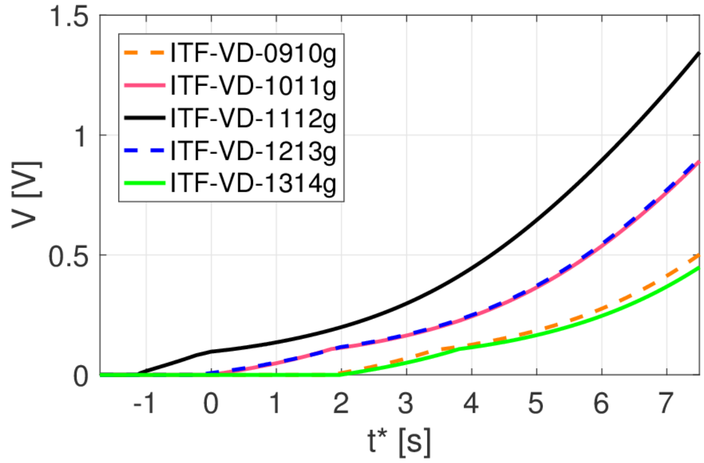

Figure 2.38. TFI test analysis: predicted evolution of the local voltages.

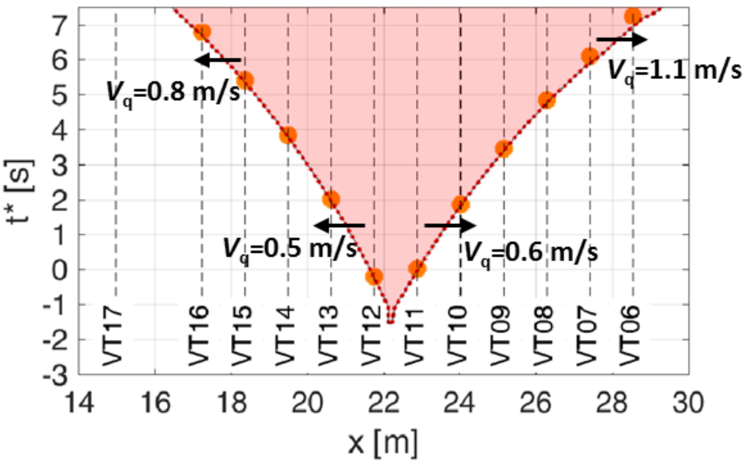

Figure 2.39. TFI test analysis: predicted normal zone propagation in the (*x*,*t*) plane with t_{delay} = 7.5 s.

Figure 2.39 allows to fairly compare the computed and experimental results for the quench front propagation. However, since the voltage taps identify *discrete* points, to follow *continuously* the quench front, the trajectory of points were $I = I_C$ is also reported. The quench propagation speed V_q is computed using the difference between the times at which the quench front passes B and A and the distance between neighbouring voltage taps (A and B), showing the quench front acceleration typical of ITER CICCs [82].

As for the CSI [37], the computed average He flow speed, see Figure 2.40a, confirms the pressure-driven nature of the transient. Flowing towards the boundaries, the hot helium preheats the cable originating longer and longer low temperature margin regions, see Figure 2.40b, before the arrival of the quench front, which thus tends to accelerate finding a warmer cable during its advancement.

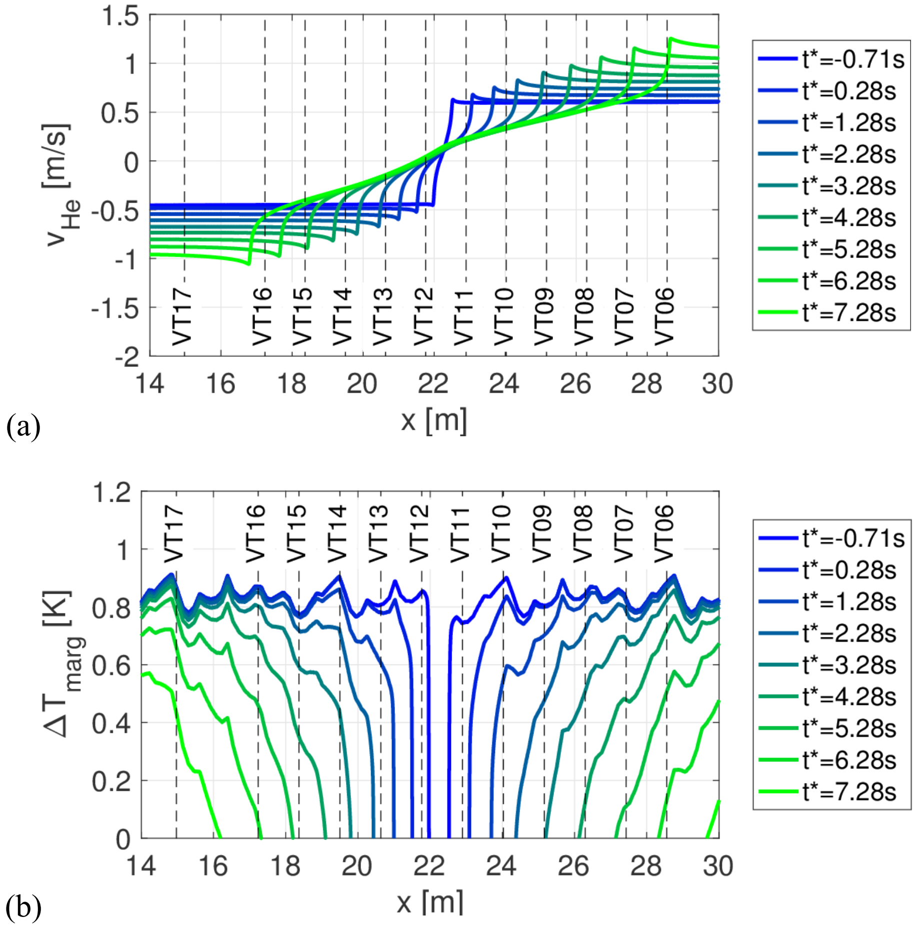

Figure 2.40. TFI test analysis: predicted (a) average He flow speed profile and (b) temperature margin in the TFI at different times of during the quench propagation.

Since it is not possible to directly measure the hot-spot temperature in the cable, a virtual-sensor, see Figure 2.41, is introduced: using the voltage measured by the couple of taps across the IH (here ITF−VD−1112g) and being the temperature dependence of the Cu electrical resistivity well known from material property (e.g. those from the NIST databases [83]), it is possible to infer the $T_{\text{hot-spot}}$. Assuming that the cable segment between voltage taps VT11 and VT12 is totally normal and with uniform temperature (T_{1112}) profile, the $T_{\text{hot-spot}}$ can be determined from VD_{1112} = VT12 − VT11 measurement, following a well-known method [76] [79]:

$$VD_{1112} = \rho_{el,Cu}(T_{1112}) \times \left(\frac{L_{1112}}{A_{Cu}}\right) \times I_{TFI} \tag{35}$$

where $\rho_{el,\mathrm{Cu}}$ is the Cu electrical resistivity, L_{1112} the strands length between VT11 and VT12, A_{Cu} the total Cu cross section. For conservative reasons, it is assumed that the whole current (I_{TFI}) flows in the Cu. However, the code can provide the actual $T_{\text{hot-spot}}$, clearly larger than the virtual-sensor signal, since the temperature profile between VT11 and VT12 is peaked and not uniform, see Figure 2.41b.

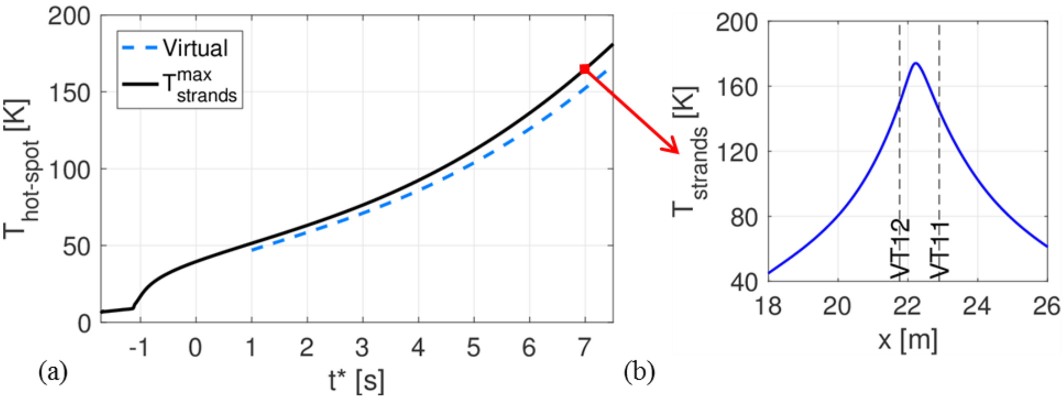

Figure 2.41. TFI test analysis: (a) computed virtual hot-spot temperature (dashed light blue) and maximum strands temperature (solid black) evolutions from predictive simulations. (b) Strands temperature profile at t^* ~7.3 s where the non-uniform T profile between VT12 and VT11 is clearly visible.

Concerning the hydraulic evolution of the quench, during the initial heat deposition, the coil starts pressurizing, see Figure 2.42, and on the sound time scale the mass flow rate at the coil boundary reacts to the disturbance, inducing backflow at the inlet. At the end of the heating phase, the pressure quickly returns to the initial value, but when the normal zone Joule heating takes-off, pressure rises violently, until the pressure wave, propagating at sound speed, reaches the coil boundaries and pushes the He out. A second slower pressurization follows, influenced by the inertia of the circuit.

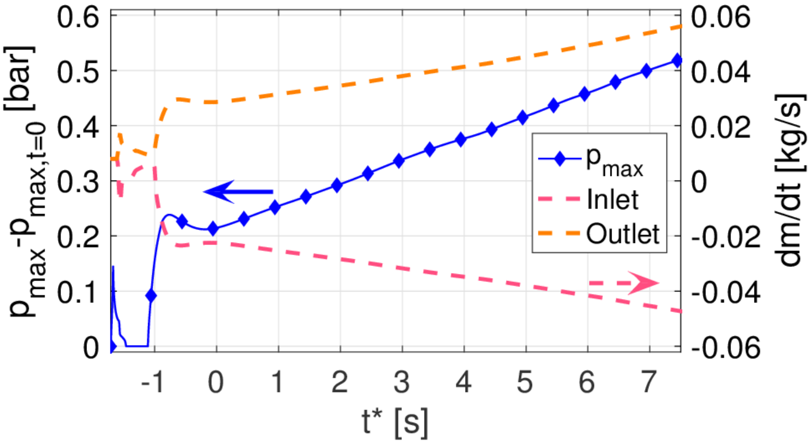

Figure 2.42. TFI test analysis: evolution of maximum pressurization in the TFI CICC (solid blue, left axis) and mass flow rates (dashed, right axis) at the inlet (pink) and outlet (orange) of the TFI.

Experimental results

As done for the predictive simulation, the experimental results are synchronized at the quench detection time *t** and they show a nice reproducibility on total and local voltage traces, see Figure 2.43.

The normal zone is initiated between VT11 and VT12 (IH location) and the propagation of the quench front, deduced from the experimental local voltage traces, shows an excellent reproducibility, see Figure 2.44. The propagation of the quench front is almost symmetric with respect to the initiation zone with a slightly higher speed downstream because of the He flow direction. As the quench propagates, the front accelerates in both directions, from the initial speed of ~0.5 m/s to above 1.5 m/s.

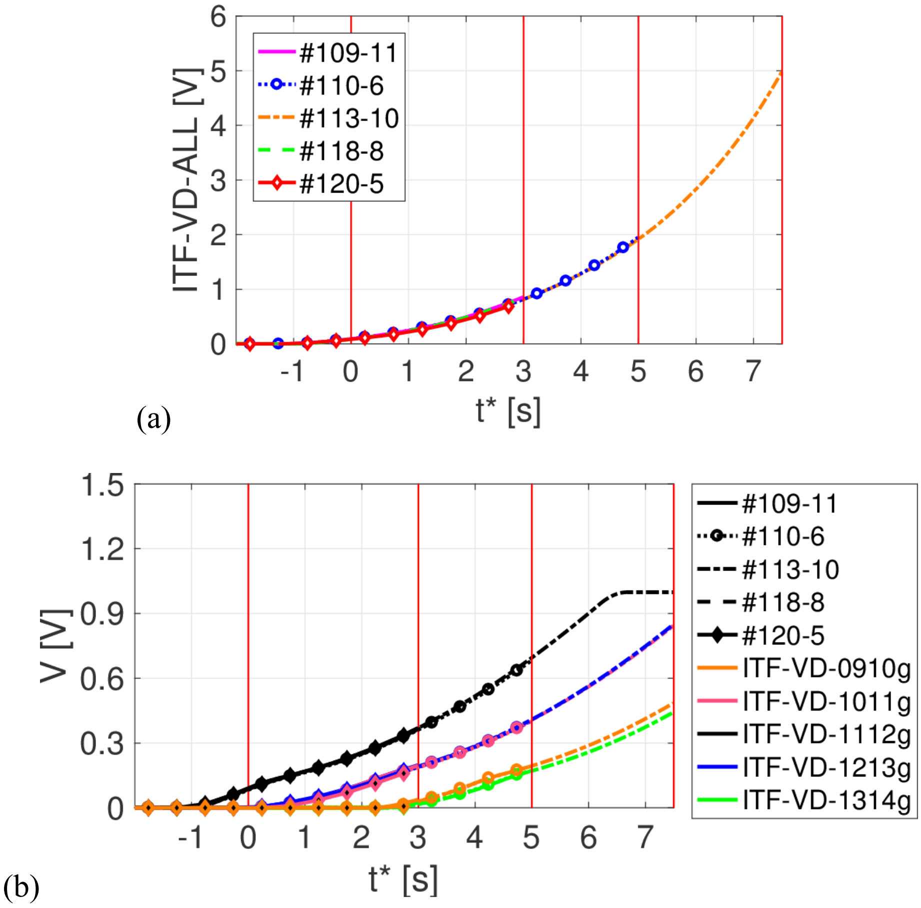

Figure 2.43. TFI test analysis: experimental evolution of (a) total and (b) local voltage evolutions during quench tests.

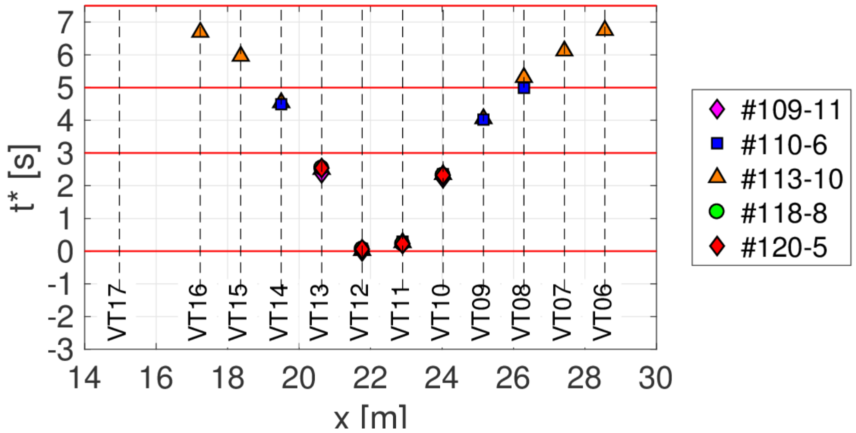

Figure 2.44. TFI test analysis: normal zone propagation as measured during quench tests.

Concerning the $T_{\text{hot-spot}}$, during the longest quench propagation the maximum virtual temperature reached by the conductor can be obtained only by extrapolation, see Figure 2.45. This is due to the local voltage sensor ITF−VD−1112g saturation for $t^* > \sim 6.5$ s. On the other side, local jacket temperature sensors show a not perfect reproducibility during the different tests, with differences up to 3.5 K, see Figure 2.46, with TS03 sensor trace not running parallel to the others, growing much more slowly. This odd behaviour may be due to an additional thermal contact resistance, e.g. in the glue used to attach the sensor on the jacket, see Paragraph 2.6.1.

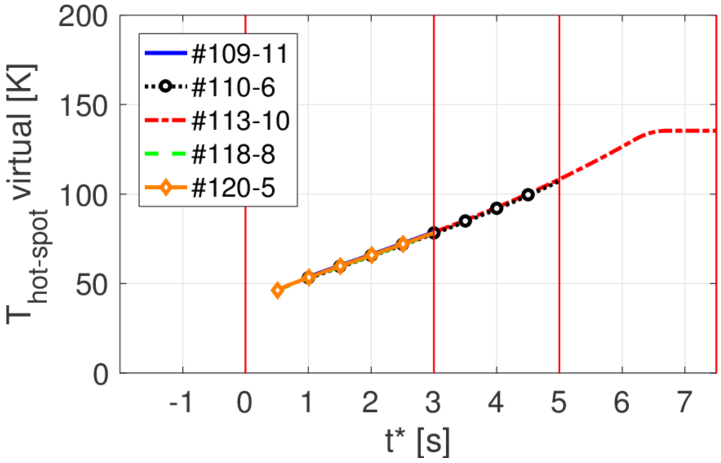

Figure 2.45. TFI test analysis: estimation of virtual hot-spot temperature during the quench tests on the TFI.

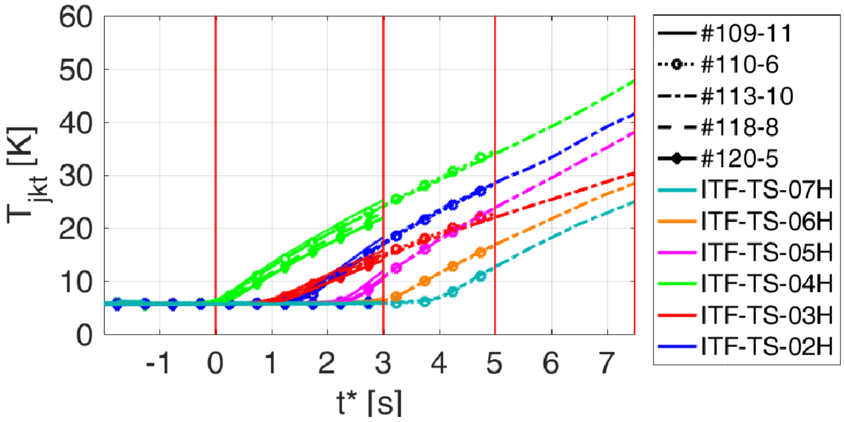

Figure 2.46. TFI test analysis: jacket temperature evolution at local sensors locations on the TFI during the quench tests.

As well as other features, also the hydraulic behaviour of the quench is reproducible: the pressurization shows basically the same evolution during all the tests performed, see Figure 2.47. The maximum inlet over-pressure is ~1.5 bar reached in the case of the test with the longest delay time, however the peak pressure is reached inside the TFI in the normal zone, but unfortunately, it cannot be directly measured. The mass flow rate behaviour is independent from the quench initiation energy only after the QD, see Figure 2.47, while during the initiation phase, from $t^* = -1.5$ s to $t^* = -0.5$ s, some differences are visible among the various tests.

Looking more in detail, at about $t^* = -1$ s, the pressure at the boundaries rapidly increases because of the normal zone initiated in the conductor centre and the Joule heat generation therein. On the sound propagation time-scale (~0.1 s), He is ejected from the coil boundaries, see Figure 2.48, driven by the pressure difference between the quenched zone and the coil boundaries.

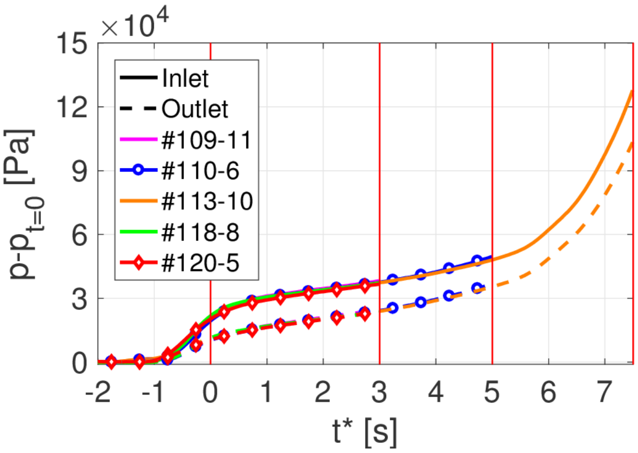

Figure 2.47. TFI test analysis: evolution of the pressurization at the inlet (solid line) and outlet (dashed line) of the TFI during quench tests.

From $t^* = 0$ s to $t^* = 1$ s, due to the pressure increase at the boundaries and the following He expulsion, the pressurization rate decreases, before increasing again after t^* ~5 s, as noted in [37], possibly because of the quench front acceleration. The measurements do not show any other increase of He expulsion rate because the mass flow rate signals saturate for $t^* > 3$ s. and being the flow sensors of orifice type, only data from zero to around 30 g/s, i.e. in the calibrated range, are considered reliable and therefore reported from now on.

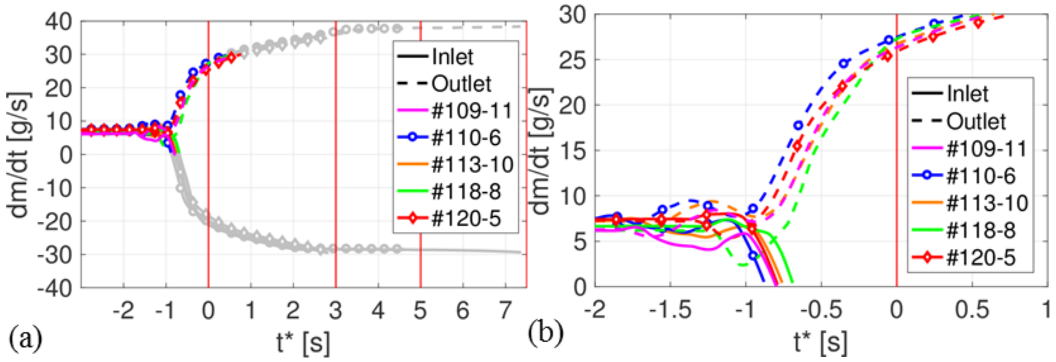

Figure 2.48. TFI test analysis: (a) mass flow rate evolution at the inlet (solid line) and outlet (dashed line) of the TFI during quench tests. Data outside the calibrated measurement range are reported with grey curves and will not be considered in successive discussions. (b) Zoom on the reliable measurement interval of mass flow rate.

In the particular case of shot #118-8, i.e. the only quench test initiated using two IHs, no major differences are observed with respect to all the other cases. In fact, using two IHs leads only to the deposition of more energy than the required minimum quench energy (MQE) without affecting the quench propagation.

Comparison between 4C code predictions and measurements

In view of the computational reproducibility of the quench phenomenon, the predicted results are compared, up to the current dump, only with shot #113-10, the one with the longest delay time, since it is the most interesting and severe from the quench propagation (and hot spot temperature) point of view. The curves are synchronized at t_{QD}, with $t_{QD,pred}$ ~1.71 s while $t_{QD,exp}$ ~1.64 s: this means that the computed results before the QD are not exactly capturing the experimental evolution. However, the initiation phase, before the QD, is strongly dependent on some parameters like the exact amount of energy deposited by the IH and its repartition between jacket and cable, whose detailed investigation is beyond the scope of this work.

The comparison of the predicted and measured total voltage across the coil shows an excellent agreement, see Figure 2.49; however, looking in detail on local voltage taps pairs, see Figure 2.50, the perfect agreement on total voltage results from the partial compensation of small inaccuracies in the simulation of the local measurements: take-offs of predicted evolutions are slightly in advance with respect to the experiment, but then the evolution is somewhat slower.

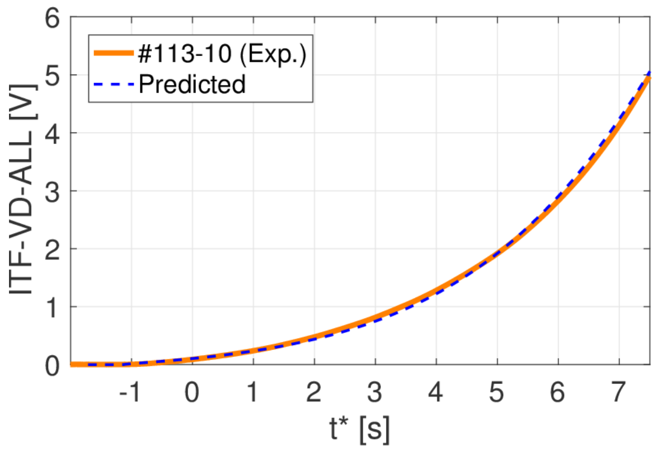

Figure 2.49. TFI test analysis: comparison between measured (solid orange) and predicted (dashed blue) total voltage evolution.

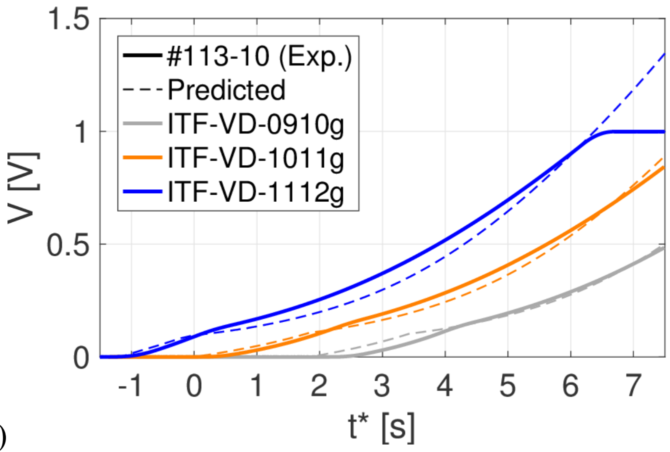

(a)

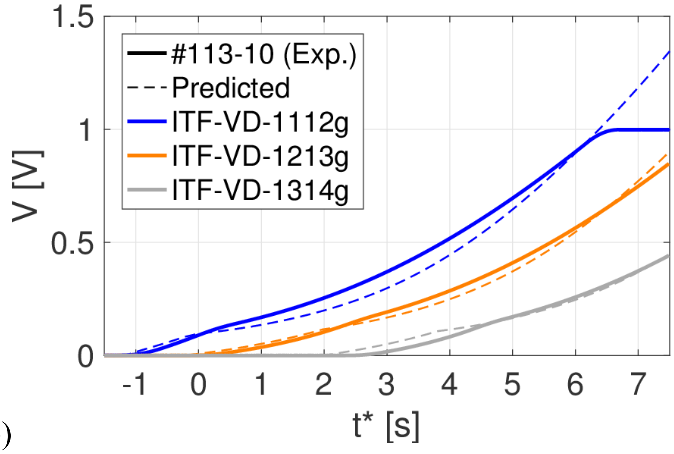

(b)

Figure 2.50. TFI test analysis: comparison between measured (solid) and predicted (dashed) local voltage signals (a) upstream and (b) downstream the quench initiation zone.

Comparing the quench propagation speed, an error below 15% is observed until $t^* < 5$ s, while in the last phase, the predictive simulation underestimates the quench front acceleration with speed mismatches up to 50%. It is worth remarking that, if compared to previous quench studies, e.g. [37] [76] [79], the normal zone evolution comparison shown here, see Figure 2.51a, can be considered very good; however, when looking in detail to the quench speed, see Figure 2.51b, such statement may be considered too enthusiastic.

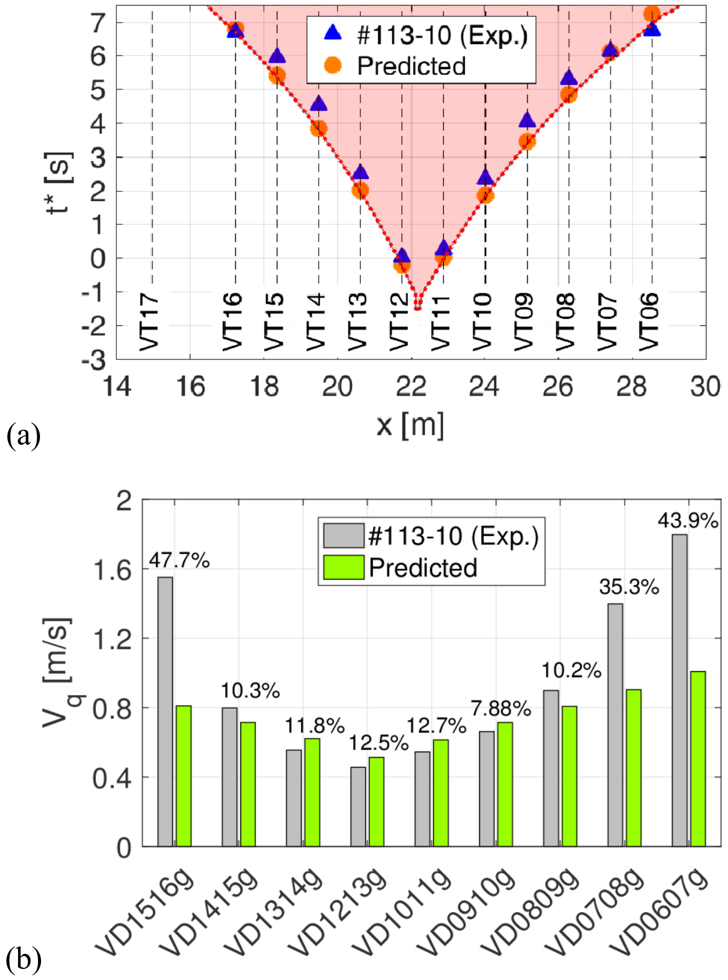

Figure 2.51. TFI test analysis: (a) comparison between measured (blue triangles) and predicted (orange circles) normal zone evolution. The $I = I_C$ curve is also reported (dotted red line). (b) Comparison between measured (grey bar) and predicted (green bar) quench propagation speed V_Q.

Concerning the temperatures, the predicted virtual $T_{\text{hot-spot}}$ is in good agreement with experimental results, see Figure 2.52, even if the computed result slightly overestimates its increase rate, namely: ~24 K/s against ~19 K/s of the experiment.

Moreover, since the difference between the predicted strands maximum temperature ($T_{\mathrm{strands}}^{\mathrm{max}}$) and the virtual $T_{\mathrm{hot\text{-}spot}}$ is <15 K, it is reasonable to assume that $T_{\mathrm{strands}}^{\mathrm{max}}$ will be 15 K higher than the extrapolated experimental virtual temperature (~155 K), resulting into an estimated value of ~170 K, well below the 250 K prescribed by the ITER design criteria [61].

Looking more in detail at the temperature evolutions, despite the very good agreement between measured and predicted $T_{\mathrm{hot\text{-}spot}}$ results, the computed jacket temperatures largely overestimate recorded data, with anticipated take-offs and higher increase rates, see Figure 2.53. Since the 4C code has already shown good capabilities in reproducing jacket temperature [37], this results were quite surprising. The reason behind this are possible uncertainty in the measurements due to the thermometers glued on the jacket external surface: being the amount and the thermal properties of the glue uncertain, some delays in response of the sensors may be induced. A similar disagreement has been found also in other analyses [84] performed with the Supermagnet code [85].

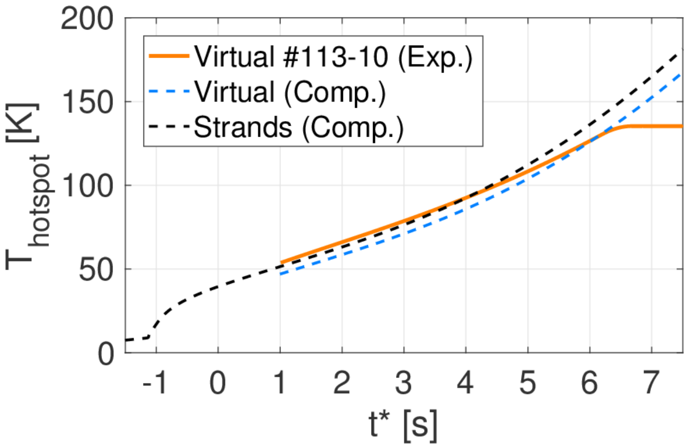

Figure 2.52. TFI test analysis: comparison between measured (thick solid orange) and predicted (dashed light blue) virtual $T_{\mathrm{hot\text{-}spot}}$. Predicted $T_{\mathrm{strands}}^{\mathrm{max}}$ is also reported (dashed black).

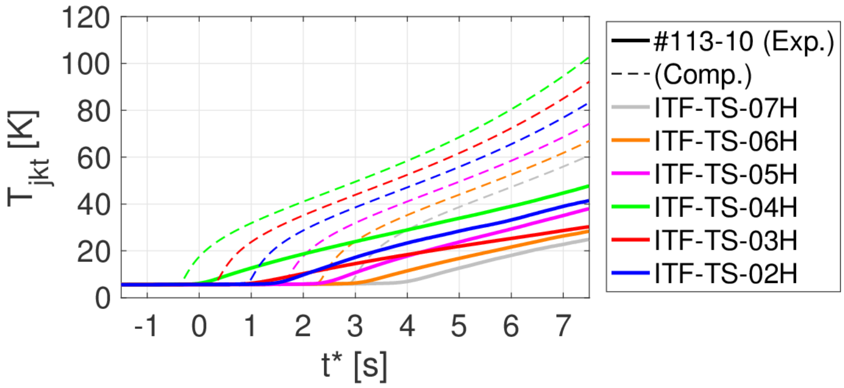

Figure 2.53. TFI test analysis: measured (thick solid) and predicted (thin dashed) jacket local temperature evolutions.

Concerning the mass flow rates, see Figure 2.54, the predicted evolution has two different phases as previously described. Before the QD, the predicted and experimental results are in complete disagreement: the predicted flow reverses at the inlet, while for the experiment it only slightly increases; at the outlet the opposite is observed. This odd (measured) behaviour already observed in [37] remains unexplained. During the second phase, the prediction overestimates the He expansion at the outlet. This difference is due to the fact that in reality, ejected He pressurizes the outlet manifold (not included in the model since fixed pressure is used as BCs) at the coil boundaries, reducing the pressure difference between the quenched zone and the boundaries.

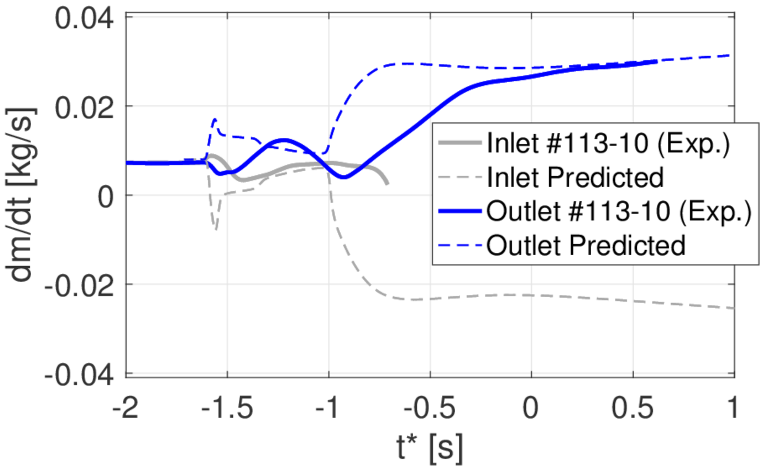

Figure 2.54. TFI test analysis: comparison between experimental (solid line) and predicted (dashed line) mass flow rate at the inlet (grey) and outlet (blue) of the TFI.

Interpretive simulations of the TFI quench

In order to improve the quality of the model and try to address some issues observed in the predictive exercise, some interpretive simulations have been performed after the tests.

Including the structures in the model

The first interpretive simulation performed includes the model of the supporting structure, trying to see if the experimental measurements of jacket temperature are, at least, bracketed by the computed temperature evolution on the jacket and the structures. Based on previous experience in simulating similar transients [86] and geometries [34], the model of the SS mandrel has been discretized in eight poloidal 2D cuts, on which a finite element model is used to solve the heat conduction problem, see Figure 2.55. The meshes for the cuts have from 6500 to 22000 elements depending on the particular cut considered.

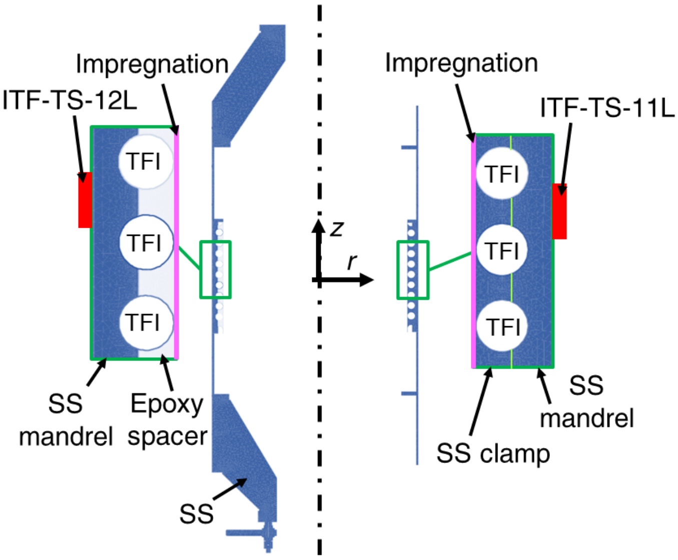

Figure 2.55. TFI test analysis: sketch of the TFI structure as implemented in the 4C model.

As expected, the computed structure and jacket temperatures bracket the measurements, see Figure 2.56, confirming the supposed measurements issues affecting the jacket temperature sensors. In fact, supporting this statement, the two additional temperature monitors included in the model, see Figure 2.55, allow to compare computed and experimental evolutions for sensors ITF−TS−11L and ITF−TS−12L, attached on the external surface of the mandrel at the height of the 5th TFI turn. The agreement between simulated and measured temperature evolutions is only qualitative, see Figure 2.57, possibly as a consequence of the adoption of a finite number of cuts. In fact, even if in the model the virtual sensors are located at the same (*r*, *z*) coordinate of the real sensors, they are associated with the temperature on a toroidal segment of the mandrel, while the sensor measures the temperature at a precise toroidal coordinate. Nevertheless, if the average temperature evolution is compared, the agreement is very good, proving the reliability of the structure model.

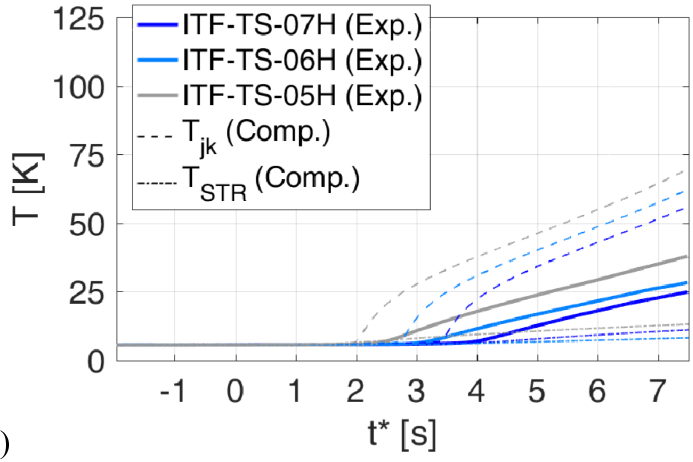

(a)

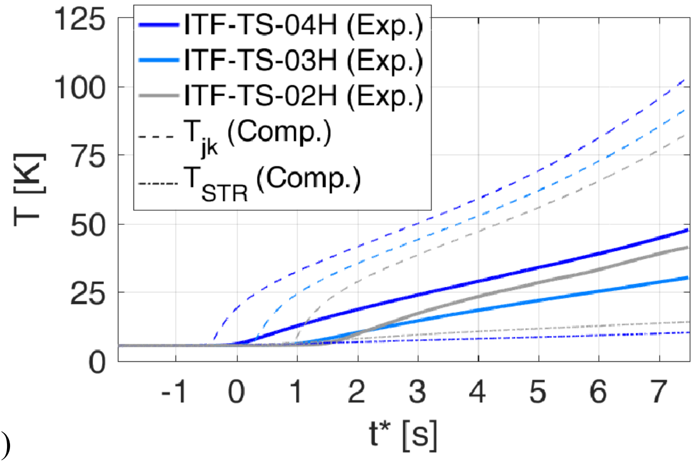

(b)

Figure 2.56. TFI test analysis: comparison between experimental (solid line) and computed (dashed line) temperatures on the jacket and on the structures (dash-dotted) during the quench test (a) upstream and (b) downstream the IH.

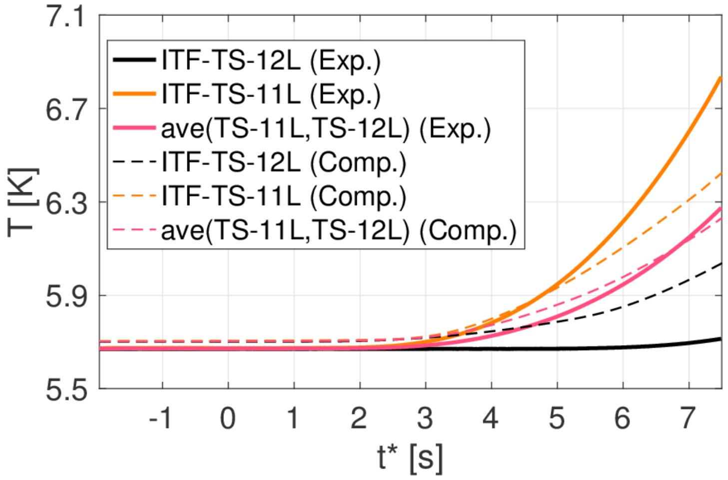

Figure 2.57. TFI test analysis: comparison between experimental (solid line) and computed (dashed line) temperature measured by the mandrel sensors ITF−TF−12L (black), ITF−TF−11L (orange) and their average (pink).

Including a different treatment of the boundary conditions

The second kind of interpretive simulations performed adopts two different recipes for the BCs treatment:

(i) Inclusion of an external cryogenic circuit to bypass the use of experimental BCs [87]. This is done to compare the p_{in}, p_{out} and T_{in} evolutions using a simplified model of the cryogenic loop, see Figure 2.58, including the TFI piping, the bus bars (BBs) and two pipes equivalent (in terms of transit time and hydraulic impedance) to the CSMC inner (CSIM) and outer (CSOM) modules, as already done in [37].

(ii) Prescribe the measured value of p_{in}, p_{out} and T_{in} as BCs.

If recipe (i) is adopted, the agreement between computed and measured results is only qualitative for $t^* < 5$ s, see Figure 2.59: the simulated pressurization is anticipated, with respect to the experiment, turning into an anticipated He expulsion, see Figure 2.60. When $t^* > 5$ s, the accelerated pressurization at the coil boundaries is not well captured. However, even if recipe (ii) is used, mass flow rates are not better captured, see again Figure 2.60. The lessons learnt from this analysis are that a different model is necessary to capture the initial phases of the quench propagation, which is indeed beyond the scope of this work, and that the acceleration of the pressurization is not related to the cryogenic circuit behaviour, but by some phenomena in the coil not captured by the model.

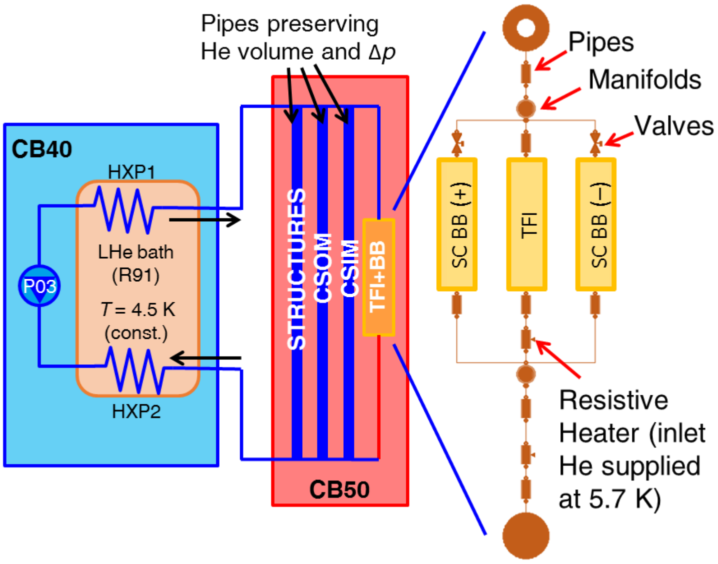

Figure 2.58. TFI test analysis: sketch of the cryogenic circuit used for the TFI quench simulation (HX = heat exchanger, CB40 = cold box, P03 = cold circulator).

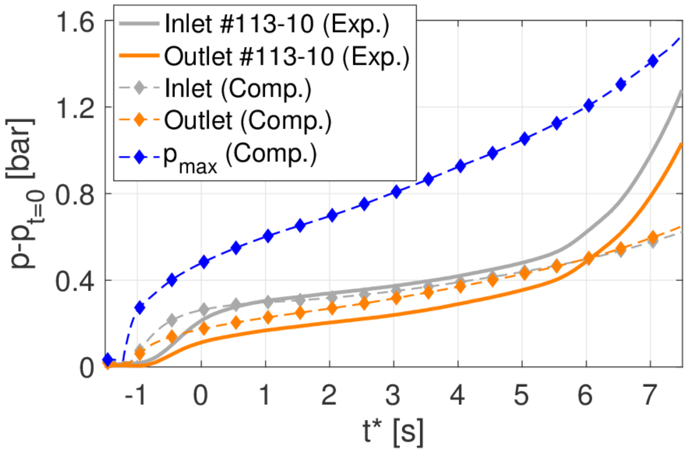

Figure 2.59. TFI test analysis: comparison between experimental (solid line) and computed (dashed line) pressurization at the coil boundaries (inlet: grey, outlet: orange) during the quench tests. Computed maximum pressure in the coil is also reported (dashed blue with diamonds).

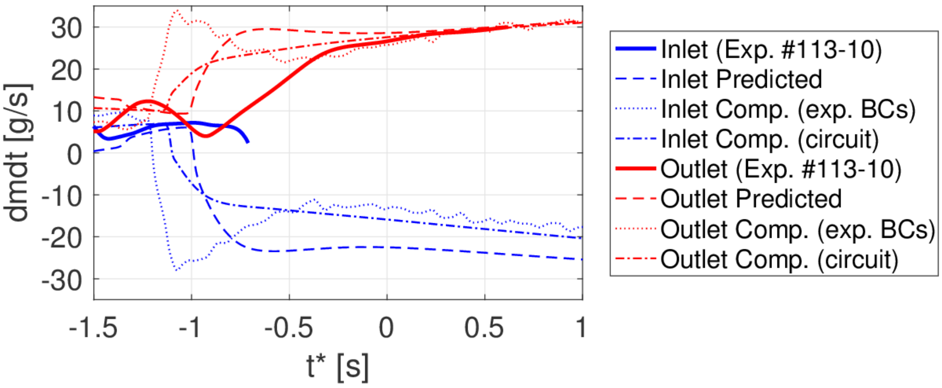

Figure 2.60. TFI test analysis: comparison of experimental (thick solid line), predicted (thin dashed line), computed with experimental BCs (thin dotted) and computed with circuit (thin dash-dotted) mass flow rate evolution at the inlet (blue) and outlet (red) of the TFI during the quench test.

Parametric study of the effects of inter-turn heat transfer

The last series of interpretive simulations performed try to address the discrepancy between the computed and experimental quench propagation speed and its acceleration for $t^* > 5$ s. It is interesting to note that ~5 s are the time required for the quench to propagate along the entire turn length and reach again the azimuthal coordinate of the IH. Moreover, since it is well known that the He preheating ahead of the quench front accelerates its propagation, see Figure 2.40a, it was supposed that the inter-turn thermal coupling is tighter than expected. Therefore, in the simulations performed, it is presumed that the central turn (where the IH is located) is thermally coupled with the two neighbouring ones through the turn insulation (neglecting the SS material); the contact perimeter along the three central turns has been assumed to be equal to its maximum value. However, since this would give the maximum heat transfer on the three turns, a multiplying coefficient M_λ, going from 0 to 1, is used to scale the HTC through the $2\times\delta_{\text{ins}}$ insulation thickness, thus computed as:

$$HTC_{IT} = M_\lambda \times \frac{\lambda_{ins}}{2\delta_{ins}} \tag{36}$$

where λ_{ins} and $\delta_{\text{ins}} = 1.4$ mm are the insulation thermal conductivity and thickness, respectively.

Simulation results show that with two proper values of M_λ it is possible to bracket the measured quench speed, see Figure 2.61, and that also the accelerated pressurization for $t^* > 5$ s is qualitatively better reproduced, see Figure 2.62.

The lesson learnt from this analysis is that, if the hypothesis on the higher effectiveness of the inter-turn coupling is correct, this can explain the acceleration of the quench propagation. For magnets with a design in which this phenomenon can occur, it may have an impact on the development of the quench detection system.

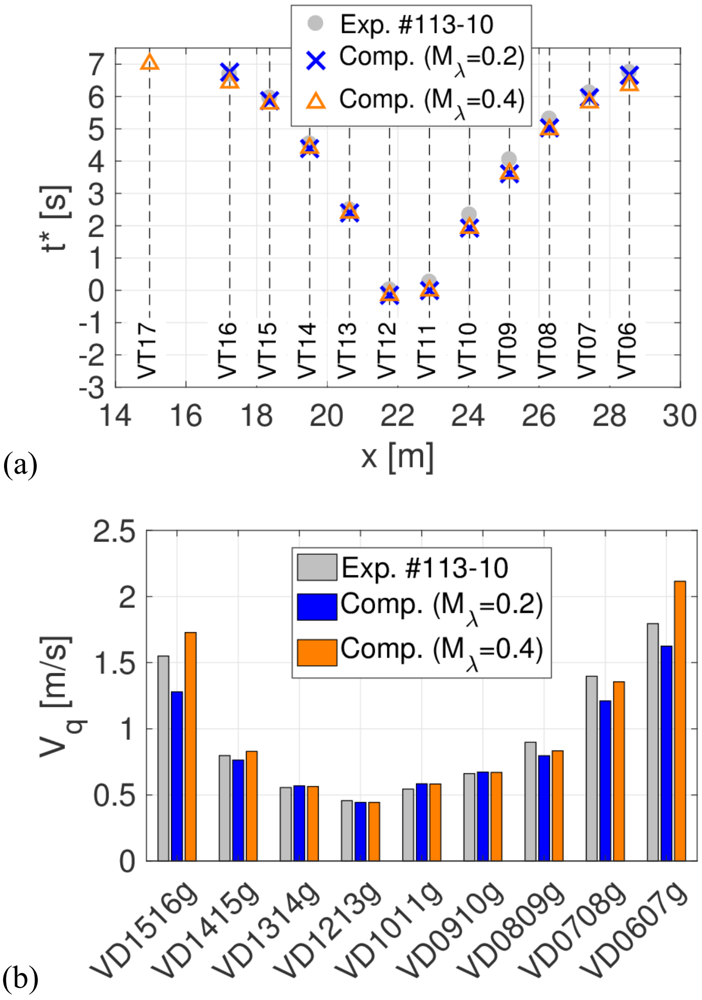

Figure 2.61. TFI test analysis: comparison of (a) normal zone propagation and (b) quench propagation speed as measured (grey) and computed with two different inter-turn M_λ multipliers (blue and orange, respectively).

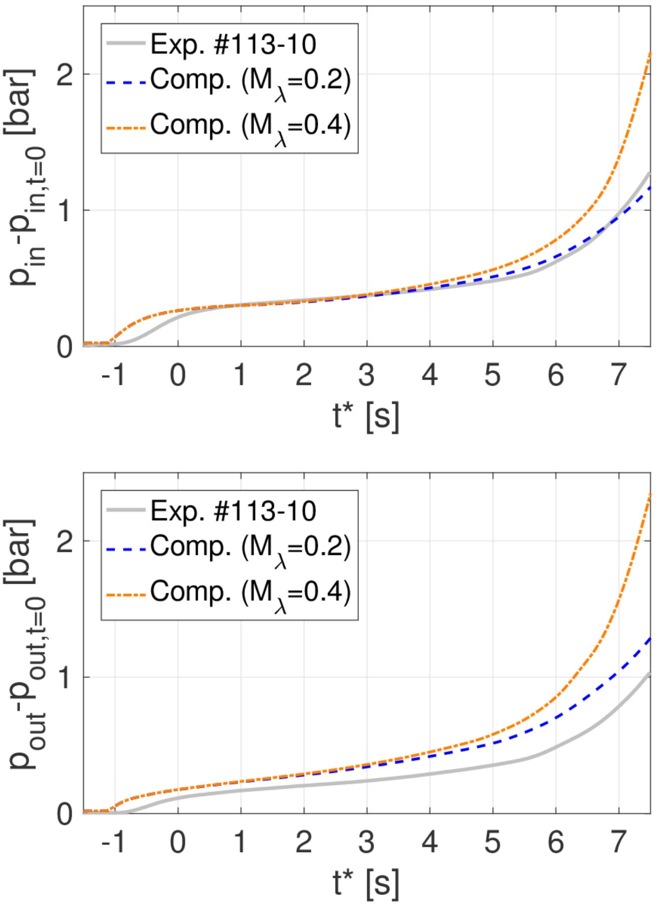

Figure 2.62. TFI test analysis: comparison of (a) inlet and (b) outlet pressurization between measured (thick grey) and computed using two different M_λ multipliers (dotted blue and dash-dotted orange, respectively).

Final considerations

All simulations, predictive and interpretive, have been performed with the 4C code and it must be remarked that the predictive simulation have been performed rigorously before the test and for the first time for a quench in ITER-relevant conditions, to the best of the author’s knowledge. The predicted results showed a good-to-excellent agreement with the experimental data for most of the relevant quantities; however some discrepancies were found and tried to be solved by means of interpretive simulations, which also aimed at improving the model quality.

A summary of the model ability to reproduce single and detailed features of the quench phenomenon is reported in Table 2.8 and Table 2.9 comparing the present work to previous ITER-relevant quench propagation assessments on Nb_3Sn coils.

Table 2.8. Qualitative evaluation of the agreement between ITER-relevant Nb_3Sn quench simulations and experiments: voltages and temperatures.

Reference	Prediction	$V_{tot}(t^*)$	$V_{loc}(t^*)$	$T_{hot\text{-}spot}(t^*)$	$T_{jkt}(t^*)$
Present work	☺	☺	☺😐	☺😐	☹ ?
[37]	n.a.	☺😐	☺😐	☺😐	☺
[79]	n.a.	☺😐	n.a.	☺	n.a.
[78]	n.a.	☺😐	n.a.	☺😐	n.a.
[77]	n.a.	😐	n.a.	n.a.	n.a.
[76]	n.a.	☺😐	n.a.	☺	☺
[75]	n.a.	☺😐	n.a.	n.a.	n.a.

Note: multiple faces = agreement between the two, or either of the two, corresponding faces; ? = possible uncertainties in experimental data; n.a. = not applicable.

Table 2.9. Qualitative evaluation of the agreement between ITER-relevant Nb_3Sn quench simulations and experiments: quench speed and hydraulics.

Reference	V_q ($t^* < 5$ s)	V_q ($t^* > 5$ s)	dm/dt (t^*)	p (t^*)
Present work	☺😐	☺😐	😐 ?	☺😐
[37]	😐	😐	☺ ?	😐☹
[79]	☹	☺☹	n.a.	n.a.
[78]	☹	☺☹	n.a.	n.a.
[77]	n.a.	n.a.	n.a.	n.a.
[76]	☹	😐☹	☺	☹
[75]	☺😐	☺😐	n.a.	☺😐

Note: multiple faces = agreement between the two, or either of the two, corresponding faces; ? = possible uncertainties in experimental data; n.a. = not applicable.

Chapter 3

Performance analysis of the ITER CS

3.1. The ITER CS

The ITER CS is constituted by six separate modules built by electrically jointing, on the outer side of the coil, six hexa-pancakes (HP) and a single quad-pancake (QP) each with 14 turns, see Figure 3.1, for a total of 40 pancakes. These seven circle-in-square Nb_3Sn CICCs (jacket side = 48.8 mm) are then used for the winding of each module (height = ~2.2 m, inner radius = ~1.3 m, outer radius = ~2.1 m), cooled by SHe supplied by a cryogenic circuit.

The modules of the ITER CS coil are currently being tested in a new General Atomics (GA) facility in San Diego (California, US). The strands have been manufactured by different producers (JASTEC, Furukawa and KAT) [16] and, finally, the conductor used to wind all the six modules of the ITER CS coil has undergone a long series of qualification tests including a series of short samples tested in the SULTAN facility (Villigen, Switzerland) [88], to qualify different cable suppliers and assess the effects of different design parameters (e.g. strands twist pitch), and lastly the full-scale sample (the CSI) tested in 2015 in the bore-hole of the CSMC at QST (Naka, Japan).

Here, the simulation of the 15 MA plasma scenario for the ITER CS is performed, see Figure 3.2, considering all the six modules with the inputs and assumptions obtained from the design process and the experience gained during qualification tests, see e.g. Paragraph 2.5.

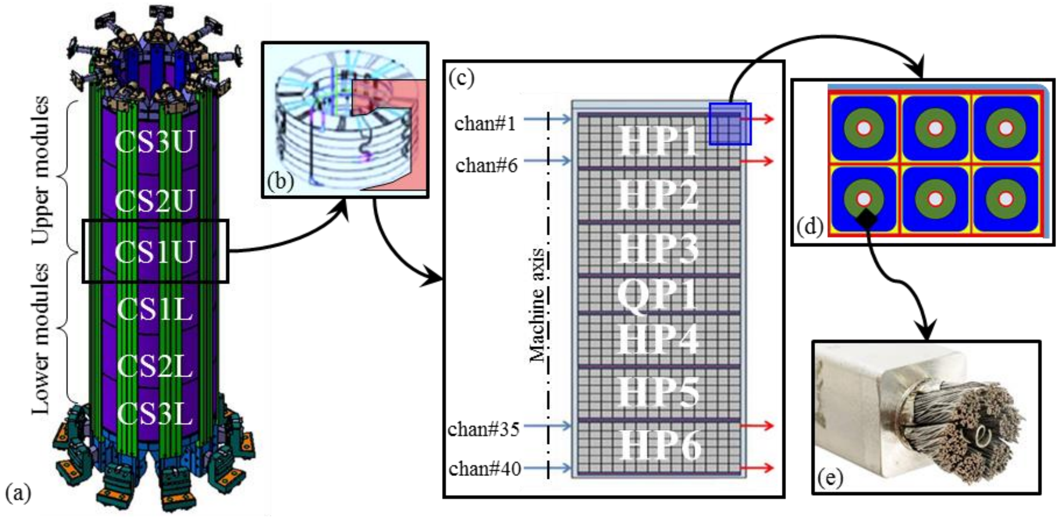

Figure 3.1. (a) Representation of the ITER CS coil (adapted from [89]). (b) A single ITER CS module with (c) its cross section, (d) a zoom showing the insulation layer between adjacent turns and (e) a picture of the real ITER CS conductor [25].

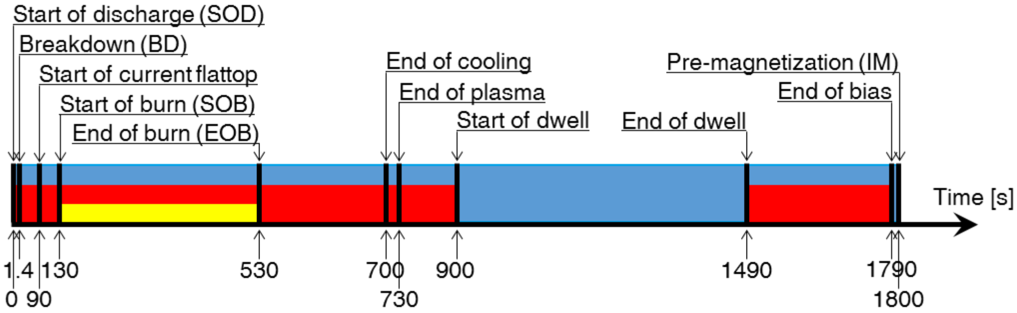

Figure 3.2. ITER CS coil analysis: timeline of the ITER standard 15 MA plasma pulse used in the simulation.

3.2. Simulation setup

3.2.1. Geometry, scaling parameters and friction factor correlations

The 4C model of the CS coil includes 40 parallel channels per each module (240 channels in total) modeled with the same hydraulic length. This is an ideal approximation as the length of the pancakes may differ up to ~10 m. The cryogenic circuit and all the modules, with He flowing in counter-current in each pancake, are simulated at the same time. The model accounts also for the inter-pancake (adjacent channels) and inter-turn (same channel) thermal coupling inside the module: a series of thermal resistances, accounting for the multi-layer insulation scheme adopted in the winding, is used to compute the heat transfer.

The conductor used is the same of the CSI, whose geometrical and scaling parameters are reported in Table 2.1 and Table 2.5, respectively, while the adopted friction factor correlations are defined in Paragraph 2.5.1.

3.2.2. Circuit model

All the six modules of the CS coil are cooled in parallel by forced flow SHe circulating in a dedicated cooling circuit, see Figure 3.3. He inlets are located at the inner side of the coil, while outlets are placed at the outer radius. The first level of circuit parallel is constituted by the three upper modules (U) and the three lower (L) ones, fed by two different cooling branches with slightly different lengths and their own manifolds. The second level of parallel flow is constituted by the two feeders of each module-triplet, which are connected to a manifold coupled to the circulator. From the circulator, He passes through a HX releasing the heat to a LHe bath kept at 4.3 K before being sent back to the coil using the same two-level parallel flow scheme adopted for the outlet. The main hydraulic parameters of the cooling circuit, taken from [68], are reported in Table 3.1.

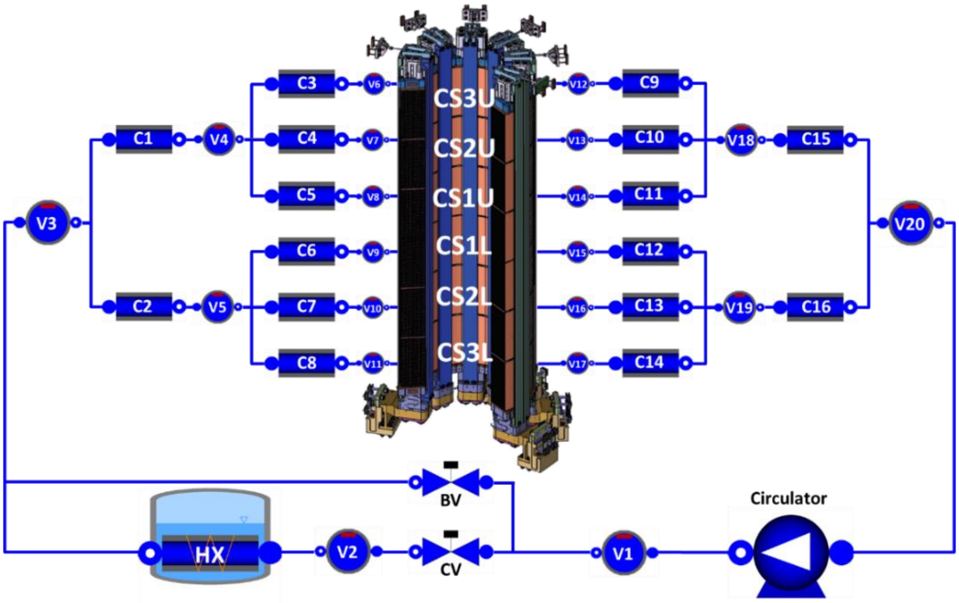

Figure 3.3. ITER CS coil analysis: model of ITER CS coil cooling circuit adopted in the simulations showing the CS modules (CS##), volumes (V#), cryolines (C##), heat exchanger (HX), control valve (CV) and the bypass valve (BV).

Table 3.1. Parameter of circuit components: length and internal diameter for the cryolines and volumes for the manifolds from [68].

Cryoline #	Length [m]	ID [mm]	Manifold #	Volume [m^3]
C1	40	85	V1	0.24
C2	96	85	V2	0.24
C3−C14	54	53	V3	0.24
C15	40	85	V4−V5	0.164
C16	96	85	V6−V17	0.4

3.2.3. Operating scenario

In the simulations, the standard 15 MA plasma scenario is considered, see Figure 3.2. The magnetic field [90] on the centerline of the conductor, being it pancake wound, has a different (but constant) value on each turn, see for instance Figure 3.4. The magnetic field is assumed to vary linearly on the conductor cross section and the maximum magnetic field is computed as:

$$B_{max} = (1 + \alpha) \cdot B_{ave} \tag{37}$$

where the coefficient α obtained as:

$$\alpha = \frac{1}{B_{ave}} \cdot \frac{\Delta B}{2} \tag{38}$$

being B_{ave} the magnetic field on the centreline and ΔB the magnetic field difference on the conductor cross section, available from [91]. The magnetic field profiles have been stretched or compressed to comply with the assumption of equal turn (10.748 m) for all the turns of all the pancakes.

The current in the different modules follows the prescribed evolution [88], see Figure 3.5: its variations change the value of the magnetic field, see Figure 3.6, and therefore induce AC losses in the conductors. As an outcome of the analysis performed in [36], both coupling (P_{coup}) and hysteresis (P_{hyst}) losses are accounted for in the model according to (14) and (18), respectively.

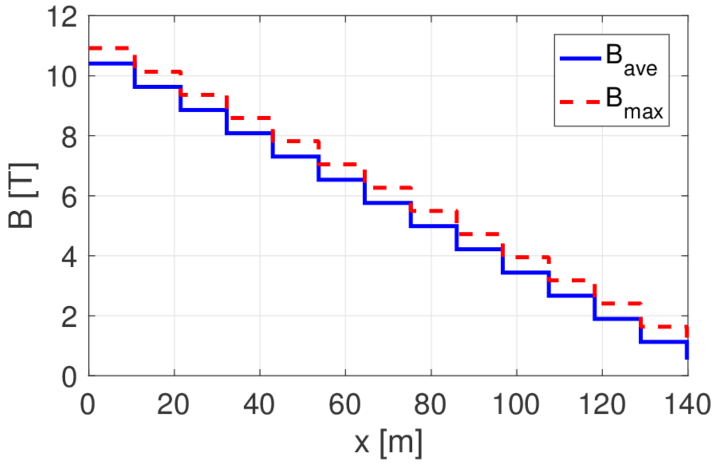

Figure 3.4. ITER CS coil analysis: average (solid blue) and maximum (dashed red) magnetic field profile at the end of the breakdown (BD) in conductor #20 of the CS2U module.

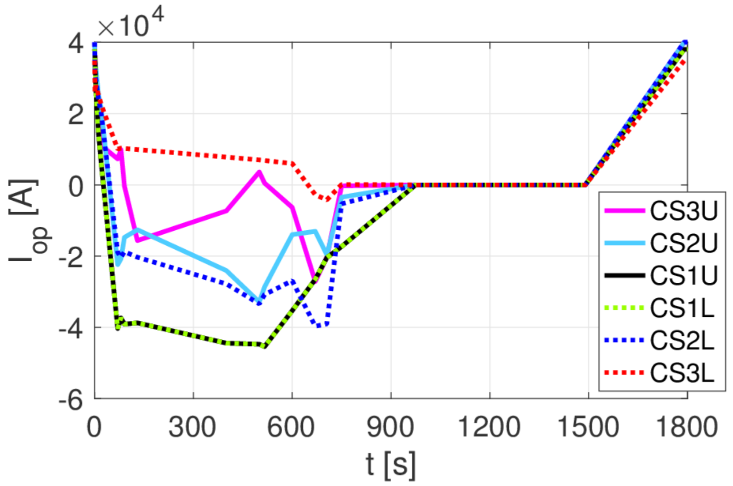

Figure 3.5. ITER CS coil analysis: prescribed current evolution during the 15 MA plasma scenario in each module of the ITER CS coil.

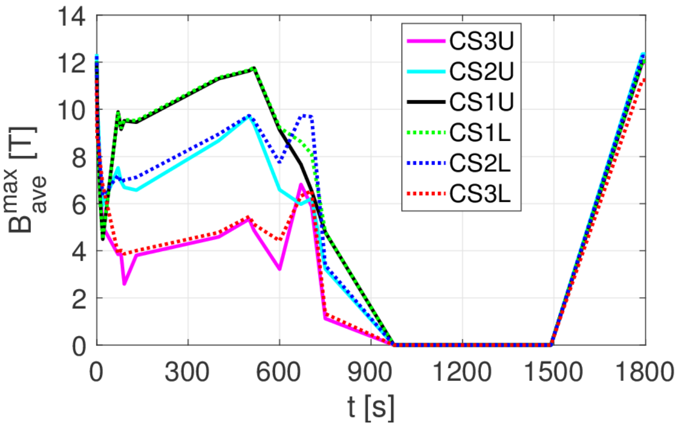

Figure 3.6. ITER CS coil analysis: maximum global magnetic field on the centerline of each module of the ITER CS coil.

Besides the AC losses, other heat loads affect the CS operation: the Joule losses in the joints, the static heat load on the cryogenic circuit and the circulator work, while the nuclear and static (radiative and conductive) heat loads on the bare coil are negligible. The values of the heat loads are reported in Table 3.2: for simulations with virgin (first start-up, $n\tau = 580$ ms) and cycled (after EM cycles, $n\tau = 220$ ms) conductors [36]. By using the analytic AC loss formulation, the total power deposition, see Figure 3.7, will be different from what has been used in [68], where it was an external input to the code and not computed in runtime as done here.

Table 3.2. Heat loads on the entire CS coil during ITER standard 15 MA plasma pulse.

Item	**From** [68]		**Virgin conductors**		**Cycled conductors**	
	Energy [MJ/cycle]	**[%]**	**Energy [MJ/cycle]**	**[%]**	**Energy [MJ/cycle]**	**[%]**
AC losses	8.14	56	13.39	65.22	6.727	48.34
Joint losses	0.058	0.5	0.058	0.282	0.058	0.417
Static heat load on circuit	2.572	17.5	2.572	12.53	2.572	18.48
Circulator work	3.8	26	4.51	21.97	4.56	32.77
Total	14.6	100	20.53	100	13.91	100

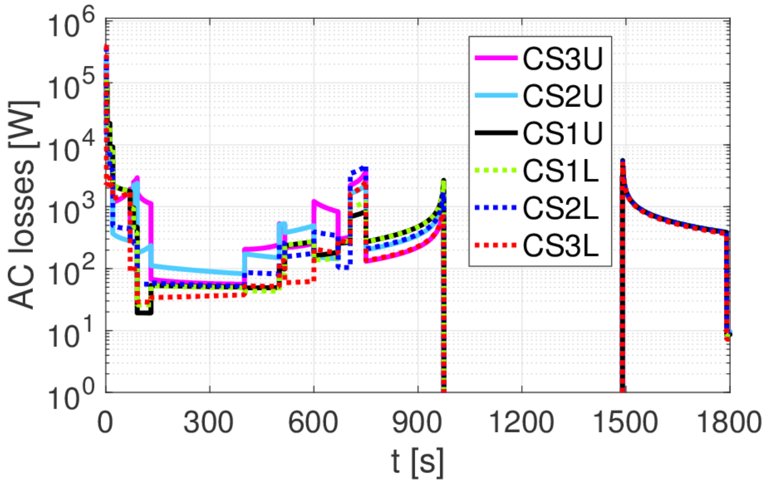

Figure 3.7. ITER CS coil analysis: total AC loss power deposition during the 15 MA plasma scenario in each module of the ITER CS coil with cycled conductors.

3.2.4. Numerics

Concerning the numerical aspects of the analysis, with no data available in literature, a dedicated grid independence and time convergence analysis, see Figure 3.8, has been carried out on the ITER CS coil model. The chosen reference value for the analysis is the minimum temperature margin ($\Delta T_{\mathrm{marg}}^{\mathrm{min}}$) in value in the most critical conductor (see Paragraph 3.3.2). As outcome of the analysis, the values of the minimum/maximum mesh size ($dx = 0.004/ 0.8$ m) and time step

(dt = 0.01/0.1 s) has been chosen to provide a satisfactory trade-off between computational time and accuracy.

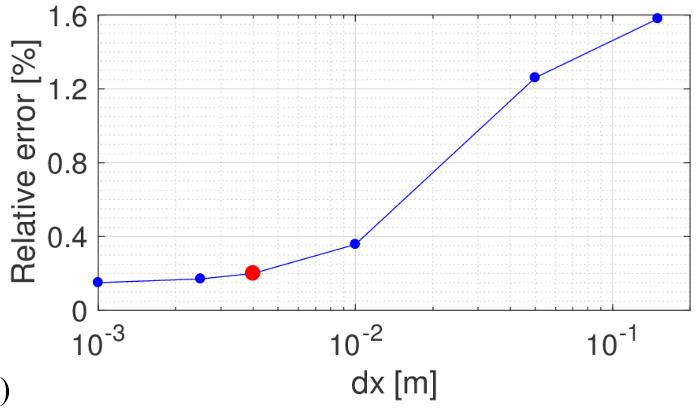

(a)

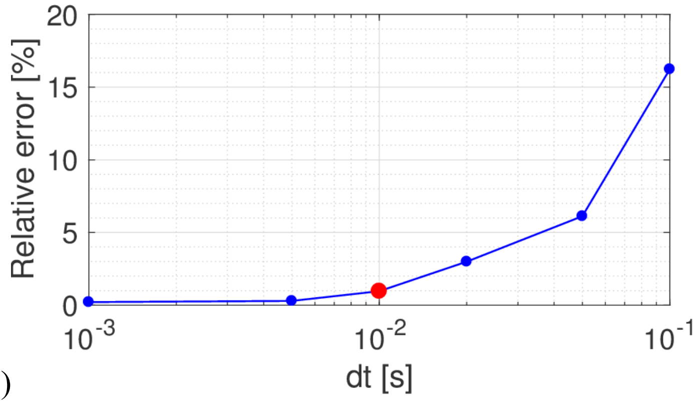

(b)

Figure 3.8. ITER CS coil analysis: (a) grid independence (dt = 0.01 s) and (b) time convergence (dx = 0.004 m) analysis for the ITER CS coil model. The selected values of dx and dt are highlighted by the red circle.

3.3. Results

After an initial stabilization phase, the 15 MA scenario has been simulated both with *virgin* and *cycled* conductors. Since coupling losses are proportional to the coupling time constant, the most severe conditions are expected for the plasma pulse with virgin conductors and the results are compared to those obtained in [68] (in figures referred to as “L. Savoldi, 2014a”) that differs from the present simulation in two main aspects: the AC losses, computed *a priori* and given as an input and therefore not computed on runtime as done in present simulation, thanks to the AC loss analysis carried in the framework of the CSI test analysis (see Paragraph 2.5.3) and the effective strain considered (see Paragraph 2.5.4).

3.3.1. Initial stabilization

At steady state the circulator supplies ~2 kg/s [90] (p_{in} ~4 bar, pressure head ~0.084 MPa,) to the CS, almost uniformly split between all the 240 conductors with an average value of ~8.4 g/s, see Figure 3.9. Lower modules have a slightly smaller mass flow rate (around −0.78% with respect to the overall average) because of the longer inlet cryoline C2 with respect to C1, see Table 3.1.

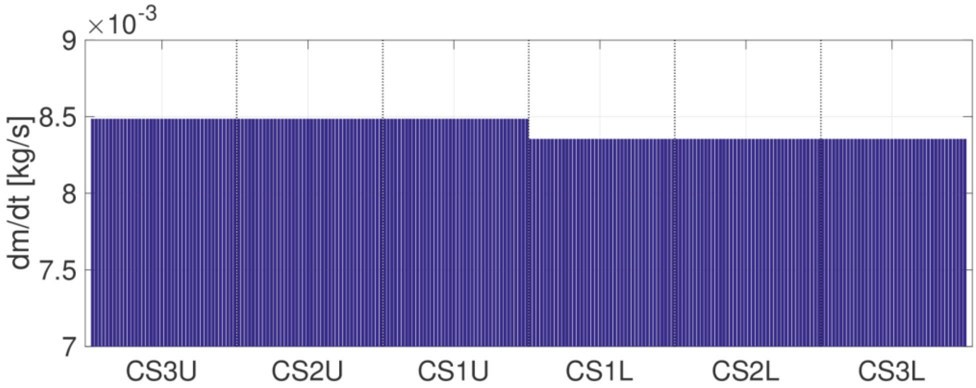

Figure 3.9. ITER CS coil analysis: steady state mass flow rate in each channel of the ITER CS coil.

3.3.2. Normal operation

Mass flow rates

During the large power deposition in the BD phase from 0 s to ~1.36 s, the pressurization in the peripheral modules induces a strong backflow, see Figure 3.10. On the other side, in the central modules CS1U and CS1L, since the power deposited is smaller, an increase in the inlet mass flow rate is observed, as consequence of the tight hydraulic parallel connection with the other modules. Then from ~1.36 s to ~5 s, the central modules experience the largest losses and the above-mentioned phenomenon is reversed. After 5 s, the pressurization inside the coil is not strong enough to maintain the backflow because of the losses reduction.

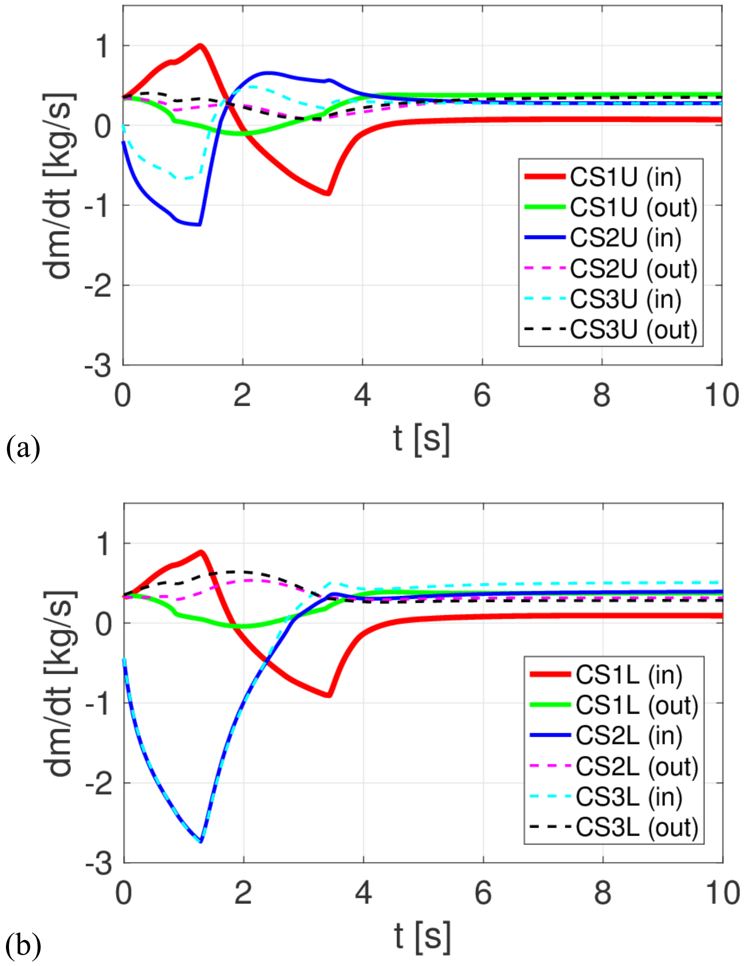

Figure 3.10. ITER CS coil analysis: mass flow rate evolution in (a) upper and (b) lower modules of the ITER CS coil during first 10 s of the standard 15 MA plasma pulse with cycled conductors.

Circuit

Pressures

In the first phase of the pulse, the power deposition causes a pressurization of the SHe loop which reaches a maximum value depending on the coupling time constant, see Figure 3.11. When the magnetic field derivative (and so the losses) are low, the pressurization in the circuit decreases, until the coil is charged again starting from ~1500 s. The small pressure increase at ~700 s is due to the sudden current change at the End of Plasma, see Figure 3.2 and Figure 3.5.

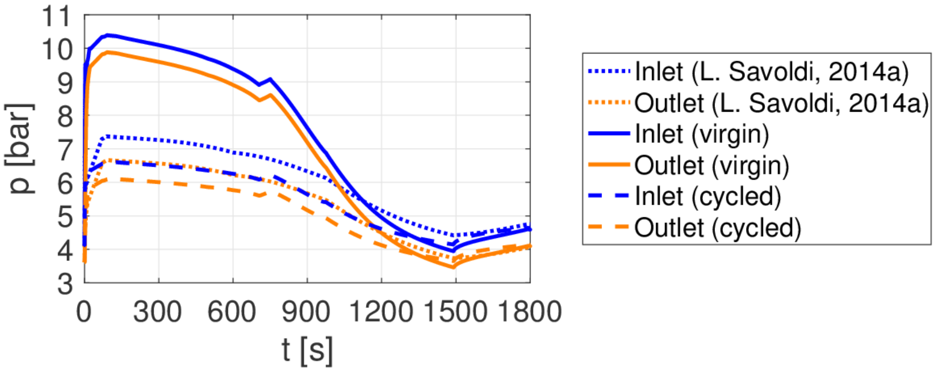

Figure 3.11. ITER CS coil analysis: pressure at inlet (blue) and outlet (orange) feeders of the CS coil from [68] (dotted line) and present simulation with virgin (solid line) and cycled (dashed line) conductor.

Heat Exchanger

During the plasma pulse, the energy deposited in the modules, summed to the static heat load on circuit components, must be dissipated to the LHe bath, see Figure 3.12. The HX removes the maximum power at ~900 s, corresponding to the time required by the power deposited during the first phase of the transient (~400 s) to be evacuated through the CS channels (~400 s) and then advected in the cryolines from the coil to the HX (~100 s). The reduction of the power exchanged in the first 4 s is due to the backflow during the initial phase: a reduction of the mass flow in the HX also reduces the heat exchange. The direct relation between the energy deposited and the power extracted by the HX is clear, with the highest and lowest peak observed for the pulse with virgin and cycled conductors respectively, while results from [68] are at an intermediate level.

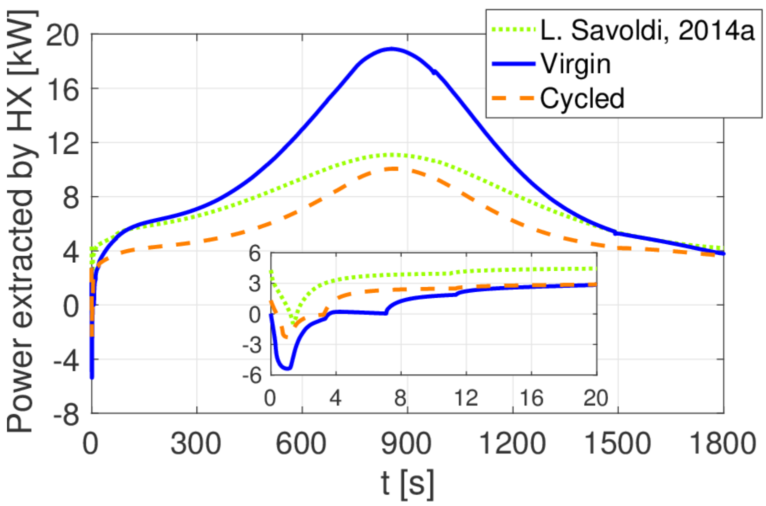

Figure 3.12. ITER CS coil analysis: power extracted by the HX in the CS cooling circuit during the ITER standard 15 MA plasma pulse from [68] (dotted green) and present simulations with virgin (solid blue) and cycled (dashed orange) conductors.

Minimum temperature margin

In the normal operation, the absolute $\Delta T_{\mathrm{marg}}^{\mathrm{min}}$ in the CS coil, see Figure 3.13, rapidly decreases during the BD, because the peak values within the whole transient of the magnetic field and its time derivative are expected to be here, see Figure 3.6. Then, $\Delta T_{\mathrm{marg}}^{\mathrm{min}}$ starts increasing because of the combined reduction of B and the decrease of dB/dt, turning into an increase of the T_{CS} and a decrease of the power deposited, respectively. This is true up to ~70 s when the field starts increasing again for a short time eroding the $\Delta T_{\mathrm{marg}}^{\mathrm{min}}$. Continuing in the transient, from ~100 s to ~900 s, the $\Delta T_{\mathrm{marg}}^{\mathrm{min}}$ increases because of the small power deposition in the coil and then, during the dwell when $t \in [900{,}1500]$ s, the margin remains almost constant, because the coil is not charged. Finally, after 1500 s (during the coil recharge), the margin decreases again as the magnetic field increases and thus the T_{CS} decreases. Results obtained in [68] show an overall evolution similar to the case with cycled conductors (the total energy deposited differs of only ~5% in the two cases), however, the $\Delta T_{\mathrm{marg}}^{\mathrm{min}}$ is lower because of the larger strain applied.

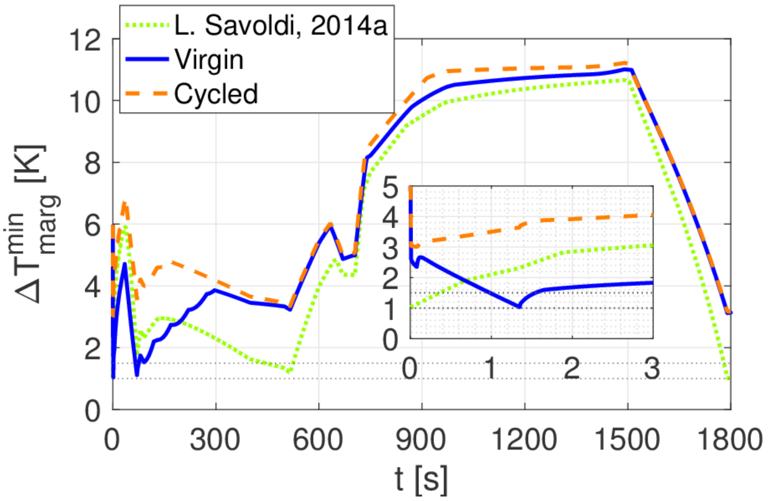

Figure 3.13. ITER CS coil analysis: absolute ΔT_{marg}^{min} in the entire CS coil from [68] (dotted green) and present simulations with virgin (solid blue) and cycled (dashed orange) conductors.

Looking more in detail, during the 15 MA plasma scenario, the requirement for ΔT_{marg}^{min} of 1.0 K [92] and 1.5 K [61] with virgin and cycled conductors, respectively, is satisfied. At the SOD, the conductors of the charged coil are in the same severe operating conditions (high current, magnetic field and strain) both at the beginning and at the end of the EM cycles, but the minimum margin for the two considered cases is reached at different times:

- with virgin conductors, the margin reaches its minimum value at the end of the BD, because starting from the charged coil, large AC losses are energy deposited in the conductors;
- with cycled conductor the ΔT_{marg}^{min} is reached at IM, with the coil charged in the most severe conditions (high current and magnetic field), because during the BD, the reduced AC losses (= relatively small increase of the operational T), combined with the fast magnetic field reduction (=fast increase of the T_{CS}), turn into an increase of the ΔT_{marg}^{min}.

Nevertheless, in both cases, the most critical conductor is located in CS2L module (virgin: pancake #27, cycled: pancake #19), see Figure 3.14. However, by including in the simulation the 10% uncertainty on the $n\tau$ [36], it turns out that, the ΔT_{marg}^{min} goes below the acceptance limit in some conductors. When compared to present results, the outcome of [68] shows the lowest ΔT_{marg}^{min} because, even if the energy deposited is comparable to that expected with cycled conductors, a higher strain on the pancakes was expected.

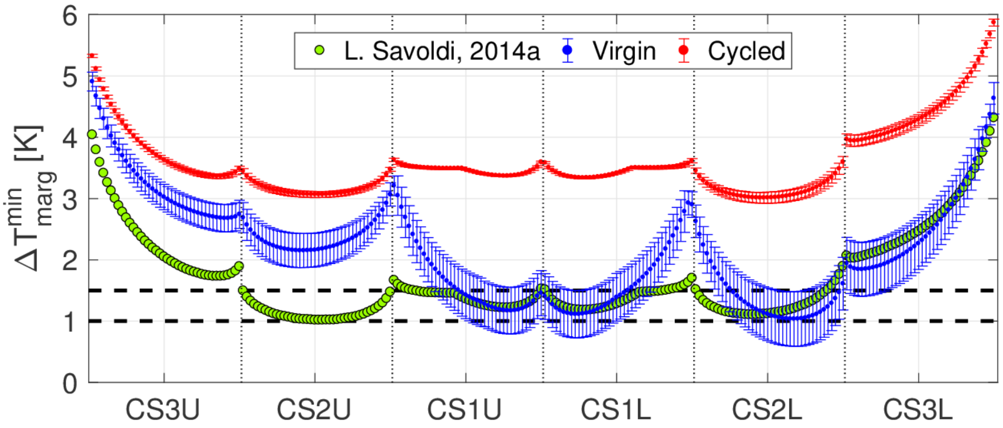

Figure 3.14. ITER CS coil analysis: $\Delta T_{\mathrm{marg}}^{\mathrm{min}}$ in all conductors of the CS coil from [68] (green circles) and present simulations with virgin (blue dots) and cycled (red dots) conductors. The estimated error bar for present simulations is also reported.

3.3.3. Off-normal operation

Here, the unprecedented simulation of off-normal operation is performed considering a ~25% reduction of the mass flow rate in the most critical pancake, for conservative reasons. This exercise aims at accounting for the uncertainty related to the friction factors and the effective hydraulic length of the channels, which may differ from the ideal value assumed in the model. Results for the simulation with reduced mass flow rate in the virgin pancake #27 show an additional $\Delta T_{\mathrm{marg}}^{\mathrm{min}}$ erosion of ~0.15 K, see Figure 3.15, with the lower bound of the error bar going significantly below the acceptance threshold. With reduced cooling capacity in pancake #27, thermally coupled adjacent pancakes must remove additional heat but they show a $\Delta T_{\mathrm{marg}}^{\mathrm{min}}$ reduction of only few mK.

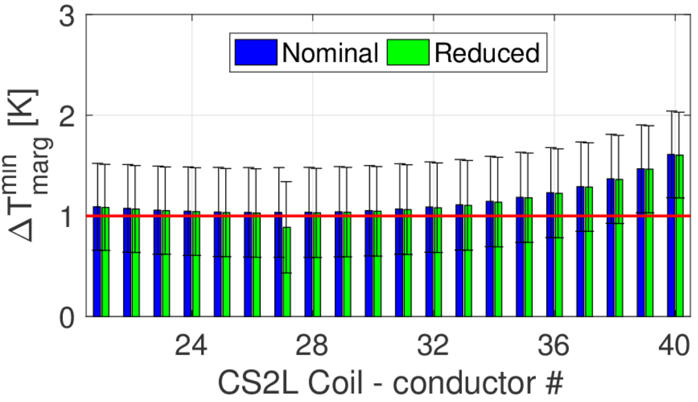

Figure 3.15. ITER CS coil analysis: ΔT_{marg}^{min} in CS2L module, with virgin conductors, considering the nominal (blue bars) and reduced (green bar) mass flow rate in the most critical pancake.

3.4. Conclusions

The thermal-hydraulic analysis of the ITER CS coil has been carried out, starting from the experience gained during the CSI test campaign carried out in 2015.

The simulation of the ITER CS operation showed better performances, in terms of ΔT_{marg}^{min}, with respect to previous analyses, mainly in view of the updated strain value. Computed results show that the requirement on ΔT_{marg}^{min} is nominally satisfied both with virgin (>1.0 K) and cycled (>1.5 K) conductors. However, in the first case, when the uncertainties on the coupling time constant are accounted for, some conductors in the CS2L module are below the acceptance threshold. On the other side, after EM cycles and power deposition almost halved, the ΔT_{marg}^{min} is almost unaffected by this uncertainty. The off-normal operation analysis considers a reduction of the mass flow of 25% in the most critical pancake, a reasonable guess in view of the assumptions made in the model (i.e. equal turn length). The simulation with virgin conductors shows that the ΔT_{marg}^{min} is eroded of additional ~0.15 K in the critical pancake, while the other ones are almost unaffected.

In conclusion, the first pulse of the CS, if at full current, may turn out to be the critical one from the point of view of the ΔT_{marg}^{min}, because of the large AC losses, while after several EM cycles, the ΔT_{marg}^{min} concern is more relaxed. Considering that some EM cycles will already be performed on all the CS modules during their final testing in the GA facility in San Diego, during ITER operation no issues are highlighted as far as the CS conductor ΔT_{marg}^{min} is concerned.

Chapter 4

Performance analysis of the ITER TF

4.1. The ITER TF coils

In the ITER machine there are 18 TF coils [93] which must provide a constant magnetic field of 5.3 T on the plasma toroidal axis, while the peak field on the coil reaches about 12 T and so Nb_3Sn CICCs are used (strands manufactured by several manufactures like BEAS, ChMP, Hitachi, JASTEC and others, see [16]). The conductors are wound in double pancakes (DPs), see Figure 4.1, enclosed in stainless steel radial plates (RPs). A set of seven DPs constitutes the WP of the TF, which is then inserted in a large SS case refrigerated by 74 dedicated case cooling channels (CCCs).

Starting from 2018 [94] [95], the last stages of manufacturing are taking place, with the winding-pack insertion in the case sub-assemblies [96], before shipment to the ITER construction site.

Here, taking advantage of the experience gained during the qualification tests, see Paragraph 2.6, the simulation of the 14 kW plasma scenario for the ITER TF coil is performed. The analysis aims at assessing the performances of the full magnet during normal and off-normal operation, where the latter includes the mass flow rate reduction in the most critical conductor, the quench propagation and the fast discharge.

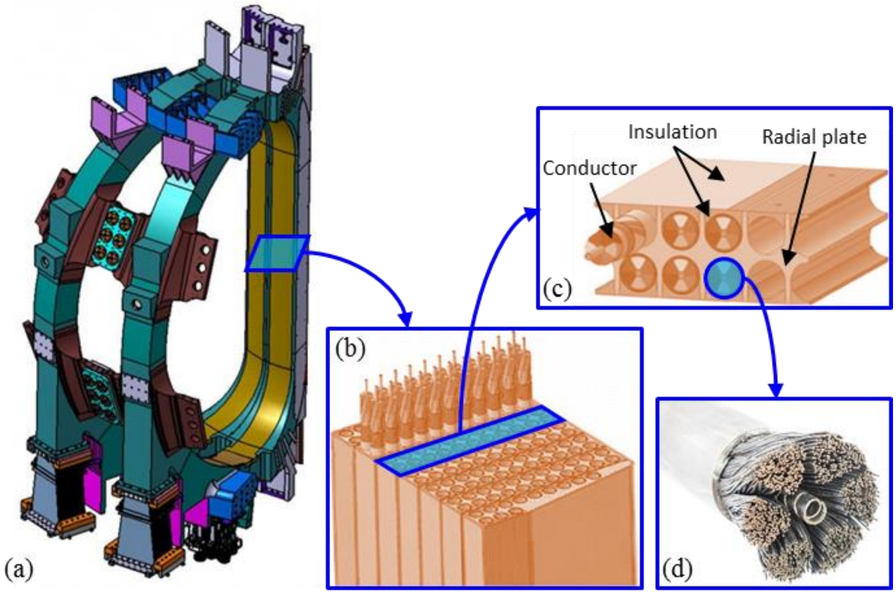

Figure 4.1. (a) Representation of a couple of ITER TF coils (adapted from [97]). (b) WP of the TF coil [14] accompanied by (c) a zoom on a double-pancake enclosed in its radial plate and (d) a picture of the real TF conductor.

4.2. Simulation setup

Here, the 15 MA inductive standard scenario, with total nuclear load of 14 kW, is performed, as done in [98] and [71], together with possible off-normal operating conditions, as done in [99] and [100]. The 4C model of the single TF coil adopted includes the WP, the structures with the CCCs and two cryogenic loops.

An initial stabilization phase including only the static (radiative) heat load on the structure and the circuit is simulated. Then, a series of plasma pulses up to periodic evolution are simulated.

The peak magnetic field in each pancake of the WP is computed with (37), accounting also for the gradient of B on the conductor cross section, see (38). As the conductors are wound in pancakes and the He is supplied from the inner side of the coil, the highest magnetic field is on the first turn and it decreases radially moving outward. The magnetic field maps [71], see for instance Figure 4.2, have been stretched or compressed to comply with the assumption of ideal equal turn length (34 m) for all pancakes, as done for the first time in [70] and then, consistently, in successive analysis [71] [98] [99] [100] [101].

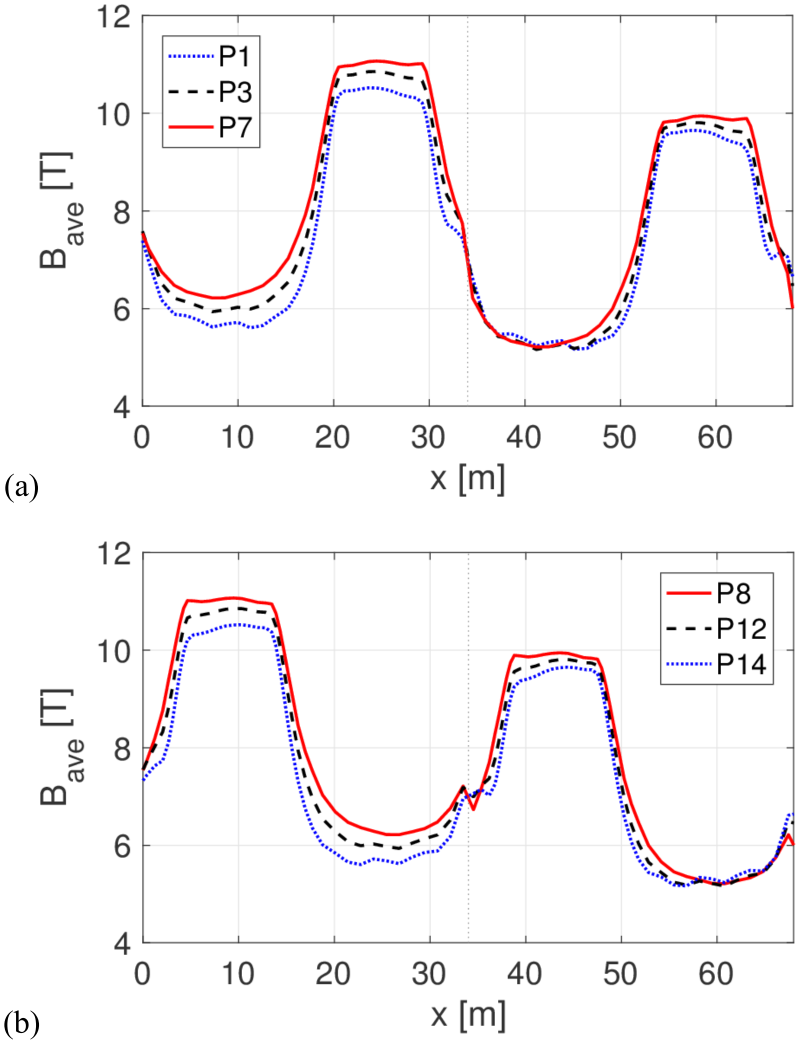

Figure 4.2. ITER TF coil analysis: magnetic field profile at the end of the plasma on the first two turns of (a) pancakes P1 (dotted blue), P3 (dashed black) and P7 (solid red) and (b) P8 (solid red), P12 (dashed black) and P14 (dotted blue).

4.2.1. Geometry, scaling parameters and friction factor correlations

Since the TF coils are wound using the same conductor of the TFI, the geometrical parameters and the coefficients for the scaling formulas in [67] are exactly those reported in Table 2.2 and Table 2.6, respectively, while the adopted friction factor correlations are defined in Paragraph 2.6.1. Finally, concerning the numerical analysis, the values of minimum/maximum time step ($dt = 0.05/0.5$ s) and minimum/maximum mesh size ($dx = 0.001/0.25$ m) are more strict than those reported in [101] and assured to be accurate.

4.2.2. TF structures model

The casing structure of the TF coil is included in the model; discretized, at different poloidal coordinates, in eight 2D cuts, which show a reasonable independence of the results of the numbers of cuts considered as already explained [101] and consistently done in [71] [98] [100]. The outer leg has a rectangular shape and corresponds to sections B1-4, while the inner leg has a wedge-shaped cross section and corresponds to sections A1-4, see Figure 4.3.

The WP is thermally coupled with the casing through the ground insulation, modeled using the glass-epoxy material properties. A total of 74 CCCs [101] is used for the cooling of the casing to which they are thermally coupled by means of 0.15 mm of a resin glue, assumed to be epoxy as done in [71] [98]. The CCCs are represented in Figure 4.3 as small white circles surrounding the ground insulation in green, and are distributed on the various sides of the casing according to Table 4.1.

Table 4.1. Distribution of the CCCs in the ITER TF casing.

Casing side	**Leg**	
	Inboard	**Outboard**
PW	24	
BW	12	
SW (each)	6	

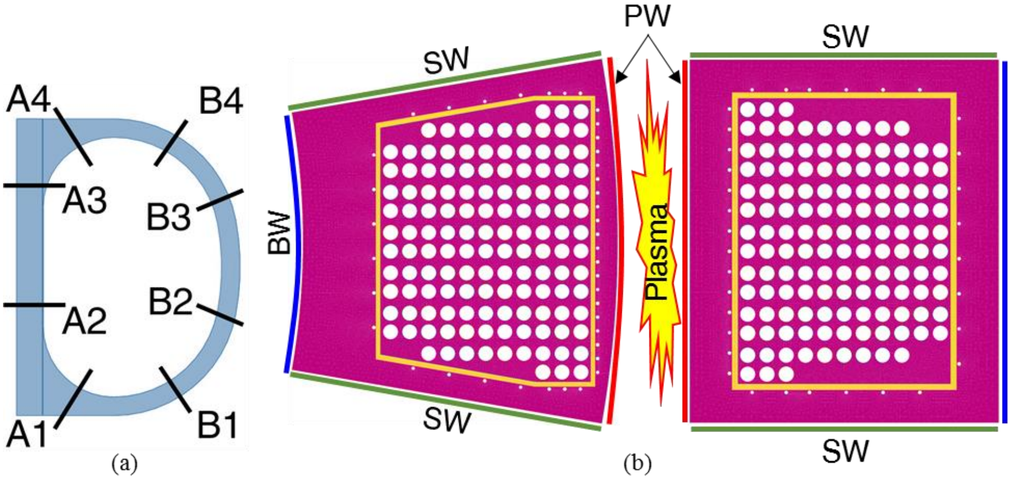

Figure 4.3. ITER TF coil analysis: (a) location of the selected poloidal cuts of the TF coil structures. (b) Cross section of the inboard (left) and outboard (right) legs. Plasma-wall (PW), back-wall (BW) and side-walls (SW) are identified by red, blue and green segments, respectively. SS and ground insulation (glass epoxy) are colored in pink and orange, respectively. The CCCs are the small white circles surrounding the ground insulation.

4.2.3. Circuit model

In the analysis, the single TF coil is connected to two separate SHe loops: one for the WP and one for the CCCs, see Figure 4.4. The loops are properly rescaled, with respect to the dimensions of the actual loop [102], following the assumption that all the TF coils connected in parallel should have the same hydraulic behavior. With this idea in mind, the methodology used to rescale the circuits consists in proportionally reducing the manifold volume and pipeline cross section, to account for the He inventory of a single coil preserving the circuit inertia, while the length of the pipelines is kept equal to the one of the actual loop, so that the transit time in the circuit is unchanged. The circuit rescaled according to this rationale has already been used in [71], [98], [99] and [100]. The main geometrical parameter of the circuit are reported in Table 4.2.

It is assumed that the WP pump provides a total mass flow rate 0.112 kg/s, resulting in 8 g/s in each pancake, while the CCCs pump provides 0.15 kg/s. In the WP loop, downstream the pump, SHe flows inside a HX, releasing heat to a LHe bath kept at 4.3 K. Then, the fluid passes into a cryoline up to the WP feeder, where at its outlet another feeder takes the He back to the pump. The WP inlets and outlets are located at the bottom of the coil, with the He in odd and even pancakes flowing in opposite direction along the D-shaped coil. The CCCs circuit has the same layout, but here from inlets located at the bottom of the TF coil, the CCCs move upwards, where the outlets are connected to two separate feeders: feeder “P” for channels on the plasma side and feeder “U” for all other channels, according to the current design.

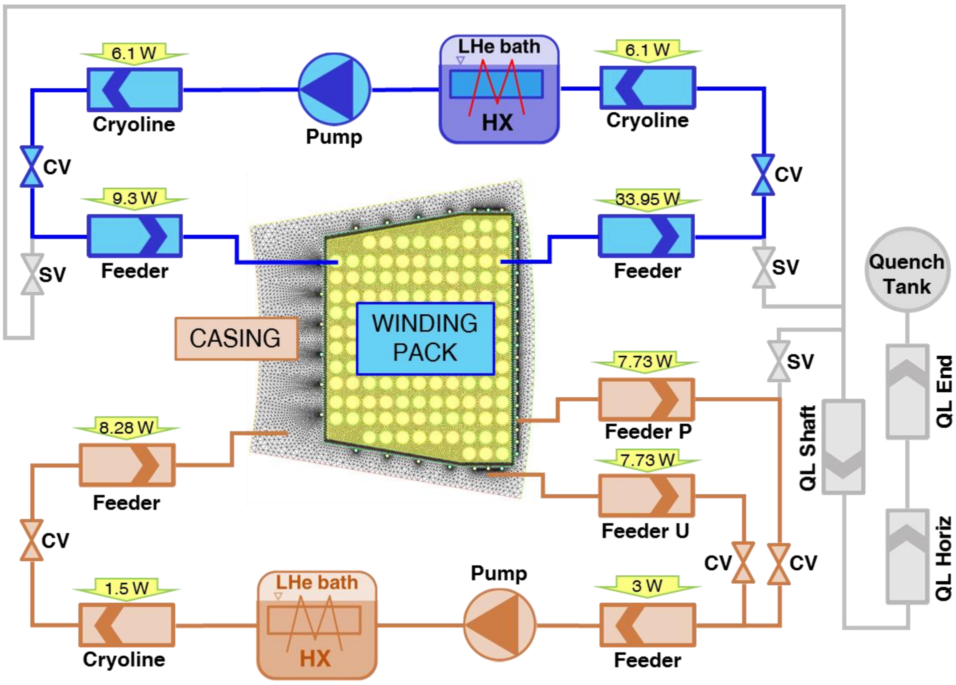

Figure 4.4. ITER TF coil analysis: model of TF winding (blue) and casing cooling (orange) circuits adopted in the model. For each component, the static heat load is also indicated. The quench lines are also reported (grey).

Table 4.2. Main parameters of the cryogenics loops [30].

Circuit	**Component**	**Parameter**	**Value**
Winding	Pump	Flow rate @ Δp = 0 [kg/s]	0.2
		Δp @ zero mass flow [MPa]	0.5
	Supply cryoline	Length / diameter [m / mm]	138.93 / 45.33
	Supply feeder		19.19 / 44.3
	Return cryoline		138.93 / 45.33
	Return feeder		19.19 / 44.3
Winding/Case	HX	Length / diameter [m / mm]	31.0 / 40.0
		Diameter [m]	0.04
		Heat transfer coefficient [W/m^{2}K]	1000
	He bath	Temperature [K]	4.2
Case	Pump	Flow rate @ Δp = 0 [kg/s]	0.8
		Δp @ zero mass flow [MPa]	0.7
	Supply cryoline	Length / diameter [m / mm]	29.48 / 48.32
	Supply feeder		18.81 / 38.96
	Return feeder P		23.79 / 29.4
	Return feeder U		23.79 / 21.9
	Return cryoline		33.05 / 54.33

4.2.4. Heat loads

Heat loads on the conductors

The WP is subject to two main thermal drivers, see Figure 4.5: AC losses and nuclear heat load, as adopted in [71] and [98] since no updated values are available to the author, with the latter applied only during the plasma burn, i.e. from 130 s to

530 s, with peak value on the inboard leg spatial coordinates of the pancake and decreasing values as the spatial coordinate on the pancake moves outward, on successive turns, far from the plasma centre, see Figure 4.6. It is assumed that the energy from the two drivers is entirely deposited in the superconducting strands. Concerning AC losses, it must be stressed that, since the TF operates in DC, the energy deposited originates from the field variations due to the CS and PF coils. The Joule losses in the joints are also considered, assuming 2 nΩ electrical resistance for each of them [103].

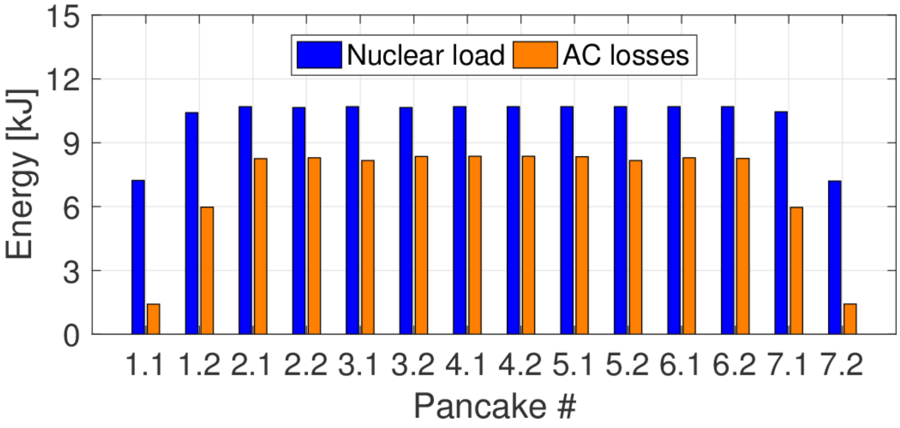

Figure 4.5. ITER TF coil analysis: total energy deposited by nuclear heat load (blue bars) and AC losses (orange bars) during the 14 kW scenario plasma pulse.

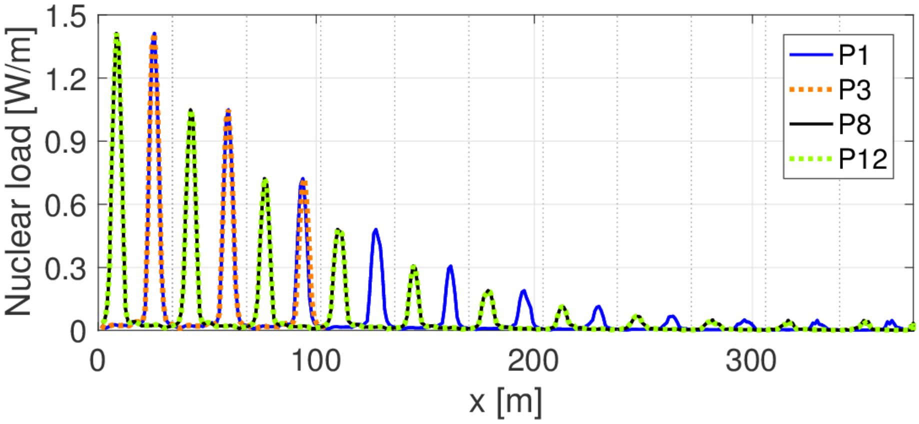

Figure 4.6. ITER TF coil analysis: nuclear heat load spatial profiles on pancakes P1 (solid blue), P3 (dotted orange), P8 (solid black) and P12 (dotted green). The end of each turn is also reported in dotted grey vertical lines.

Heat loads on the structures

For the 14 kW scenario, the spatial distribution of nuclear heat load on the structures sections is shown in Figure 4.7: the peak nuclear heat load is expected on the plasma-wall side of cut A3, located on the inboard leg and close to the equatorial plane. In the reference scenario, the eddy current losses and those for the vertical stabilization of the plasma are taken into account and modeled as a uniformly distributed heat source on the casing walls, see Figure 4.8.

Additionally, the structures are subject to the static heat load, see Figure 4.9, i.e. irradiation from the cryostat and thermal shield and conduction from the gravity support: the peak value is reached on section B2, because it is in direct contact with the gravity support. On the contrary, the radiative heat load is zero on the inboard leg, as the back wall of the casing is facing the cold CS at its same temperature of 4.3 K.

A summary of the heat loads on the WP, structure and cryogenic circuit during the standard plasma pulse is reported in Table 4.3.

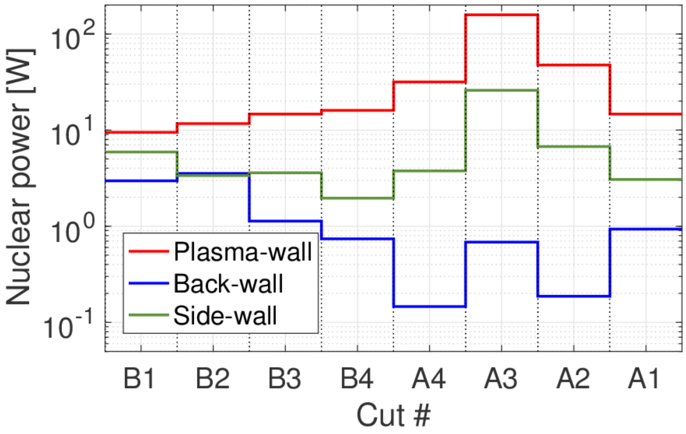

Figure 4.7. ITER TF coil analysis: repartition of the nuclear heat on the structure cuts.

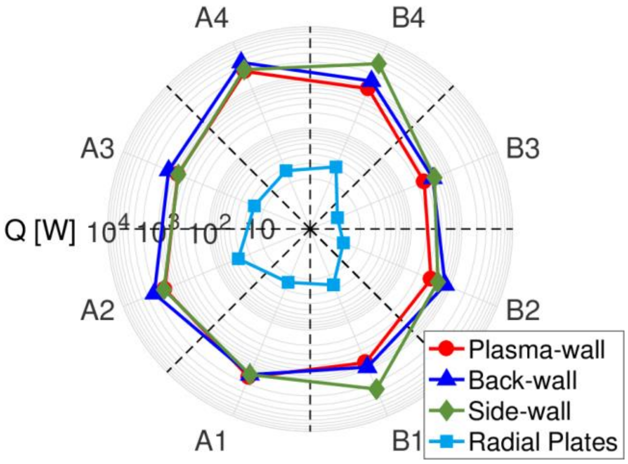

Figure 4.8. ITER TF coil analysis: repartition of the eddy current losses on the structure cuts.

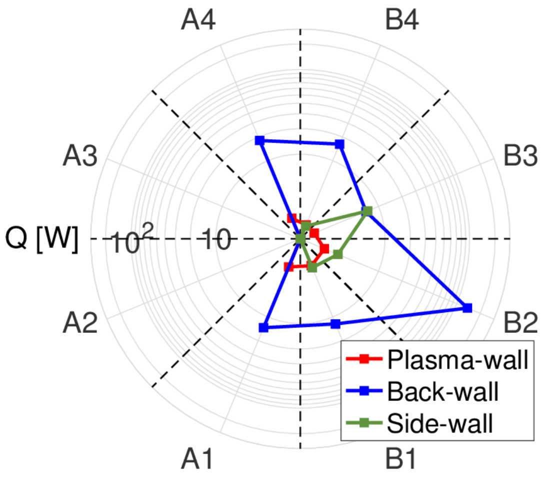

Figure 4.9. ITER TF coil analysis: distribution of the static heat load on structure cuts.

Table 4.3. Heat loads on the TF coil during the plasma pulse of the 14 kW scenario [71].

	Load	**Energy deposited [kJ]**
Heat load on structures	Static radiative heat load	448.3
	Eddy current losses	444.4
	Plasma vertical stabilization	361.1
	Nuclear heating	169.4
Heat load on winding	AC losses + Nuclear heating	239.8
	Joint losses	183.0
Static heat load on circuit	WP circuit	99.90
	CCCs circuit	50.84
Total		1970.24

It must be stressed that the heat loads considered in the present analysis are the same used in [71] so that it is possible to make an as fair as possible comparison between the two analyses. This statement is especially valid for the AC loss energy deposited, since no updated data have been published or are available to the author on the expected AC losses on the ITER TF WP after the TFI test campaign.

4.3. Results

The analysis of the ITER TF operation consists in the simulation of an initial stabilization phase, followed by a series of plasma pulses up the periodic evolution. The present computed results are compared to those obtained in the framework of the activities performed in [71] (in figures referred to as "L. Savoldi, 2014b"). The present analysis and the work carried out in [71] have a lot of inputs in common: the heat loads (see Paragraph 4.2.4), the structure and circuit models; however the main difference lay in the conductor, which, in the present analysis, has different geometrical and superconducting model as discussed in Paragraph 4.2.1 and in the fact that in [71] (and [98], [99], [100]) the Cu heat capacity in the segregated and SC strands was not considered, while it has been accounted in the present analysis for a more realistic and precise simulation.

4.3.1. Initial stabilization

At the end of the initial stabilization phase, the mass flow rate in each pancake has the nominal value of ~8 g/s, see Figure 4.10, supplied with an inlet pressure of ~6.47 bar with a total pressure head of 0.61 bar, ~37% smaller with respect to the 0.97 bar obtained in [71], where different friction factor correlations were adopted. Since side pancakes P1, P2, P13 and P14 are shorter than the other pancakes, in order to uniformly distribute the mass flow rate, some throttling valves, modelled as short pipes, are installed at the outlet of the channel following the same approach used in [70] and lately in [71] [98] [99] [100] [101]. The additional pressure drop of the short pipes is responsible of the slightly different mass flow rate.

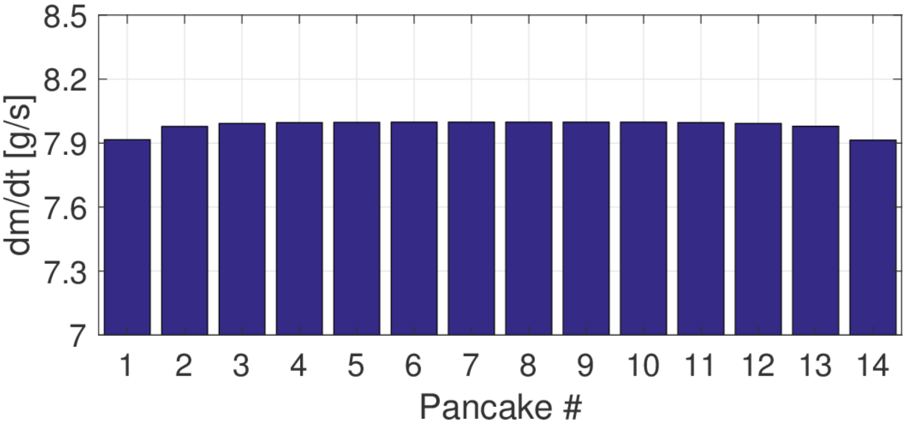

Figure 4.10. ITER TF coil analysis: mass flow rate in each pancake at the end of the stabilization phase.

4.3.2. Normal operation

After an initial stabilization phase, several plasma pulses are simulated up to the periodic evolution starting from the 3rd pulse (i.e. the 4th pulse is equal to the 3rd). Concerning the conditions at the beginning of the periodic plasma pulse, the inlet temperature of the CICCs remains close to ~4.33 K, see Figure 4.11, while near the outlet, the temperature is ~0.2 K higher due to effect of Joule losses in the joints. On the structure, see Figure 4.12, the maximum temperature is ~14 K, clearly above the He inlet temperature: it is located on the BW side of section B2, because of the smaller number of CCCs on that casing side and the peak static heat load in this region, coming from the gravity support.

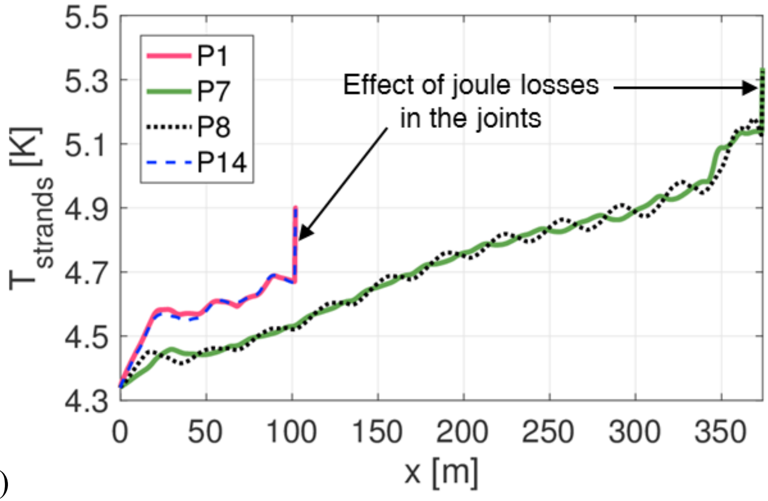

(a)

Figure 4.11. ITER TF coil analysis: (a) strands temperature profile in selected pancakes P1 (solid pink), P7 (solid green), P8 (dotted black) and P14 (dashed blue) and (b) temperature map on section B2 just before the 3rd plasma pulse.

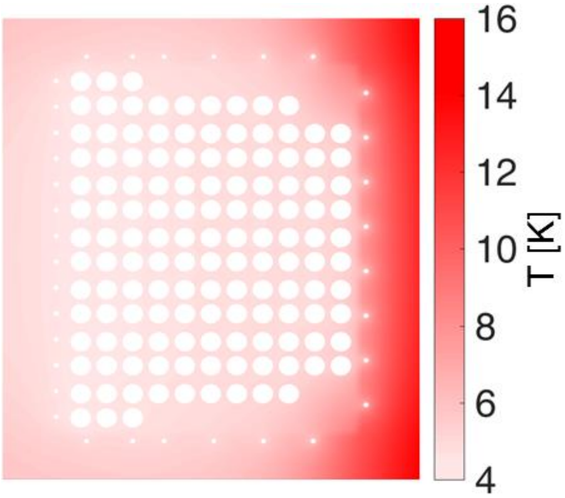

Figure 4.12. ITER TF coil analysis: temperature map on section B2 just before the 3rd plasma pulse.

Maximum strands temperature

During the periodic pulse the $T_{strands}^{max}$ is <6.0 K, see Figure 4.13, and it is reached at ~70 s after the end of the plasma burn. The highest strand temperatures are reached in pancake P3, and symmetrically in pancake P12, instead of occurring in the central ones as expected. In fact, even if the total AC losses and nuclear heat loads are the same for the pancakes, see Figure 4.5, P3 and P12 are subject to a larger energy transfer with the structures, see Figure 4.14. The $T_{\mathrm{strands}}^{\mathrm{max}}$ evolution change, see Figure 4.15, sudden in P1 and smoother in P14, is related to a change in its positions: at the beginning of the pulse, the maximum is close to the outlet of the pancake, where also the joints are located, but during the plasma burn the location of the hot-spot temperature moves on the first turn of the pancakes, where the heat load is larger. Figure 4.15 shows that the $T_{\mathrm{strands}}^{\mathrm{max}}$ for present simulation is always lower than the results obtained in [71] since the Cu heat capacity, here, is taken into account.

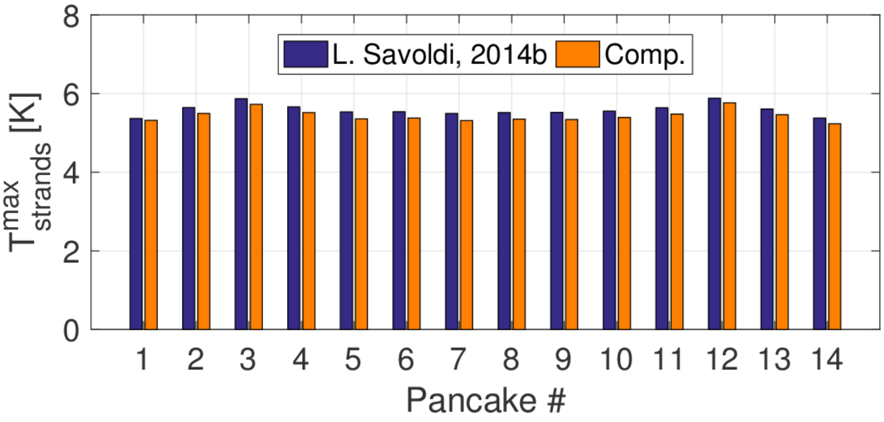

Figure 4.13. ITER TF coil analysis: $T_{\mathrm{strands}}^{\mathrm{max}}$ in all pancakes during the periodic pulse comparing present results (orange bar) with those obtained in [71] (blue bars).

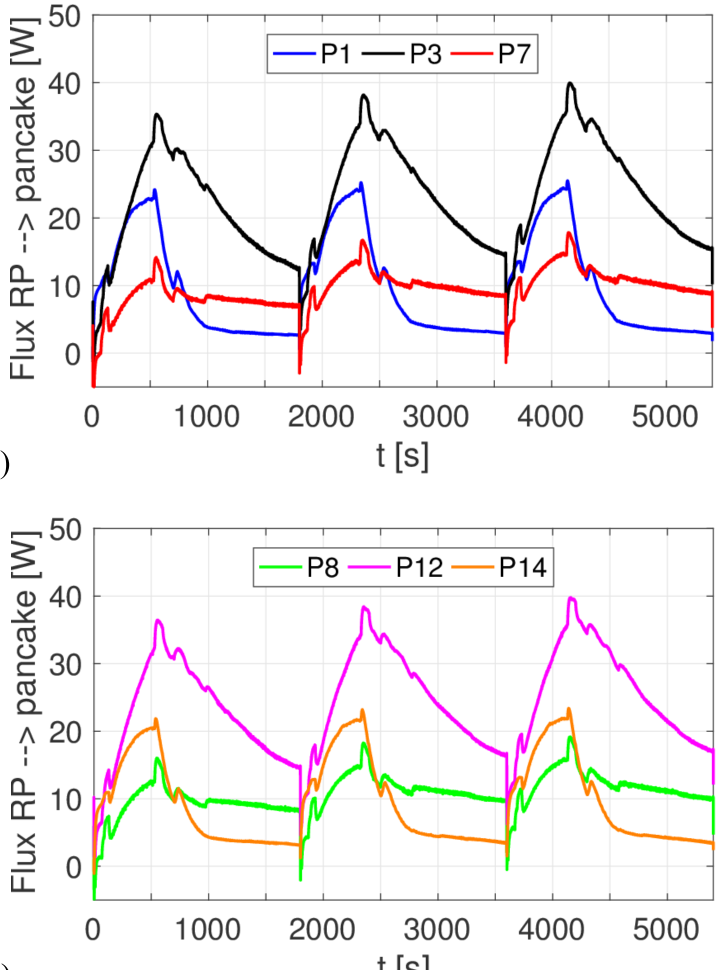

(a)

(b)

Figure 4.14. ITER TF coil analysis: heat flux from the RP to pancakes (a) P1 (blue), P3 (black), P7 (red) and (b) P8 (green), P12 (magenta) and P14 (orange).

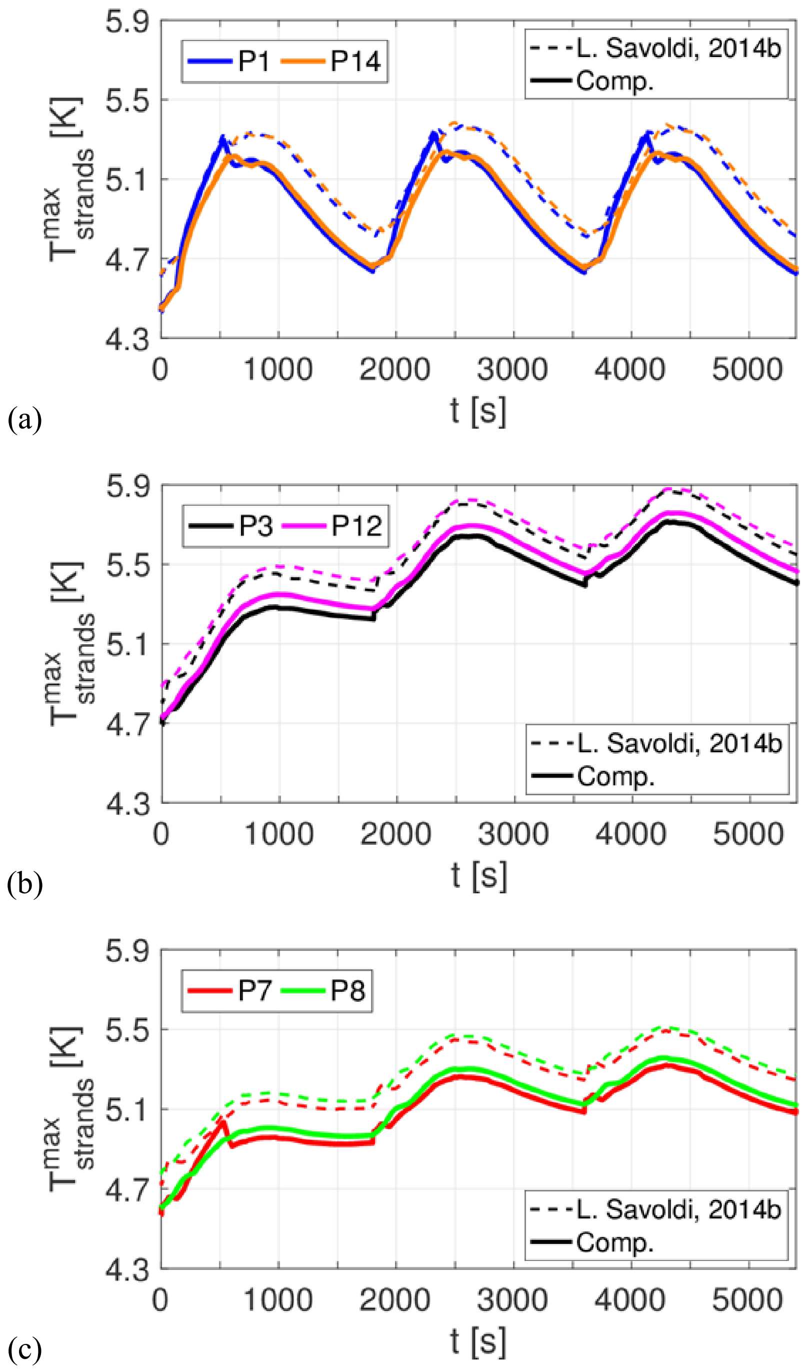

Figure 4.15. ITER TF coil analysis: evolution of $T_{\mathrm{strands}}^{\mathrm{max}}$ in pancake (a) P1 (blue), P14 (orange), (b) P3 (black), P12 (magenta) and (c) P7 (red), P8 (green) comparing the present results (thick solid line) with those in [71] (thin dashed line).

Minimum temperature margin

In each pancake, the predicted $\Delta T_{\mathrm{marg}}^{\mathrm{min}}$ (evaluated at B_{ave} on the conductor cross section) is reached at the end of the plasma (530 s) and it is located, for odd and even conductors respectively, approximately in the first and last third of the first turn, see Figure 4.16, as a result of the counter-current flow of the channels. Nevertheless, all pancakes satisfy the requirement of ~0.7 K, with a minimum value of ~1.1 K reached in P7. It must be stressed that the present simulation aims at predicting the operation in “standard” conditions with respect to the real operation of the machine. It may be rightly argued that for conservative reasons, the assessment on whether a minimum temperature margin is or is not fulfilled should be based on the scaling parameters of the worst performing TF conductor. However this is not the main objective of the work, which instead aims at predicting the operation of the coil with the available nominal data of the conductor adopted taking advantage of the experience acquired during the TFI test campaign.

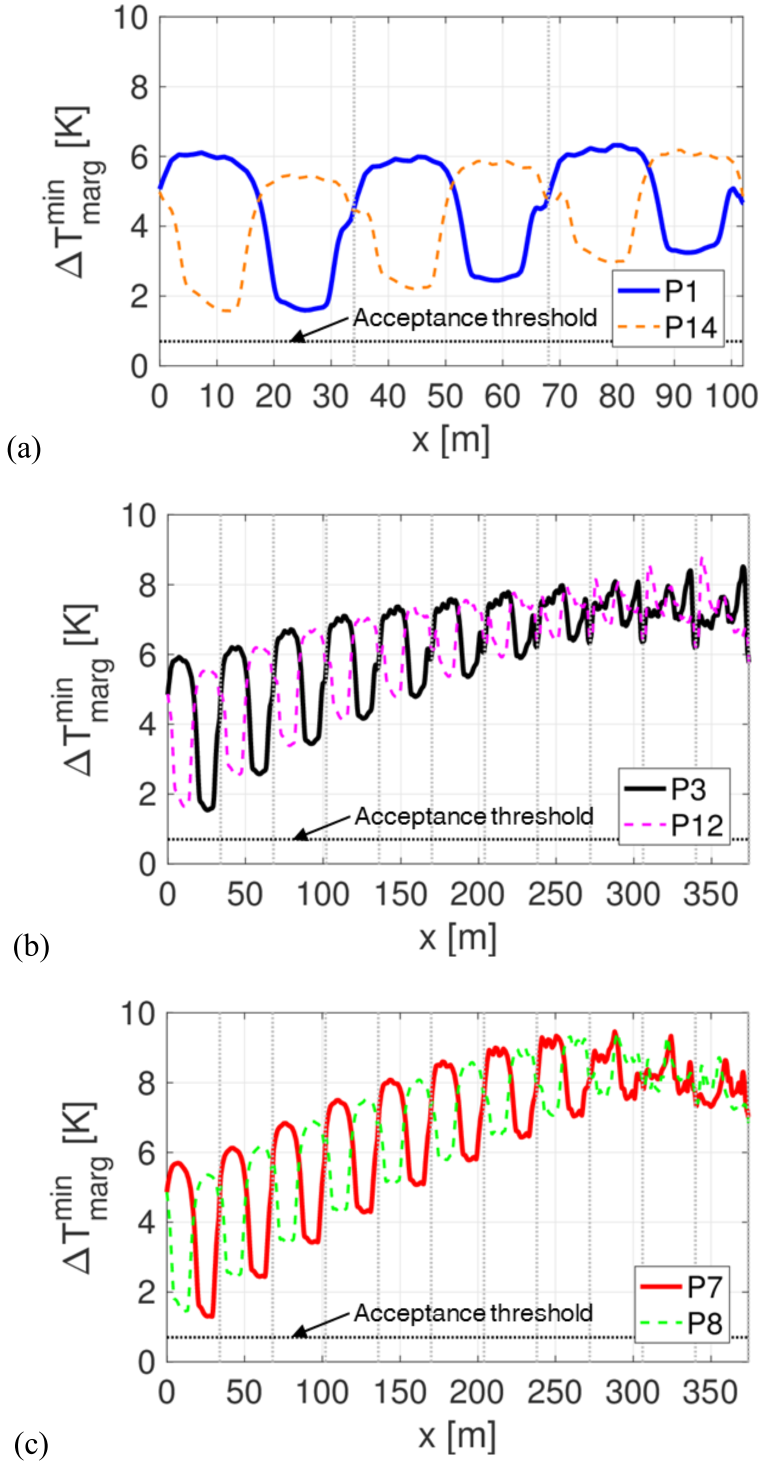

Figure 4.16. ITER TF coil analysis: profile of ΔT_{marg}^{min} in pancake (a) P1 (blue), P14 (orange), (b) P3 (black), P12 (magenta) and (c) P7 (red), P8 (green) for present simulation. Grey dotted lines indicate the end of each turn and the black dotted line indicates the 0.7 K ΔT_{marg}^{min} acceptance threshold.

When compared to results in [71], see Figure 4.17, the predicted $\Delta T_{\mathrm{marg}}^{\mathrm{min}}$ is ~0.47 K larger for two main reasons: in [71] the heat capacity of the Cu strands was not considered following over-conservative assumptions and because, as previously mentioned, in [71] the applied strain (from [66]) was higher. If the margin is evaluated at B_{max}, the minimum margin is ~0.3 K lower in every pancake, but still above the 0.7 K threshold [61].

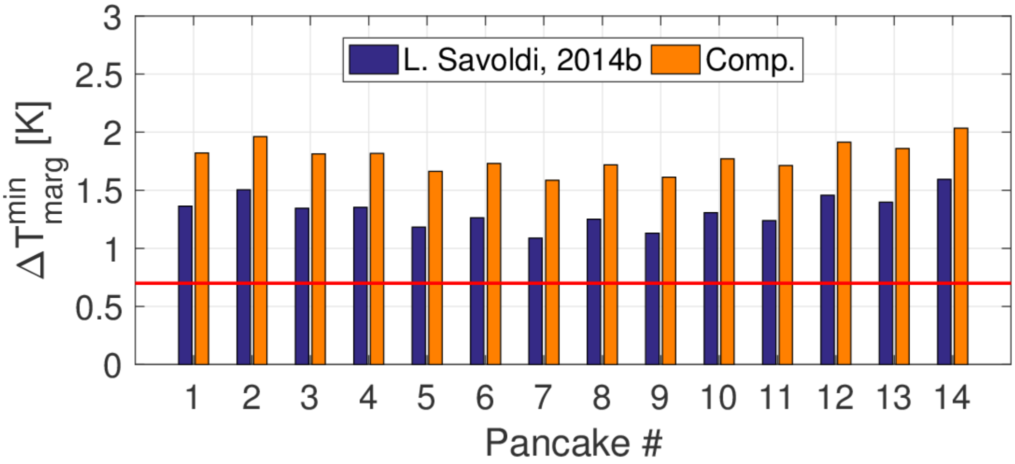

Figure 4.17. ITER TF coil analysis: $\Delta T_{\mathrm{marg}}^{\mathrm{min}}$ in all pancakes during the periodic pulse comparing present results (orange bars) with those obtained in [71] (blue bars).

The $\Delta T_{\mathrm{marg}}^{\mathrm{min}}$ starts decreasing, see Figure 4.18, in the first ~70 s for the AC losses induced by the change of CS magnetic field. At ~70 s, the small discontinuities on the $\Delta T_{\mathrm{marg}}^{\mathrm{min}}$ evolutions, already observed in [71], are related to the change in position of the minimum value onto a coordinate (of the first turn) where the heat load deposited during the plasma pulse is smaller, see Figure 4.6. Then, from 70 s to 530 s, the erosion of the temperature margin is mainly due to the temperature increase following the nuclear heat load deposition. Then from $t > 530$ s to the end of the pulse (1800 s), the margin starts increasing again because the strands temperature starts decreasing as the heat is evacuated from the coil and since the thermal heat load is very small during the dwell.

Following the outcome of Figure 4.13, it is expected that the $\Delta T_{\mathrm{marg}}^{\mathrm{min}}$ is located in one of the hottest channels, however this is not true because the magnetic field is slightly higher (~0.2 T) on the central pancakes, see Figure 4.2. The combination of the higher magnetic field and of the more severe strain produces a T_{CS} reduction of ~0.2-0.3 K in pancake P7 rather than in P3 or P12.

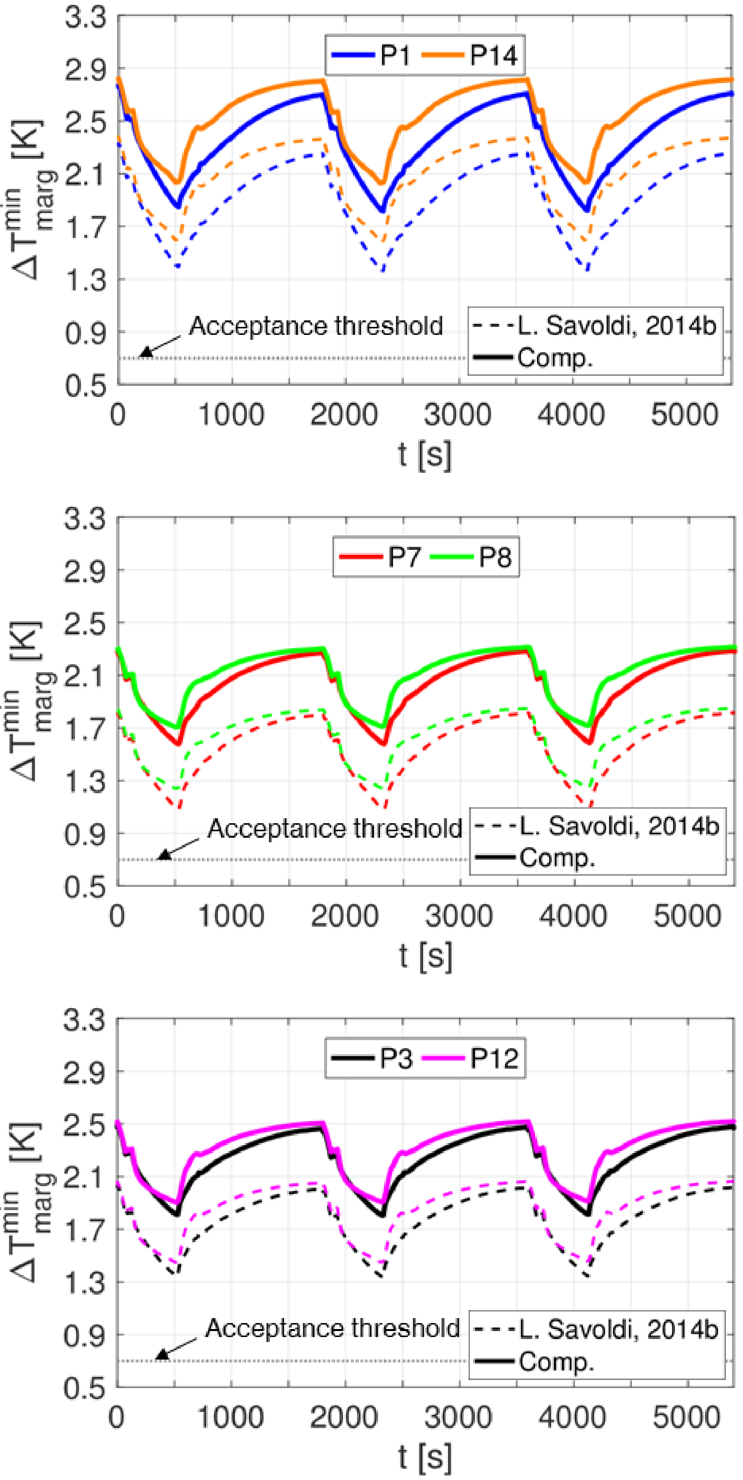

(a)

(b)

(c)

Figure 4.18. ITER TF coil analysis: evolution of ΔT_{marg}^{min} in pancake (a) P1 (blue), P14 (orange),(b) P3 (black), P12 (magenta) and (c) P7 (red), P8 (green) comparing the present results (thick solid line) with those in [71] (thin dashed line).

Circuit results

The pressure at inlet and outlet of the WP and CCCs, see Figure 4.19, shows a periodic evolution starting from the 3rd pulse, as well. Looking at the periodic pulse, in the first ~600 s, the pressure in the WP (p_{max} ~8.7 bar) and CCCs (p_{max} ~10 bar) circuits increase as a consequence of the heat deposition. Note that, for sake of simplicity, only results from present simulations are reported, refer to [71] [98] for the comparison. When the power decreases, the peak pressure starts decreasing, recovering its initial value before the beginning of the pulse. During the periodic pulse, the peak power extracted by the WP and CCCs HXs is ~625 W and ~1100 W, see Figure 4.20, reached at ~900 s and ~600 s after the start of the plasma pulse, respectively.

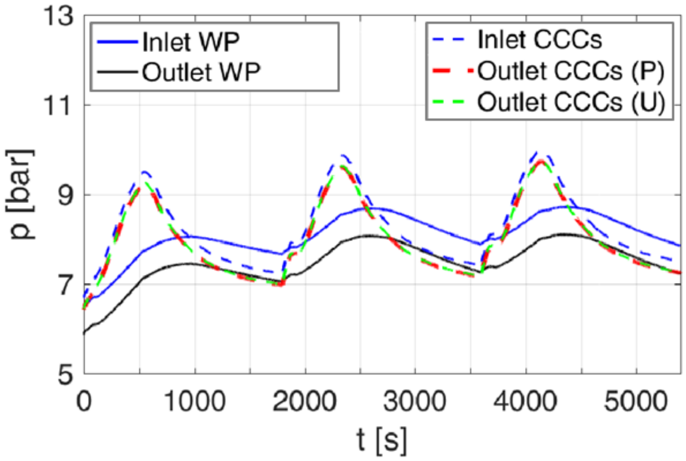

Figure 4.19. ITER TF coil analysis: pressure at the WP (solid lines, inlet: blue, outlet: red) and at the CCCs (dashed lines, inlet: blue, outlet feeder P: red, outlet of feeder U: green) during the first three plasma pulses up to periodic evolution.

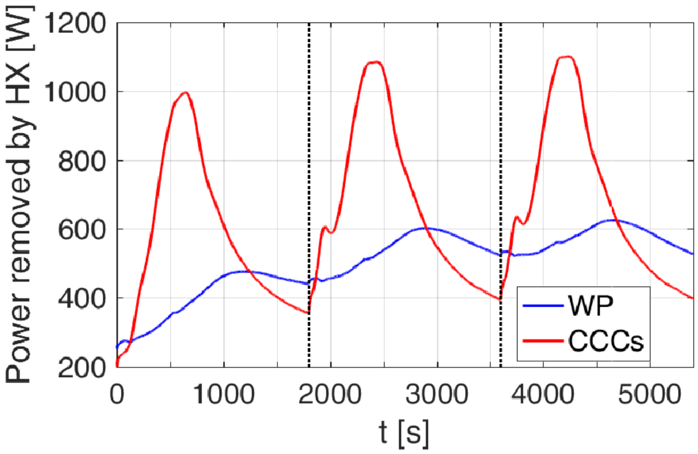

Figure 4.20. ITER TF coil analysis: power extracted by the HXs during the first three plasma pulses up to periodic evolution in the WP (blue) and CCCs (red) loops.

Structures

The maximum temperature on the structures, see Figure 4.21, is reached ~530 s, after the beginning of the plasma pulse and it is always located on section B2, because it is subject to the highest static heat load (conduction from the gravity support), superimposed to the nuclear heat load. The heat flux, transferred from the casing to the RPs through the ground insulation, is shown in Figure 4.22 separately for BW, SW and PW: while on the PW the effect of the nuclear heat load is clearly visible and predominant, with respect to the contribution of the static load, this is not true on the BW, where the nuclear heat load is smaller (interface further from the plasma) but it has to face higher heat fluxes (see for instance in section B2) with a smaller number of CCCs with respect to other surfaces.

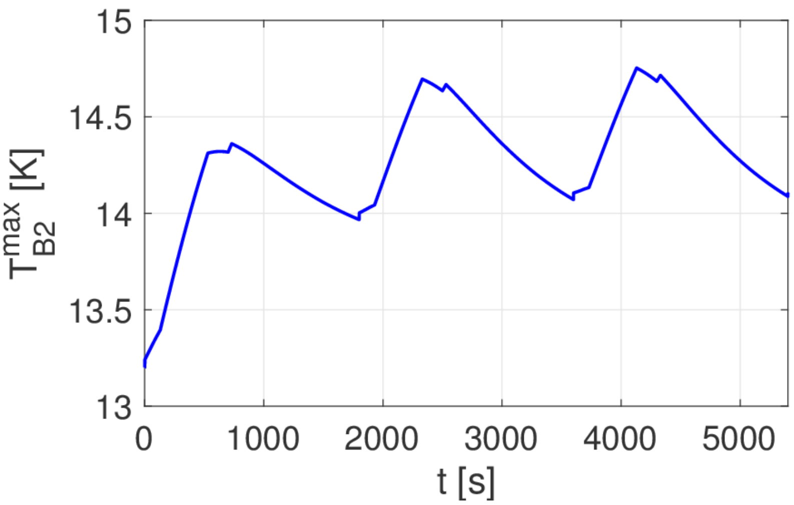

Figure 4.21. ITER TF coil analysis: maximum temperature on cut B2 during the first three plasma pulses (It is stressed that the periodic evolution starts from the 3rd pulse).

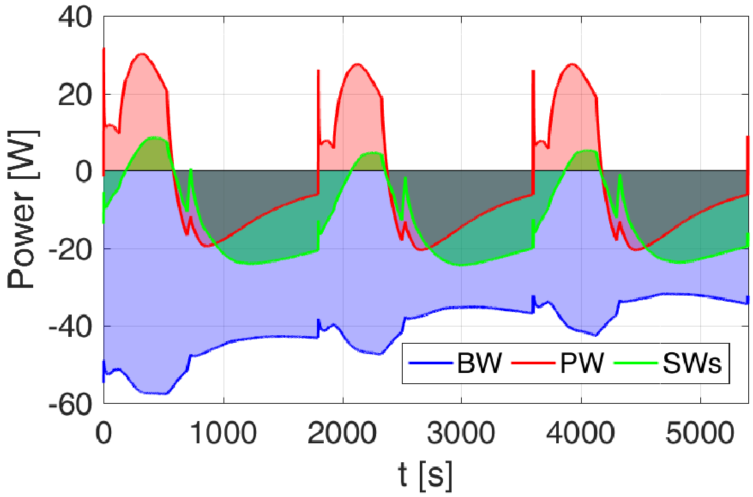

Figure 4.22. ITER TF coil analysis: total heat flux through the ground insulation (positive if entering the RPs) on the case BW (blue), PW (red) and SWs (green) during the first three plasma pulses.

When the heat flux becomes negative, e.g. after the plasma pulse, it means that the flux is transferred from the RPs to the casing. This has a positive effect because the CCCs manage to absorb, through the ground insulation, part of the heat deposited in the WP. This effect could be enhanced by substituting the glass epoxy with a more conductive material, but on the other hand when the heat flows from the casing to the WP, more energy would be transferred as well, turning into a higher load on the conductors.

4.3.3. Off-normal operation

Reduced mass flow rate in the most critical pancake

The first off-normal operating condition considered is the 25% reduction of mass flow rate in the most critical pancake, namely P7. Therefore, the steady state mass flow rate will be ~6 g/s instead of ~8 g/s, see Figure 4.23, with the remaining 2 g/s split among the other pancakes.

Such reduction of mass flow rate leads to an additional erosion of the $\Delta T_{\mathrm{marg}}^{\mathrm{min}} < 0.1$ K, because of the larger strands temperature, see Figure 4.24. Other pancakes are unaffected and, in particular for neighboring pancakes (P6, P8) this is easy to understand since the small additional mass flow rate has to remove the RP heat load not removed by P7.

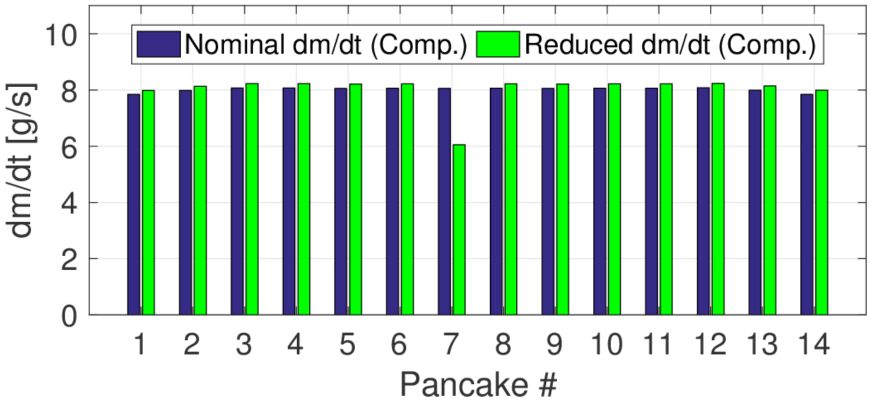

Figure 4.23. ITER TF coil analysis: mass flow rate in each pancake before the plasma pulse during nominal operation (blue bar) and with reduced mass flow rate in pancake P7 (green bar).

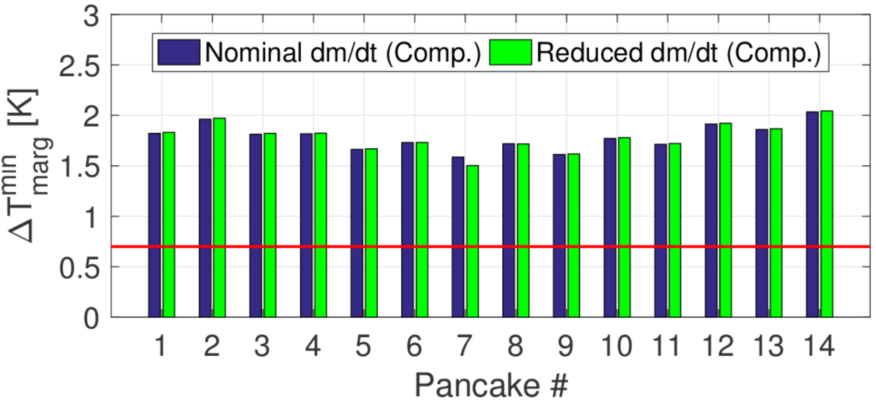

Figure 4.24 ITER TF coil analysis: ΔT_{marg}^{min} in all the pancakes during the periodic pulse in nominal operation (blue bar) and with reduced mass flow rate in pancake P7 (green bar).

Quench propagation

The methodology adopted for the analysis of the quench propagation is the same as reported in [99]; however, in the present simulation, the only difference with respect to [99], is the number of CCCs which is kept constant to 74, for consistency with the analysis of the standard plasma pulse, and therefore not increased to 96 as done in [99]. Of course, a dedicated study on the CCCs number and configuration, beyond the scope of this thesis, may be interesting to develop some mitigation strategy for the heat loads eventually deposited on the structure.

Concerning the simulations strategy, see Figure 4.25: the quench is initiated in the location of the ΔT_{marg}^{min} at the end of burn, i.e. about ~30 m from the inlet of pancake P7, using an external energy deposition of the order of the MQE on a length $L_{heat} = 1$ m during a $t_{heat} = 200$ ms pulse. The current dump (time constant $\tau_{curr} = 11$ s, see Figure 4.26) is triggered 2 s (t_{delay}) after the quench detection, reached when the computed total voltage across the coil is larger than 0.1 V. Then, the current dump will induce large AC losses in the conductor, see Figure 4.27 and Figure 4.28, and eddy current losses in the structure. The cryogenic loop includes a preliminary design of the quench lines (QL) comprising also safety valves (SV, set point 18 bar) to deal with the pressurization, see Figure 4.4. Being the structure highly thermally loaded, in order to maintain a sufficient level of accuracy and a computation trade-off, 16 poloidal cuts are considered equally distributed on the outboard (B1-8) and inboard (A9-16) legs, consistently to what has been done in [99] even if also 8 cuts would have been a satisfactory trade-off.

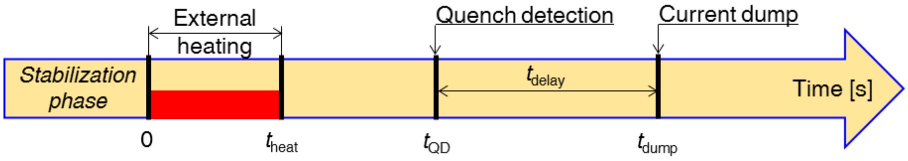

Figure 4.25. ITER TF coil analysis: graphical representation of the quench timeline.

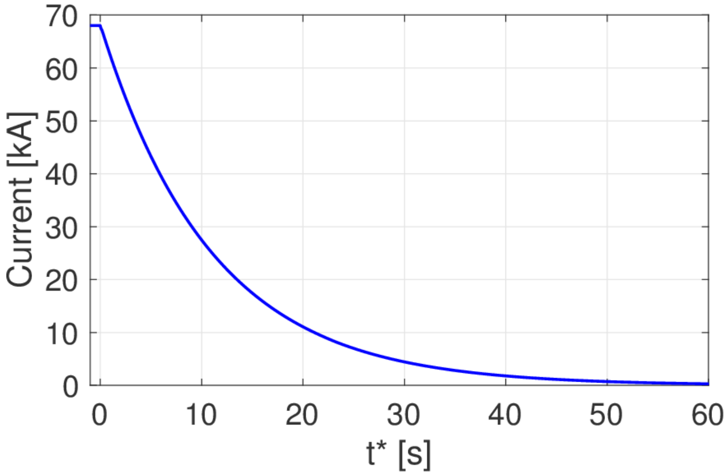

Figure 4.26. ITER TF coil analysis: current evolution during the dump with time constant τ_{curr} = 11 s.

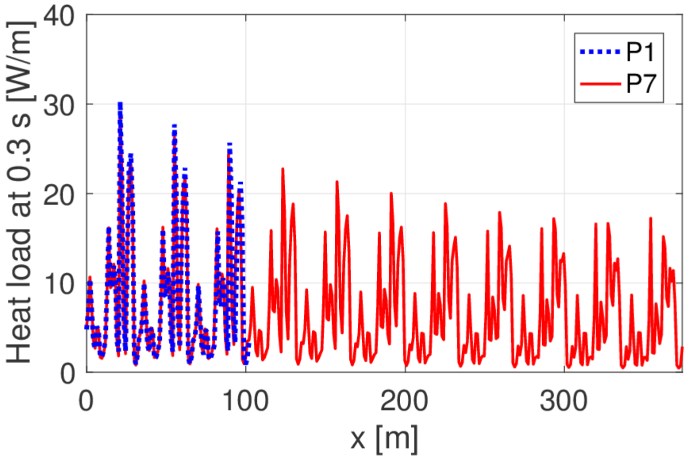

Figure 4.27. ITER TF coil analysis: axial profile of the AC losses at 0.3 s after the dump on pancake P1 (dotted blue) and P7 (solid red).

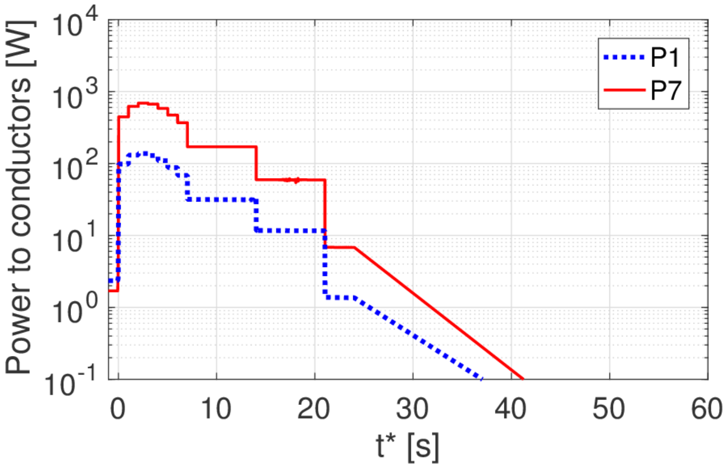

Figure 4.28. ITER TF coil analysis: evolution of the total AC loss power deposited on pancake P1 (dotted blue) and P7 (solid red).

Results, synchronized at the quench detection time $t^* = t - t_{QD}$, where $t_{QD} = 0.15$ s, show that the $T_{\text{hot-spot}}$ is below the design limit [61] during the whole transient for both strands (250 K) and jacket (150 K), see Figure 4.30. The total voltage reaches a maximum of ~1.4 V at the same time (8 s) of the $T_{\text{strands}}^{\text{max}}$, and then they both start decreasing. However, the voltage suddenly jumps again at ~1.4 V at ~18 s when the normal zone (NZ) propagates on the entire pancake length, see Figure 4.31. The NZ is ~10 m long at the time when the peak $T_{\text{hot-spot}}$ is reached, and the propagation speed is larger in high B region, i.e. near the inlet of the pancake. But after the dump, the $\Delta T_{\text{marg}}^{\text{min}}$ is uniformly reduced by the AC losses in the conductor and the heat coming from the RPs, heated by the eddy currents. Therefore, the entire conductor gradually moves toward the normal state, see Figure 4.29, that, when reached, turns into a sudden voltage increase. Again, the increase in the NZ length, initiated at ~34 m from the inlet, see Figure 4.29, and the time at which the whole pancake P7 becomes normal is clearly visible on the NZ characteristic (x,t) plane in Figure 4.31.

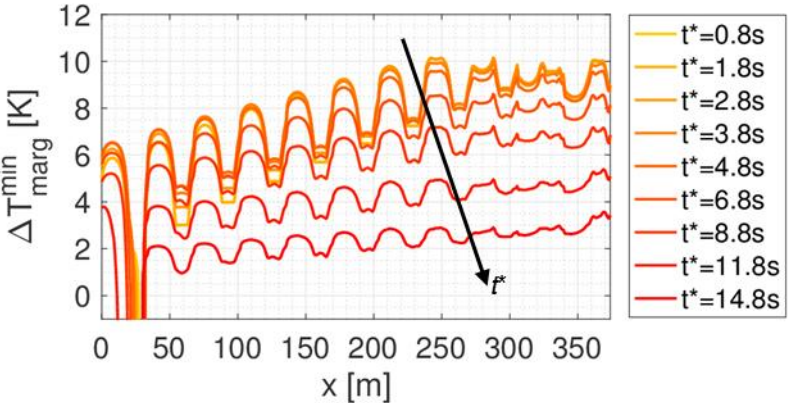

Figure 4.29. ITER TF coil analysis: ΔT_{marg}^{min} profile in P7 at different times during the quench propagation.

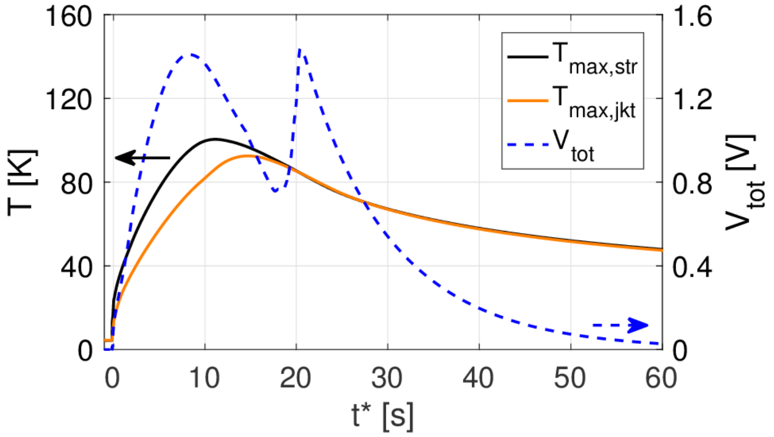

Figure 4.30. ITER TF coil analysis: hot-spot temperature evolution in strands (solid black, left axis) and jacket (solid orange, left axis) in pancake P7. Evolution of total voltage (dashed blue, right axis) across pancake P7 is also reported.

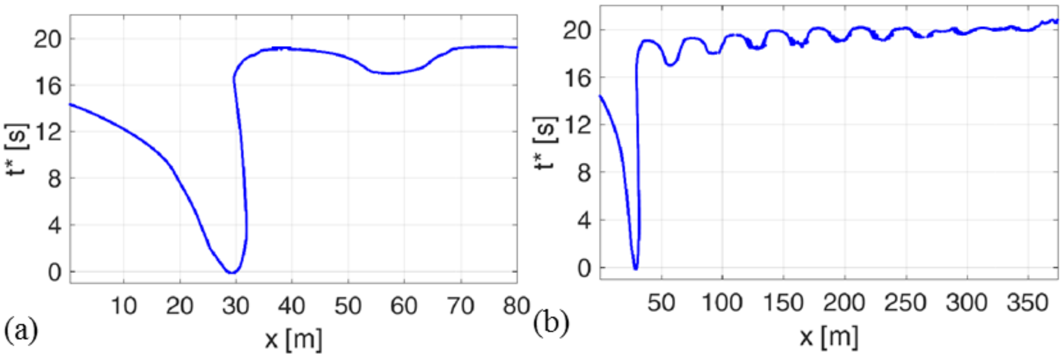

Figure 4.31. ITER TF coil analysis: normal zone propagation with $t_{delay} = 2.0$ s in the characteristic (x, t) plane on (a) the first two turns and (b) on the entire pancake P7 length.

During the quench propagation, P7 shows an initial fast pressure increase due to the external heating disturbance, see Figure 4.32, which is partially re-absorbed until the quench takes-off. The free propagation lasts t_{delay} after the QD until the current is dumped: the large heat deposition (AC losses and eddy currents) induces a strong pressurization in the WP, which causes backflow in all pancakes, see Figure 4.33, but, it never reaches the maximum design value of 25 MPa [61], satisfying the design criteria on the maximum pressure during the quench.

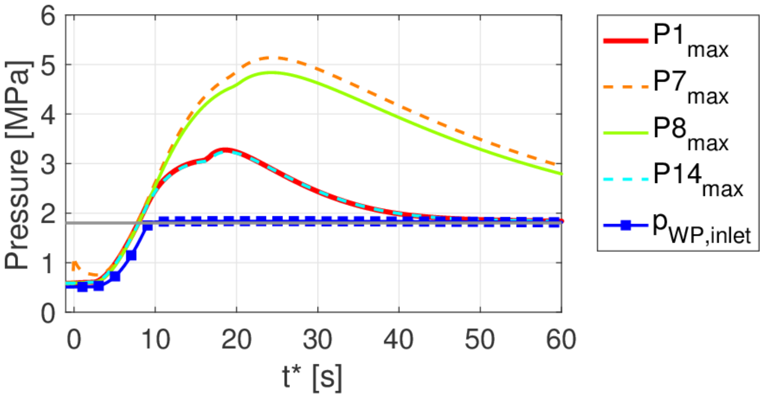

Figure 4.32. ITER TF coil analysis: maximum pressure in selected pancakes P1 (thick red), P7 (dashed orange), P8 (solid green) and P14 (dashed cyan). Inlet WP pressure (blue with squares) and SV set point (solid grey) are also reported.~

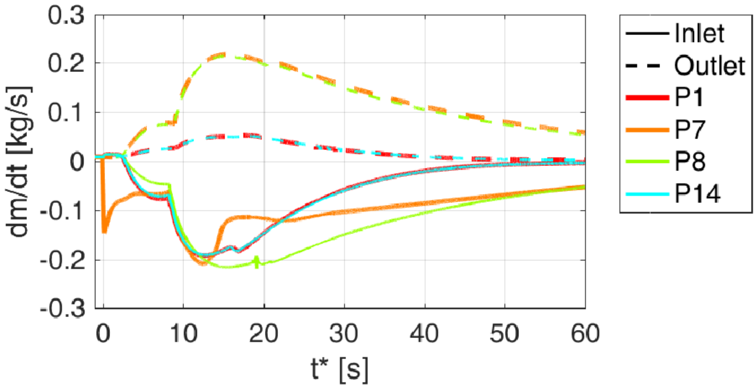

Figure 4.33. ITER TF coil analysis: mass flow rate evolution at the inlet (solid lines) and outlet (dashed lines) of selected pancakes P1 (thick red), P7 (thick orange), P8 (thin green) and P14 (thin cyan).

The pressurization is so violent that, after ~10 s, the SVs on the WP circuit open, see Figure 4.34a, and the pressure of the circuit is lately kept constant at the set point (1.8 MPa) by a PID controller. After the opening of the SVs, He is vented in a quench tank at 4 bar and 80 K. After 60 s from the quench detection, a mass of

~177 kg of He, corresponding to ~51% of the inventory (~347 kg), has been vented, see Figure 4.34b.

The same kind of behavior can be observed in the CCCs, that, being thermally coupled with the heated structures, strongly pressurize, see Figure 4.35a. As in the WP loop, the CCCs circuit reaches the SV opening set point at ~10 s and in 60 s from QD ~12.5 kg of He (~24% of the inventory, namely ~52 kg) have been vented, see Figure 4.35b.

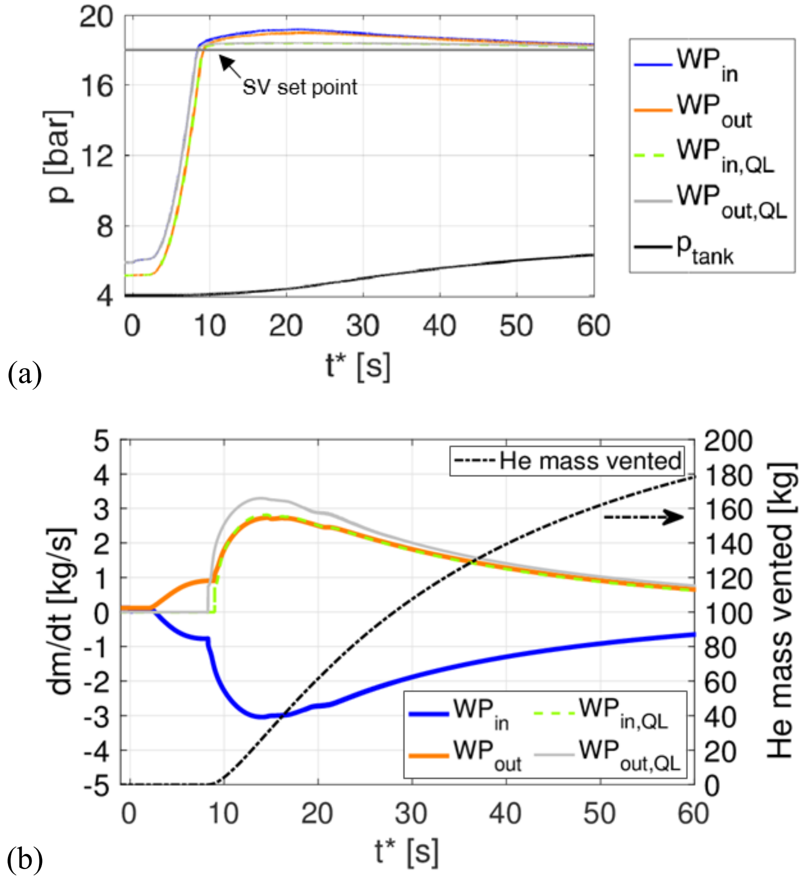

Figure 4.34. ITER TF coil analysis: (a) pressure and (b) mass flow rate evolution in the QLs of the WP circuit.

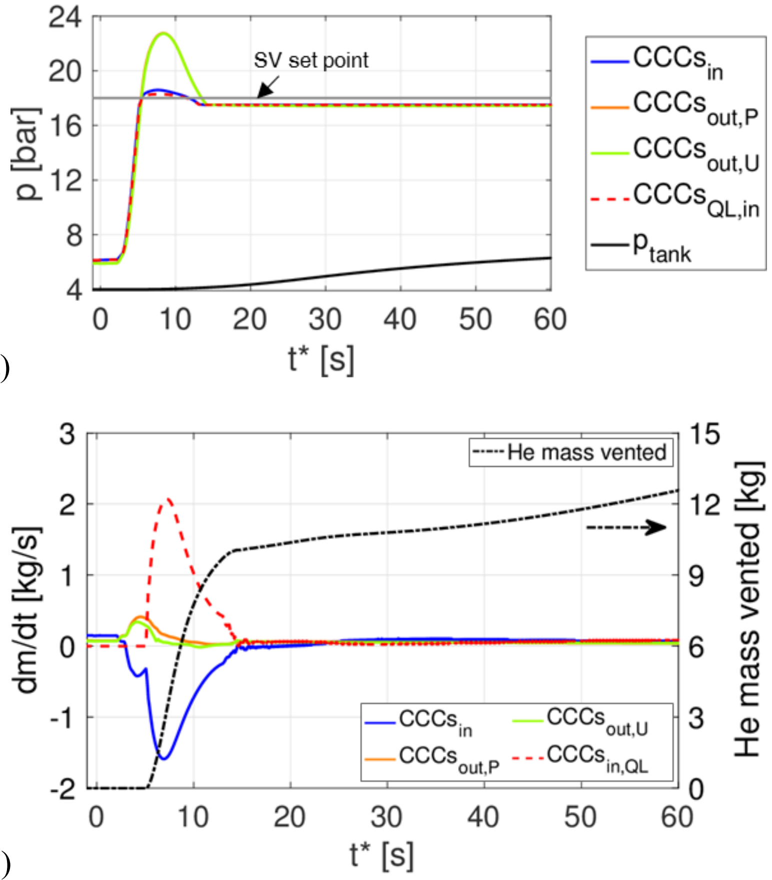

(a)

(b)

Figure 4.35. ITER TF coil analysis: (a) pressure and (b) mass flow rate evolution in the QL of the CCCs circuit.

Fast discharge

In the present simulation, the fast discharge (FD) after 535 s of normal operating conditions (p_{in} = 0.6 MPa, T_{in} = 4.3 K), the current is dumped with the TF discharge time constant τ_{curr} = 11 s. The same QLs design used for the simulation of the quench propagation has been adopted here. The results have then have been compared with those obtained in [100] (in figures referred to as “L. Savoldi, 2012”), in which the FD is triggered after 3 s of plasma disruption, but which indeed does not affect neither the early stages nor the overall evolution of the FD. In the present simulation the structure model shows only one with respect to [100]: the number of CCCs is kept constant to 74, for consistency with the burn and quench analyses, and therefore not increased to 96 as done in [100].

The results, synchronized at the current dump time t^*, show that the power deposited during the transient induces quench in all the conductors, starting from the four shorter pancakes (P1, P2, P13, P14), see Figure 4.36, due to the heat coming from the casing (and RPs). In fact, even if all the pancakes are in contact with the RPs, the side pancakes have a longer contact length, and therefore a more effective heat exchange, see Figure 4.14, with the rest of hot casing heated by the AC losses. The quench is initiated at the $\Delta T_{\mathrm{marg}}^{\mathrm{min}}$ location but quickly propagates on the entire length. The computed voltage is lower with respect to [100], because the stabilization effect of Cu is considered. Moreover, Cu additionally contributes as thermal capacity to reduce the $T_{\mathrm{hot\text{-}spot}}$, which is <35 K after 60 s of discharge, see Figure 4.37.

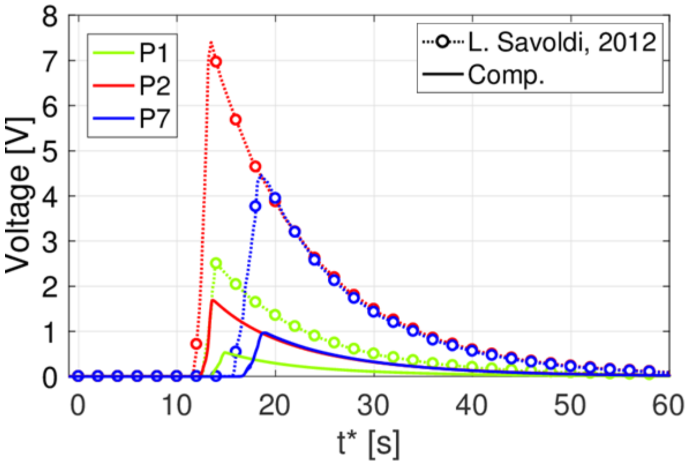

Figure 4.36. ITER TF coil analysis: voltage evolution during the FD on selected pancakes: P1 (green), P2 (red) and P7 (blue), comparing present results (solid lines) with those from [100] (dotted lines with circles).

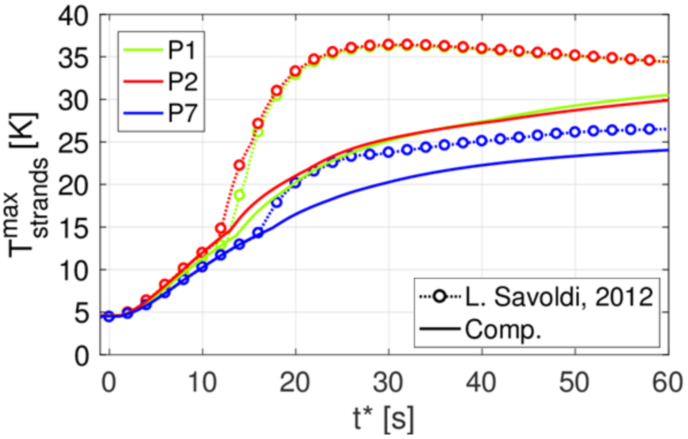

Figure 4.37. ITER TF coil analysis: $T_{\mathrm{strands}}^{\mathrm{max}}$ evolution during the FD on selected pancakes P1 (green), P2 (red) and P7 (blue), comparing present results (solid lines) with those from [100] (dotted lines with circles).

The pressure in the WP reacts first to the heat deposition following the dump ($t^* < 12$ s), see Figure 4.38, leading to the opening of the SV at t^* ~8 s, which reduces the pressurization slope. Lately, the pressurization accelerates as a consequence of the quench propagation ($t^* > 12$ s) reaching a peak value of ~5.9 MPa, which satisfies the ITER design criteria [61] and is ~30% lower than the value obtained in [100], because of the smaller friction foreseen in the cable, see Figure 2.26, and the smaller joule heat generated (the Cu is considered here as a stabilizer).

Concerning the mass flow rates, see Figure 4.39, the feeders of both WP and CCCs show strong flow reversal at the inlet and expulsion at the outlet, with a change in slope at the time of the SVs openings. Despite lower pressurization, present results show a stronger backflow with respect to [100], because even if the Δp is lower, the lower friction factor makes it easy to push He out of the coil, as it can be inferred from Figure 2.26.

When the WP and CCCs SVs open, He is vented to the quench tank, see Figure 4.40. The CCCs SV opens first (t^* = ~2 s) and the vented mass flow rate reduces quickly due to the small amount of He in its circuit. The SVs on the WP circuit start venting at t^* = ~8 s, with a longer He expulsion and with a larger amount of mass discharged. The predicted total He mass vented is ~155 kg (~40% of the inventory), in the same ball-park of [100].

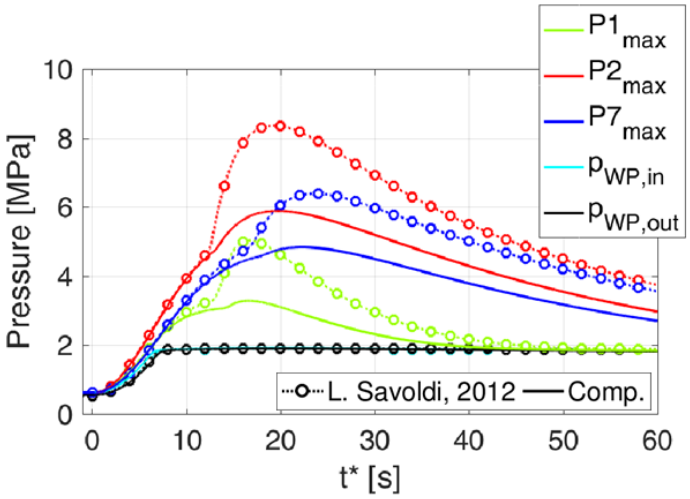

Figure 4.38. ITER TF coil analysis: evolution of maximum pressure in selected pancakes P1 (green), P2 (red) and P7 (blue) and pressure at the boundary of the WP (inlet: cyan, outlet: black). Present results (solid lines) are compared with those from [100] (dotted lines with circles).

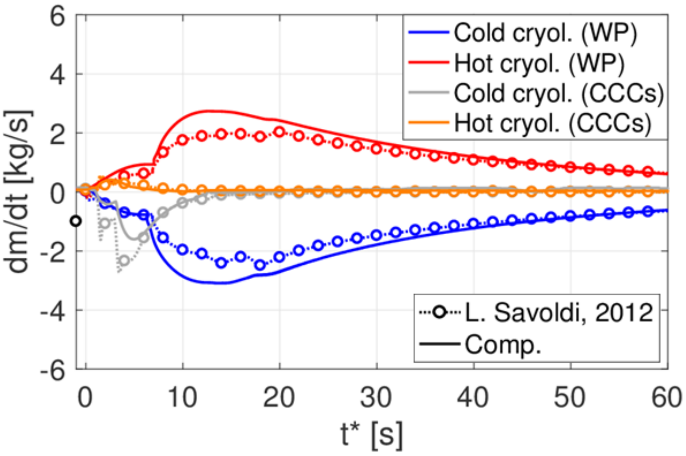

Figure 4.39. ITER TF coil analysis: evolution of mass flow rate at the boundaries of both WP (inlet: blue, outlet: red) and CCCs (inlet: grey, outlet U feeder: orange) feeders. Present results (solid lines) are compared with those from [100] (dotted lines with circles).

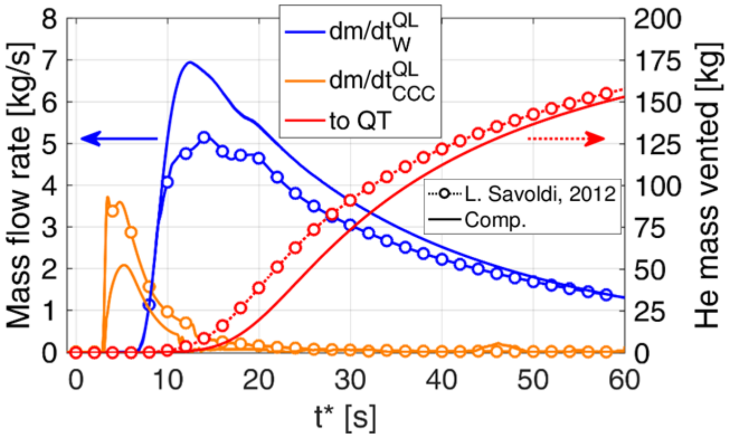

Figure 4.40. ITER TF coil analysis: mass flow rate vented from the WP (blue) and CCCs (orange) QLs (left axis) comparing present results (solid lines) with those from [100] (dotted lines with circles). The total He mass vented (red) is also shown (right axis).

4.4. Conclusions

The thermal-hydraulic analysis of the ITER TF coil has been performed in normal and off-normal operating conditions.

The results of the predictive simulation of the normal operation show that all the pancakes satisfy the requirement on the $\Delta T_{\mathrm{marg}}^{\mathrm{min}}$. However, some kind of mitigation of the static heat load (enhanced refrigeration of the casing by the CCCs or of the gravity support by dedicated channels) may be beneficial for the $\Delta T_{\mathrm{marg}}^{\mathrm{min}}$.

Concerning the off-normal operation, if the most critical pancake P7 faces a reduction of the mass flow rate by ~25%, its $\Delta T_{\mathrm{marg}}^{\mathrm{min}}$ is additionally eroded of less than 0.1 K: without any other incidents, this should not represent a significant danger during the 14 kW plasma scenario.

Concerning the quench propagation, when the normal zone initiated in the location of the $\Delta T_{\mathrm{marg}}^{\mathrm{min}}$, i.e. the most likely case, the hot-spot temperature, both in strands and jacket, and the maximum pressure in the WP remain below the prescribed design limits. However, following the dump, the power deposition in the casing induces a strong pressurization in the CCCs circuit leading to the opening of the safety valve with the successive venting of about one fourth of the total He inventory of the circuit in 60 s. Similarly, a strong pressurization occurs also in the WP loop, which vents about half of its He inventory in about one minute. For this reason, it can be stated that a careful analysis and design of the quench lines is necessary.

In addition to the off-normal operation analysis, during the fast discharge a quench is firstly induced in the shorter side pancakes because of the energy transferred from the radial plates, heated by the eddy losses. In a second time, quenches are initiated in all the other pancakes, again as a consequence of AC losses deposition and heat transfer from the RPs. During the discharge, both cryogenic loops pressurize as a consequence of the heat deposition, with the WP circuit suffering of a stronger pressurization due to joule energy deposited during the quench. The pressurization of the circuits causes the opening of the safety valves, thus the importance of the QLs design is stressed again. Finally, in order to reduce the possibility of a quench, it may be interesting to evaluate some solutions to reduce the heat transfer from the radial plates to the WP, for instance by cutting the thermal coupling between the WP and the casing; if this cannot be considered for ITER, it may be interesting for other future fusion machines.

Chapter 5

Conclusions and perspectives

Given the need of reliable computational tools in research and engineering, the detailed validation of the 4C code has been presented in this work. The code first undergoes several validation exercises against data collected during the ITER Central Solenoid and Toroidal Field Inserts test campaigns, then it is applied for predictive simulations of the ITER Central Solenoid and Toroidal Field coil operation.

Multiple validation exercises have been performed during the analysis of the measurements from the latest Central Solenoid Insert experimental campaign carried out in 2015, thanks to the large amount of data collected during the extensive test program. Concerning the hydraulic characterization, the friction factor correlations, available in literature, for the Central Solenoid conductor geometry are suitable to reproduce the hydraulic characteristic of the conductor within 30%, apart from some uncertainties on measurements. Then the data collected on the Central Solenoid Model Coil helped to calibrate the inter-turn and inter-layer thermal coupling feature of the 4C code, by validating the results of the cooldown simulation against measurements. During the campaign, it has also been possible to evaluate the DC performances of the Central Solenoid Insert coil in terms of T_{CS} and effective strain applied to the ITER Central Solenoid coil, which, thanks to the observed beneficial effects of the hoop strain, turned out to be smaller than what was previously estimated. Finally, the experimental test plan included also the measurement of the AC losses in the conductor: by means of the analysis of the data collected on the Central Solenoid Insert coil, a simplified analytical model for power deposition has been developed and validated against experimental data. Thanks to such analytical model, it has been possible to obtain the coupling time constant, both at the beginning of the coil operation (virgin conductors) and after several electro-magnetic cycles (cycled conductors). The values of the coupling time constant retrieved have then been used in the predictive simulation of the ITER Central Solenoid coil operation.

Later on, the Toroidal Field Insert experimental campaign took place in 2016-2017. The first tests were dedicated to the thermal-hydraulic characterization of the coil: the friction factor correlations available in literature are able to properly capture the hydraulic impedance of the conductor. Moreover in the initial phases of the tests, the 4C code has been used to calibrate the thermal-hydraulic constitutive relations of the conductor, including the hole-bundle and the conductor-mandrel heat transfer coefficient. Lately during the tests, the effects of electro-magnetic and thermal cycles on the T_{CS} have been assessed, showing that the degradation of the T_{CS} may need some additional thermal cycles before reaching saturation. Finally, for the first time, the 4C code has been used to strictly predict the quench propagation in the coil, showing good-to-excellent predictive capabilities for the most relevant quantities, despite some smaller uncertainties.

The second part of the work deals with the application of the tool: since the ITER machine is being built and the thermal-hydraulic performance of the Central Solenoid and the Toroidal Field magnets has never been assessed after the inserts experience, the code has been used to fill this gap.

Concerning ITER Central Solenoid simulation, the results, in terms of minimum temperature margin ($\Delta T_{\mathrm{marg}}^{\mathrm{min}}$), were much more performing with respect to what was obtained in previous analyses, mainly in view of the updated strain value. Present results show that the coil nominally satisfies the design requirement for both at the first start-up ($\Delta T_{\mathrm{marg}}^{\mathrm{min}} > 1$ K) and after several electro-magnetic cycles ($\Delta T_{\mathrm{marg}}^{\mathrm{min}} > 1.5$ K).

However, if the uncertainties on the coupling time constant are accounted for when the first start-up is considered, it is possible that some conductors do not satisfy the acceptance criteria, but only of few tents of Kelvins. On the other side, after several electro-magnetic cycles, when the coupling time constant is almost halved, the uncertainties slightly affect the operation of the coil.

Concerning the off-normal operation, with a reduction of the mass flow rate in the most critical pancake by 25%, a justified assumption given the simplifying hypothesis in the model (i.e. equal turn length), the temperature margin is additionally eroded of ~0.15 K, while neighbouring pancakes are unaffected.

In conclusion, the first full-current pulse of the Central Solenoid may be the critical one from the $\Delta T_{\mathrm{marg}}{}^{\mathrm{min}}$ point of view, since AC losses will be large, while after several electro-magnetic cycles, the concern on the $\Delta T_{\mathrm{marg}}{}^{\mathrm{min}}$ is more relaxed. This would recommend to go to full power after some charges at lower current, to take advantage of the reduction of the AC losses with cycles. In any case, since the CS modules are undergoing their final testing in the General Atomics facility in San Diego and since electro-magnetic cycles are included in the test plan, no issues are highlighted for the Central Solenoid coil $\Delta T_{\mathrm{marg}}{}^{\mathrm{min}}$ during ITER operation.

As far as the ITER Toroidal Field coil operation is concerned, the results show that all the pancakes satisfy the $\Delta T_{\mathrm{marg}}{}^{\mathrm{min}}$ requirement of 0.7 K during the normal operation and with standard strands for a simulation in nominal, rather than conservative, conditions. In this condition, however, it is advised to implement some kind of mitigation of the radiative and conductive static heat load (enhanced refrigeration of the casing by the case cooling channels or of the gravity support by dedicated channels, i.e. in the location with the higher static heat loads). Then concerning a first case the off-normal operation, if the mass flow rate in the most critical pancake is reduced by 25%, an additional margin erosion smaller than 0.1 K is foreseen, which should not represent a significant danger during the operation.

Concerning the quench propagation, a more severe off-normal operating condition, when the normal zone is initiated in the location if the $\Delta T_{\mathrm{marg}}{}^{\mathrm{min}}$, which is the most likely case, the design criteria on the maximum hot-spot temperature, both in strands (250 K) and jacket (150 K), as well as the maximum pressure (25 MPa) in the winding pack, all the values remain below the prescribed limits. However, the power deposited in the casing after the dump produces a violent pressurization of the circuit of the case cooling channels with the consequent opening of the safety valve followed by the venting of about one fourth of the total He inventory of the circuit in about one minute. In the same way, also the WP loop strongly pressurizes, venting about half of its He inventory in about one minute. Based on these results, the importance of a careful quench lines design is stressed, since about ~51% and ~25%, of the winding pack and case cooling channels circuit, respectively, is expected to be vented during the quench propagation. In perspective, for a successive analyses it would be interesting to assess the hot-spot temperature also in the location where the margin is higher (or the highest), because even if it is less likely that quench will be induced in such a location, it is not excluded for whatever reason.

Finally, concerning the fast discharge, a quench is firstly induced in the shorter side pancakes because of the energy transferred from the radial plates, heated by the eddy losses. In a second time, all other pancakes suffer the initiation of normal zones, induced by the AC losses deposition and again by energy transferred from the radial plates. As observed in the quench propagation simulation, during the discharge, the heat deposition induces a strong pressurization of both cryogenic loops: the winding pack circuit suffers of a stronger pressurization due to additional Joule energy deposited during the quench. Also during the fast discharge, the safety valve of both the winding pack and case cooling channels circuits, therefore the importance of the design of the quench lines is stressed again. Finally, it may be interesting to investigate some solutions to reduce the heat transfer from the radial plates towards the winding pack, for instance by cutting the thermal coupling between the two components, as a mean to reduce the possibility of a quench. If this solution cannot be considered for ITER, it may be worth of investigation for other future fusion machines.

In perspective, since validation is a never-ending exercise, the code will be validated against other kinds of transients and with various design of conductors and magnets. Additionally, the code aims at becoming the reference tool to support the design and research activities of superconducting magnets for other tokamaks, like the DTT and the EU DEMO.

Appendix A

The refrigerator model[6]

Motivation

Traditionally, models of cryogenic refrigerators, e.g. [104] [105] [106], and magnets, e.g. [70] [107] [108], have been developed in separate nuclear fusion scientific communities. The 4C code is part of the magnet models and it can simulate transients in superconducting magnets with the cryogenic loop, only up to the LHe bath, excluding the rest of the cryoplant (i.e. the refrigerator system). Few years ago, a model for a refrigerator started being developed, showing encouraging results already presented at international conferences [109] [110].

Having two separate models certainly simplifies the problem from the computational point of view, but it pays the price of losing some important information during the transients, like feedback effects or the controls acting based on constraints on the other part (not included in the model) of the system, as e.g. the constraint on the $\Delta T^{\max}$ on the coil, as highlighted in the analysis of the CSMC CD in Paragraph 2.5.2. On the other side, to set the BCs, the detailed and isolated magnet model requires the use of experimental data, which may be difficult to be obtained or affected by uncertainties. A coupled tool addresses both issues, allowing the automatic control of the refrigerator model with the feedback and detailed output from the magnet model, and provides to the latter consistent and reliable boundary conditions. Here, the first-of-a-kind coupled coil and refrigerator model is presented

---

[6] Part of the work described in this section was also published in [111].

showing also the comparison between computed and experimental (from the ITER CSMC) results for the 1st stage of the CD.

Refrigerator model

The new coupled model combines the CSMC magnet model [34], with the refrigerator model initially developed as a standalone tool. The operation of most cryogenic refrigerators for SC magnets is based on the Collins cycle. The system is constituted by a two-stage (pre- and inter-cooled) compressor system and the refrigerator cold box (here identified as CB30). Inside the cold box there are inlet/outlet manifolds, several control valves (CVs), a bypass valve (BV), one two- and one three-fluid HXs, a PI temperature and a PID pressure controller at the outlet of CB30 (≡ CSMC inlet), to provide the needed He flow, see Figure 6.1.

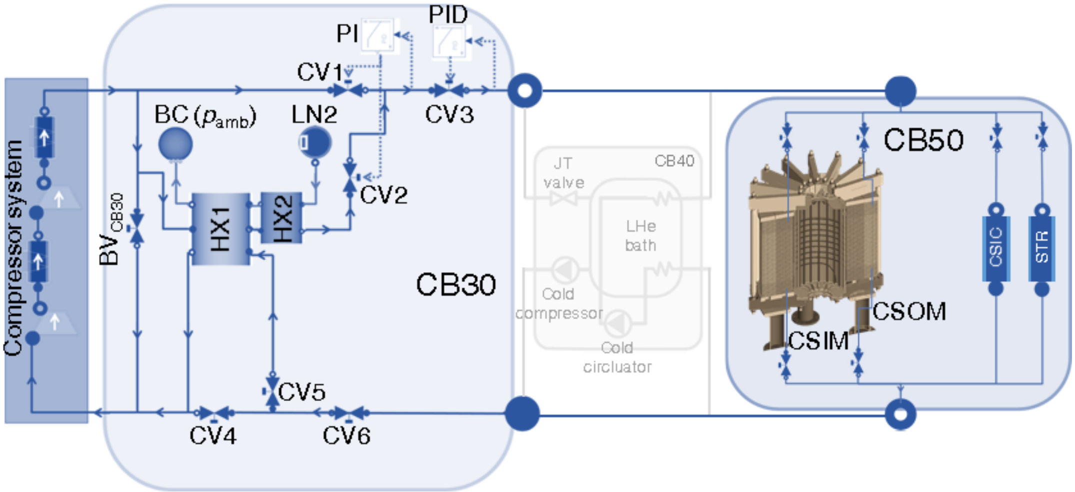

Figure 6.1. Sketch of the coupled model developed, including the refrigerator (CB30) and the CSMC and insert magnets (CB50). The cold-box containing the LHe bath (CB40) is not used during the CD, but reported here for the sake of completeness.

All the known automatic controls have been implemented in the model; however, several manual operations have been performed during the reference CD, which are not included in the model and may be the cause of some discrepancies between computed and experimental results. It means that recorded data of manually controlled valves are included in the model, but unfortunately not all the manual controls have been recorded, so some controls cannot be reproduced.

The interface between the CB30 and the CB50, containing the magnet, is defined by three equations: the first equation is for the pressure ("effort-type" variable

[47]) which must be equal for the two components; the second is the conservation of mass, so the sum of all mass flow rates ("flow-type" variable [47]) must be equal to zero; finally the enthalpy ("stream-type" variable [47]) is transported by advection from the upstream to the downstream CB, depending on the mass flow rate direction.

Results of a cooldown simulation

Here, only the results of the 1st CD stage are presented, since the model of the 2nd stage of the CD, the part including the operation of the two turbines, is currently being developed. One of the most interesting dynamics of the process is the evolution of the opening of the control valves CV1 and CV2. Unfortunately, the operation of these valves is not completely automatic, because several manual interventions were performed ("hand" symbols in Figure 6.2). Nevertheless, the openings of these two valves have been recorded and so it has been possible to prescribe a suitable approximation (envelope) of the actual evolution to be set as input to the model. It must be remarked that, since the HX models are 0D, they do not include the real dynamic response of the system and cannot cope with the fast spikes/oscillations of the valve operation [109].

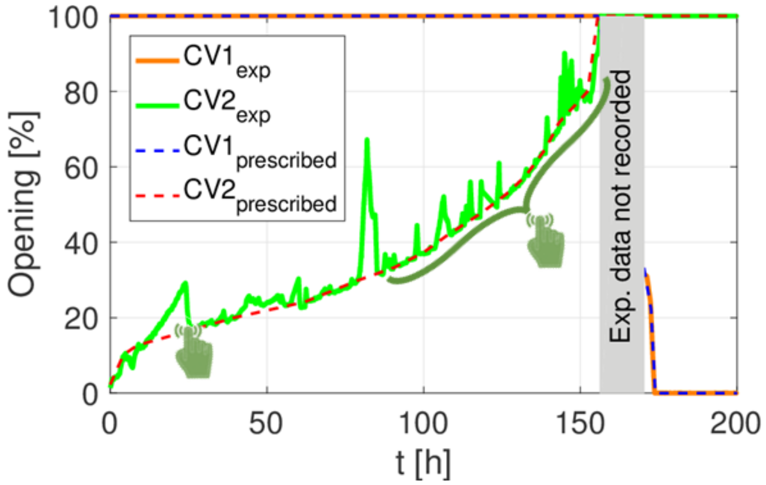

Figure 6.2. Evolution of the openings of control valves CV1 and CV2, resulting from a combination of automatic and manual ("hand" symbol) controls.

The comparison between the computed and experimental inlet and outlet temperature traces at the boundaries of the CSMC is shown in Figure 6.3. The results of the coupled model show a mismatch <5 K on the T_{in} trace, while it is within +/− 8 K for T_{out} (~2%). Since the discrepancy is in the same ball park of what was obtained in [34], the accuracy of the refrigerator model is confirmed. Going a bit more in detail, during the first phase of the transient, the experimental T_{out} rapidly decreases of few Kelvins, while the computed trace remains flat up to ~30 h, corresponding to a time interval of the order of the heat transit time in the whole magnet. The anticipated temperature decrease observed in experimental data may be due to the conductive/radiative heat transfer with the cryostat, not included in the model: the lack of this additional cooling path turns into a T_{out} overestimation in the first ~50 h.

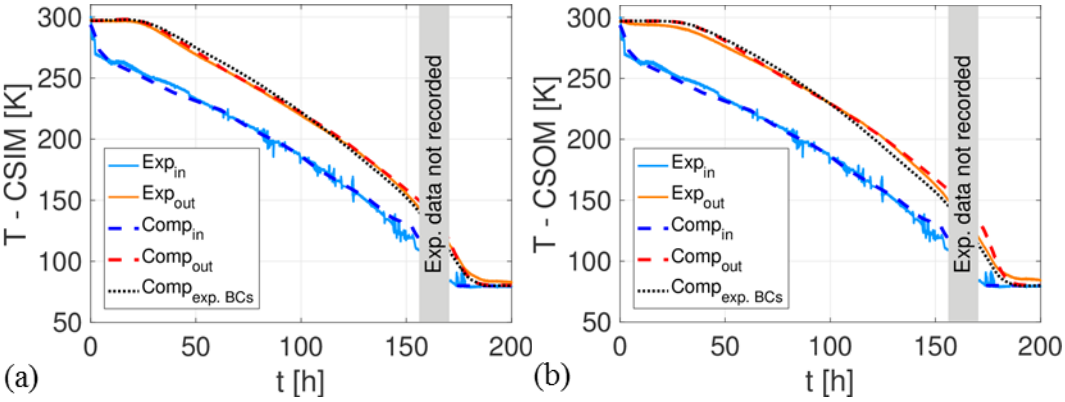

Figure 6.3. Experimental (solid, inlet: light blue, outlet: orange) and computed (dashed, inlet: blue, outlet: red) temperature evolution in the (a) CSIM and (b) CSOM. The outlet temperature from [34] is also reported (dotted black).

The comparison between computed and experimental mass flow rate at the boundary of the CSMC shows a good agreement (error < ~10%) with a slight overestimation of few g/s for $t < 70$ h, see Figure 6.4. After that time, to enhance cooling, the CSOM outlet valve opening, unfortunately unrecorded, is increased by manual intervention to improve the cooling. This is the reason why the discrepancy between computed and experimental data increases for $t > 70$ h both for the temperature traces in Figure 6.3b and the mass flow rate in Figure 6.4b.

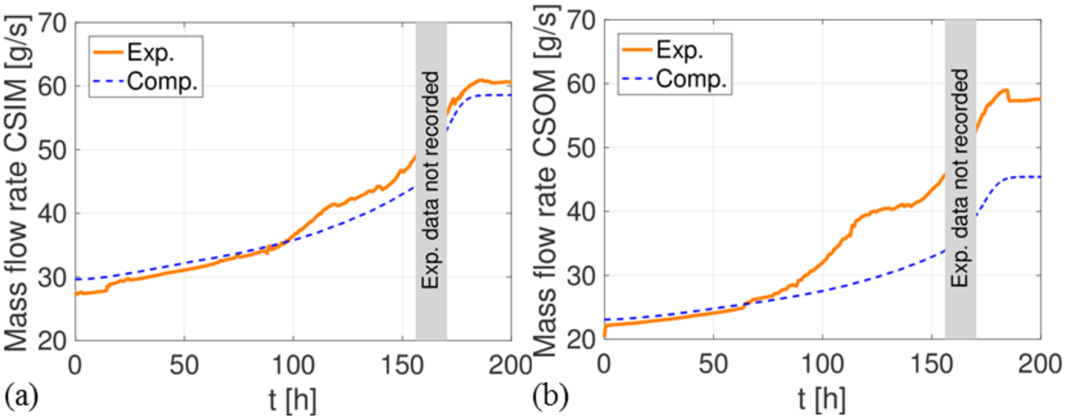

Figure 6.4. Comparison between experimental (solid orange) and computed (thin dashed blue) mass flow rate in the (a) CSIM and (b) CSOM.

The comparison of the $\Delta T^{\max}$ across both CSMC modules, see Figure 6.5, shows that even if the agreement between simulation and experiment is good in the central part of the transient ($50 < t < 150$ h), some discrepancy are clearly visible at $t < 50$ h and $t > 150$ h. The first one is explained by the neglected cooling path toward the cryostat, while the second is linked to the discrepancy on the mass flow rate and the effect of enhanced cooling. Finally, in the last ~20 h of the transient, a significant temperature difference is observed between the simulation and the experiment, possibly due to the radiative/conductive heat load from external environment to the CSMC.

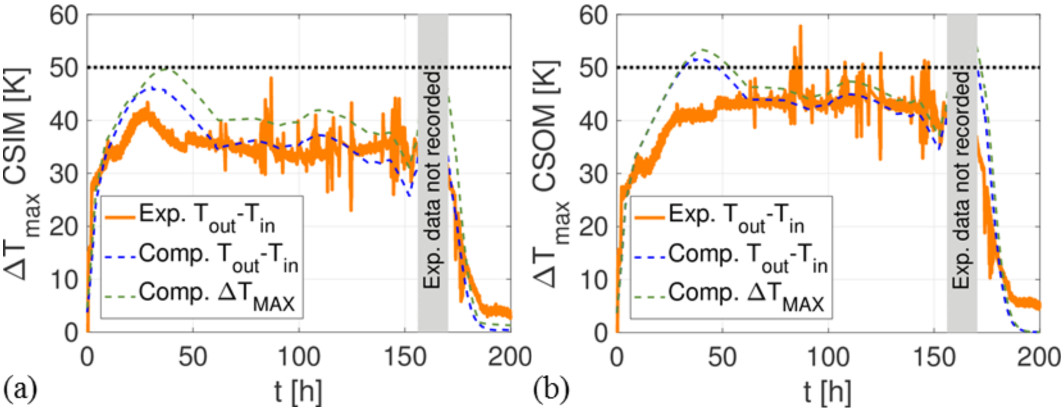

Figure 6.5. Maximum temperature difference across the coil compared between experimental (orange) and computed (dashed blue) results in the (a) CSIM and (b) CSOM. The computed maximum absolute temperature difference in the coil is also reported (dashed green).

Final considerations

A simplified refrigerator model has been developed inside the 4C code and coupled to the existing CSMC (and CSI) magnet model. The results for the CSMC CD from 300 K to 80 K showed a good accuracy of the tool, despite some of the approximations introduced (e.g. 0D HX).

In perspective, the model for the 2nd stage of the CD will be completed and validated against experimental data. Then, the model will be ready for successive applications, like the development of automatic controls for modern tokamaks, including the CD, but also the design of suitable smoothing strategies of the heat load coming from the magnets and going to the refrigerator, during the operation of the machine.

Appendix B

Optimization of the CSMC CD strategy

Objectives

The two main objectives of the exercise are the reduction of the total time required by the process, satisfying the constraint on the ΔT^{max}, but also the reduction of the radial temperature gradient on the CSMC cross section by changing the mass flow distribution among CSIM and CSOM conductors. Here, the optimization exercise focuses only on Stage I of the CD, because of the different operation mode of the refrigerator.

Methodology and results

Concerning the BCs in the optimization exercise, the experimental inlet mass flow rate and the outlet pressure have been expressed as function of the measured T_{in}, to keep a sort of "relative" correspondence to the nominal CD evolution. This combination is maintained for each optimization strategy proposed, which beside the fast temperature decrease of ~15 K/h (for ~2 h) after 25 h from the beginning of the transient, prescribes a T_{in} with a maximum rate of −1 or −2 K/h, including the control on the ΔT^{max} (if the constraint is satisfied, T_{in} is decreased, otherwise it is kept constant). The simulation ends when T_{in} reaches 80 K.

To measure the mass flow rate unbalance among the layers, a dimensionless parameter is used:

$$\Gamma = \frac{(dm/dt)_{L18}}{(dm/dt)_{L1}} \tag{39}$$

where dm/dt_{L18} and dm/dt_{L1} correspond to the mass flow rate in layer 18 and layer 1, respectively. Without changing the total CSMC mass flow rate evolution, the parameter Γ is varied parametrically, see Figure 7.1a, and increasing values of Γ correspond to an increasing mass flow rate unbalance, advantageous for the outer module conductors. The nominal value ($\Gamma = 1$) hides the above-mentioned mass flow unbalance for layer from 5A to 8B of the nominal case.

Using a value of Γ between 1.5 and 2, it is possible to reduce the cooldown time of more than 40 h (~20%), see Figure 7.1b where the reduction of the CD time is strictly related to the reduction of the temperature difference among the layers, see Figure 7.2. As outcome of the parametric study, the optimized CD is obtained with $\Gamma \sim 1.72$, with the ΔT^{max} constraint always satisfied, see Figure 7.3. The outlet temperature of both CSMC modules is shown in Figure 7.4, showing the ~20% reduction of the required CD time. To implement the optimization strategy proposed, it would be necessary to install control valves for the conductors of each layer; however, since the CD time reduction is only ~20%, such effort is justified only if relatively many CD must be performed within a given time, which is not the case for a test facility as the CSMC.

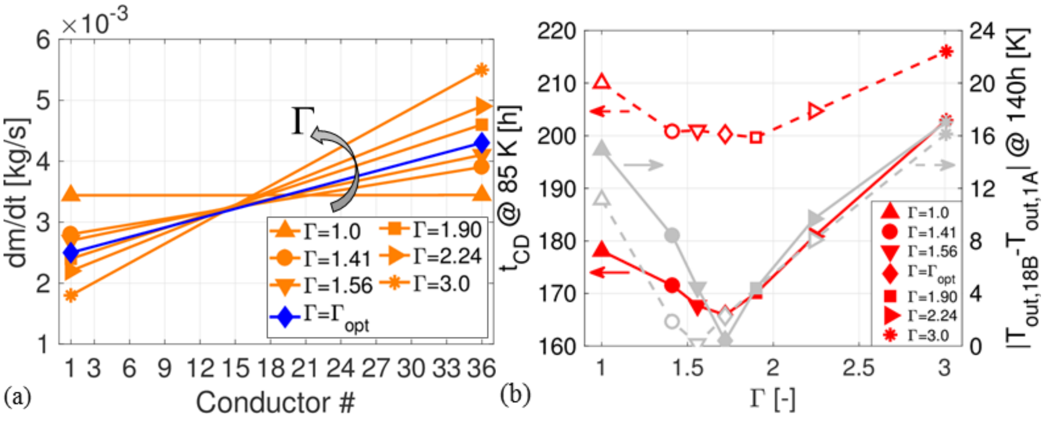

Figure 7.1. (a) Mass flow rate distribution among the CSMC conductors (1A → conductor #1, 18B → conductor #36) adopted in the optimization exercise. The computed optimized CD (Γ ~1.72) corresponds to the blue line. (b) CD duration from 300 K to 85 K (corresponding to the T_{out} during the T_{in} plateau at 80 K before the beginning of the second stage of the CD, left axis) and temperature difference at the outlet of conductor 1A and 18B (right axis) at ~140 h as a function of Γ, for different CD rates (−1 K/h dashed line with empty symbols, and −2 K/h solid lines with symbols).

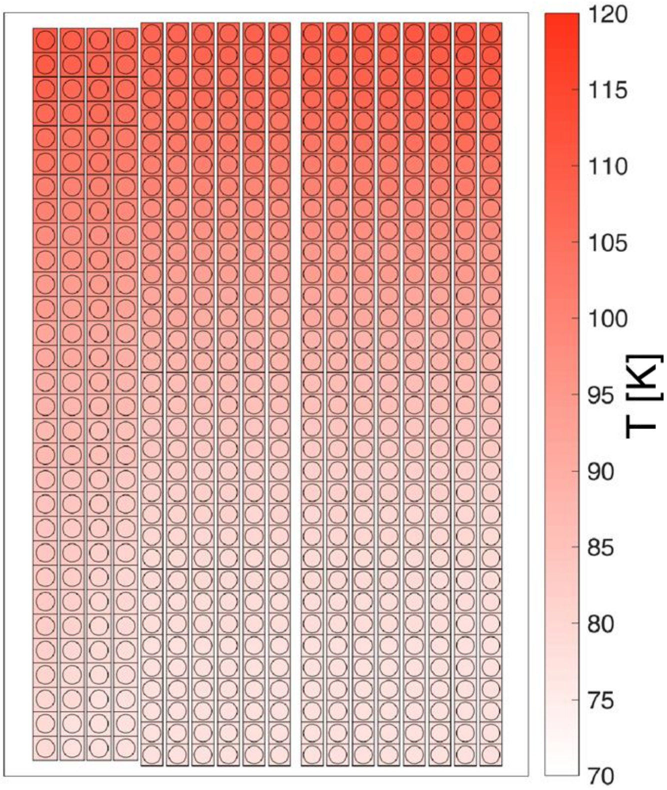

Figure 7.2. 2D temperature map on the CSMC cross section at ~140 h for the optimized CD strategy. Note that the radial temperature gradient is smaller with respect to Figure 2.13.

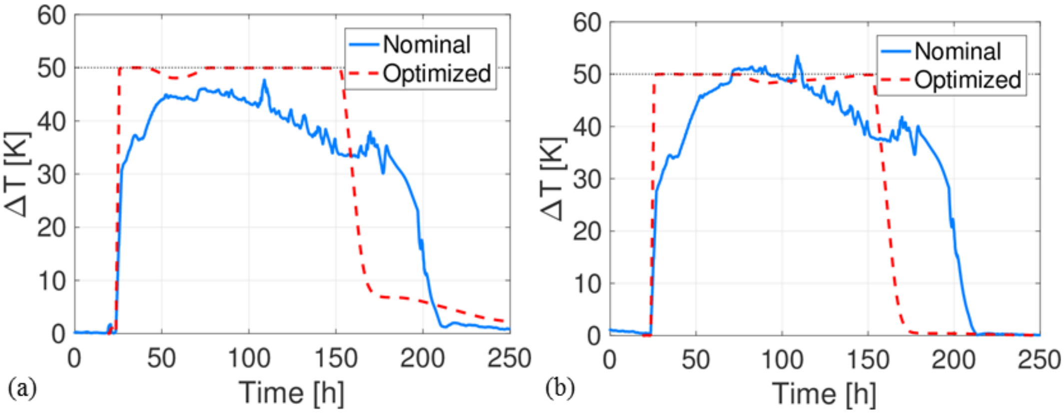

Figure 7.3. Maximum temperature difference in (a) CSIM and (b) CSOM for the experimental (solid light blue) and the computed optimized results (dashed red).

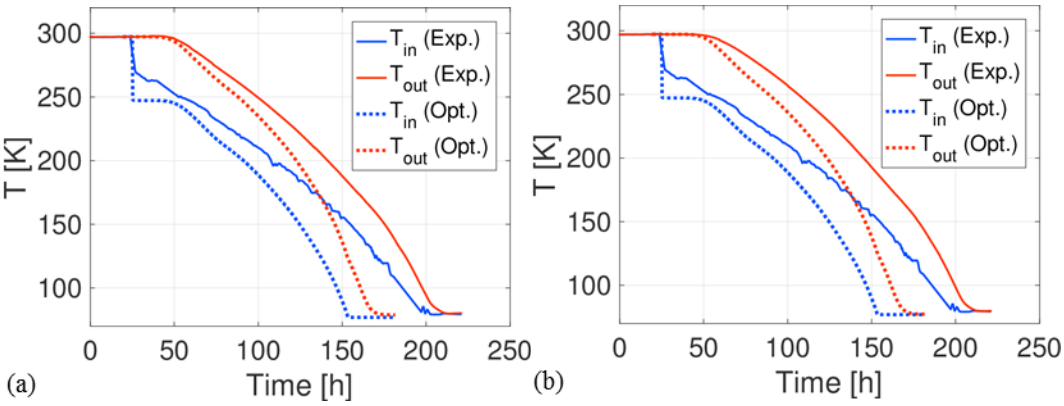

Figure 7.4. Comparison between experimental (solid line) and computed optimized (dotted line) results at the inlet (blue) and outlet (red) of the (a) CSIM and (b) CSOM.

References

[1] C. Pirlogea and C. Cicea, "Econometric perspective of the energy consumption and economic growth relation in European Union," *Renewable and Sustainable Energy Reviews,* vol. 16, no. 8, pp. 5718-5726, Oct. 2012.

[2] World Energy Council, "World Energy Scenarios 2016 - The Grand Transition," October 2016. [Online]. Available: https://www.worldenergy.org/wp-content/uploads/2016/10/World-Energy-Scenarios-2016_Full-Report.pdf. [Accessed 31 December 2018].

[3] J. Freidberg, Plasma Physics and Fusion Energy, Cambridge, MA (USA): Cambridge University Press, 2007.

[4] Georgia State University, Department of Physics and Astronomy, "HyperPhysics," [Online]. Available: http://hyperphysics.phy-astr.gsu.edu/hbase/NucEne/nucbin.html. [Accessed 15 November 2018].

[5] ITER IO, "ITER MAG 2 - Hotter than the Sun," February 2014. [Online]. Available: https://www.iter.org/mag/2/18. [Accessed 15 November 2018].

[6] G. McCracken and P. Stott, Fusion: The Energy of the Universe, Cambridge, MA (USA): Academic Press, 2005.

[7] B. B. Kadomtsev, F. S. Troyon, M. L. Watkins, P. H. Rutherford, M. Yoshikawa and V. S. Mukhovatov, "Tokamaks," *Nucl. Fusion,* vol. 30, no. 9, pp. 1675-1694, 1990.

[8] Commissariat à l'énergie atomique et aux énergies alternatives (CEA), "CEA participation in JET," [Online]. Available: http://www-fusion-magnetique.cea.fr/gb/cea/jet/jet.htm. [Accessed 5 November 2018].

[9] EUROFusion, "JET: EUROfusion's flagship device," [Online]. Available: https://www.euro-fusion.org/devices/jet/. [Accessed 15 November 2018].

[10] Culham Center for Fusion Energy (CCFE), "How fusion works," [Online]. Available: http://www.ccfe.ac.uk/How_fusion_works.aspx. [Accessed 15 November 2018].

[11] ITER IO, "What is ITER?," [Online]. Available: https://www.iter.org/proj/inafewlines. [Accessed 15 November 2018].

[12] ITER IO, "ITER Newsline - It's now official: First Plasma in December 2025," 20 June 2016. [Online]. Available: https://www.iter.org/newsline/-/2482. [Accessed 15 November 2018].

[13] ITER IO, "The largest tokamak in the world," 15 January 2013. [Online]. Available: https://www.iter.org/album/Media/7%20-%20Technical. [Accessed 15 November 2018].

[14] N. Mitchell, D. Bessette, R. Gallix, J. Knaster, P. Libeyre, C. Sborchia and F. Simon, "The ITER Magnet System," *IEEE Trans. Appl. Supercond.,* vol. 18, no. 2, Jun. 2008.

[15] R. Maekawa, S. Takami, A. Iwamoto, H. S. Chang, A. Forgeas, M. Chalifour and L. Serio, "Process analyses of ITER Toroidal Field Structure cooling scheme," *Cryogenics,* vol. 63, pp. 220-230, 2014.

[16] A. Devred, I. Backbier, D. Bessette, G. Bevillard, M. Gardner, C. Jong, F. Lillaz, N. Mitchell, G. Romano and A. Vostner, "Challenges and status of ITER conductor production," *Supercond. Sci. Technol.,* vol. 27, no. 4, Apr. 2014.

[17] C. J. Heyne, D. T. Hackworth, S. K. Singh, J. L. Young and P. A. Sanger, "Westinghouse design of a forced flow Nb3Sn test coil for the large coil program," *Proc. of Symp. on Engineering Problems of Fusion Research,* pp. 1148-1153, 1979.

[18] P. Bruzzone, "Superconductivity and fusion energy - the inseparable companions," *Supercond. Sci. Technol.,* vol. 28, no. 2, Feb. 2015.

[19] K. Risse, T. Rummel, L. Wegener, R. Holzthum, N. Jaksic, K. F. and J. Sapper, "Fabrication of the superconducting coils for Wendelstein 7-X," *Fus. Eng. Des.,* Vols. 66-68, pp. 965-969, 2003.

[20] C. Sborchia, A. Bonito Oliva, T. Boutboul, K. Chan, A. Devred, S. Egorov, K. Kim, N. Koizumi, S. Lelekhov, P. Libeyre, B. S. Lim, N. Martovetsky, H. Nakajima, N. Mitchell, K. Okuno, V. Pantsyrny, W. Reiersen, I. Rodin, F. Savary, A. Vostner and Y. Wu, "The ITER magnet systems: progress on construction," *Nucl. Fusion,* vol. 54, 2014.

[21] R. Bonifetto, P. Bruzzone, V. Corato, L. Muzzi, L. Savoldi, B. Stepanov, R. Zanino and A. Zappatore, "Thermal–Hydraulic Test and Analysis of the ENEA TF Conductor Sample for the EU DEMO Fusion Reactor," *IEEE Trans. Appl. Supercond.,* vol. 28, no. 4, Jun. 2018.

[22] M. Thinkham, Introduction to Supeconductivity, New York: McGraw-Hill, 1975.

[23] M. N. Wilson, Superconducting Magnets, Oxford, U.K.: Clarendon, 1983.

[24] Y. Iwasa, Case Studies in Superconducting Magnets Design and Operation, Springer, 2009.

[25] National High Magnetic Field Lab, "Nb3Sn Image Gallery," [Online]. Available: https://nationalmaglab.org/magnet-development/applied-superconductivity-center/asc-image-gallery/nb3sn-image-gallery. [Accessed 9 November 2018].

[26] FermiLab, "Applied Physics and Superconducting Technology Division," [Online]. Available: http://td.fnal.gov/magnet-capabilities/. [Accessed 15 November 2018].

[27] F. Romanelli et al., "Fusion Electricity. A Roadmap to the Realisation of Fusion Energy," November 2012. [Online]. Available: https://www.euro-fusion.org/fileadmin/user_upload/Archive/wp-content/uploads/2013/01/JG12.356-web.pdf. [Accessed 9 November 2018].

[28] T. Donné and W. Morris, "European Research Roadmap to the Realisation of Fusion Energy," September 2018. [Online]. Available: https://www.euro-fusion.org/fileadmin/user_upload/EUROfusion/Documents/2018_Research_roadmap_long_version_01.pdf. [Accessed 2 January 2019].

[29] A. Pizzuto et al., "DTT - Divertor Tokamak Test Facility Project Proposal," July 2015. [Online]. Available: https://www.dtt-project.enea.it/downloads/DTT_ProjectProposal_July2015.pdf. [Accessed 5 February 2019].

[30] L. Savoldi Richard, F. Casella, B. Fiori and R. Zanino, "The 4C Code for the Cryogenic Circuit Conductor and Coil modeling in ITER," *Cryogenics,* vol. 50, pp. 167-176, 2010.

[31] R. Zanino and L. Savoldi Richard, "Multiscale Approach and Role of Validation in the Thermal-Hydraulic Modeling of the ITER Superconducting Magnets," *IEEE Trans. Appl. Supercond.,* vol. 23, no. 3, Jun. 2013.

[32] N. Martovetsky, T. Isono, D. Bessette, Y. Takahashi, Y. Nunoya, Y. Nabara, H. Ozeki, K. Kawano, T. Saito, T. Suwa, K. Okuno, A. Devred, F. Gauthier, N. Mitchell, R. Zanino, L. Savoldi, R. Bonifetto, M. Breschi, D. Ciazynski, W. Reiersen, A. Smirnov, A. Khodak, P. Bruzzone, I. Rodin, A. Tronza, A. Torre, S. Nicollet, L. Zani, A. Louzguiti and J. L. Duchateau, "ITER Central Solenoid Insert Test Results," *IEEE Trans. Appl. Supercond.,* vol. 26, no. 4, Jun. 2016.

[33] H. Tsuji, K. Okuno, R. Thome, E. Salpietro, S. Egorov et al., "Progress of the ITER central solenoid model coil programme," *Nucl. Fusion,* vol. 41, no. 5, 2001.

[34] R. Bonifetto, A. Brighenti, T. Isono, N. Martovetsky, K. Kawano, L. Savoldi and R. Zanino, "Analysis of the cooldown of the ITER central solenoid model coil and insert coil," *Supercond. Sci. Technol.,* vol. 30, no. 1, Jan. 2017.

[35] M. Breschi, M. Bianchi, R. Bonifetto, S. Carli, A. Devred, N. Martovetsky, P. L. Ribani, L. Savoldi, I. Takaaki and R. Zanino, "Analysis of AC losses in the ITER Central Solenoid Insert (CSI) Coil," *IEEE Trans. Appl. Supercond.,* vol. 27, no. 4, Jun. 2017.

[36] R. Bonifetto, M. Bianchi, M. Breschi, A. Brighenti, N. Martovetsky, L. Savoldi and R. Zanino, "Modeling the ITER CS AC losses based on CS insert analysis," *submitted to IEEE Trans. Appl. Supercond..*

[37] R. Bonifetto, T. Isono, N. Martovetsky, L. Savoldi and R. Zanino, "Analysis of quench propagation in the ITER Central Solenoid Insert (CSI) Coil," *IEEE Trans. Appl. Supercond.,* vol. 27, no. 4, Jun. 2017.

[38] N. Martovetsky, T. Isono, A. Devred, Y. Nabara, R. Zanino, L. Savoldi, R. Bonifetto, P. Bruzzone, M. Breschi and L. Zani, "Characterization of the ITER CS conductor and projection to the ITER CS performance," *Fus. Eng. Des.,* vol. 124, 2017.

[39] R. Bonifetto, T. Isono, N. Martovetsky, L. Savoldi and R. Zanino, "Analysis of the DC performance of the ITER CSI coil using the 4C code," *Fus. Eng. Des.,* vol. 124, 2017.

[40] H. Ozeki, T. Isono, Y. Uno, K. Kawano, T. Kawasaki, N. Ebisawa, K. Okuno, K. Kido, T. Semba, Y. Suzuki, T. Ichimura, S. Inoue, Y. Kuchiishi, H. Hasegawa, A. Smirnov and N. Martovetsky, "Manufacture and Quality Control of Insert Coil With Real ITER TF Conductor," *IEEE Trans. Appl. Supercond.,* vol. 26, no. 4, Jun. 2016.

[41] H. Ozeki, T. Isono, K. Kawano, T. Suwa, Y. Takahashi, N. Koizumi, T. Hemmi, N. Martovetsky, M. Breschi, D. Bessette, F. Gauthier and A. Devred, "Tcs Measurements Result of ITER Toroidal Field Insert Coil Tested in 2016," *IEEE Trans. Appl. Supercond.,* vol. 28, no. 3, Apr. 2018.

[42] R. Zanino, R. Bonifetto, A. Brighenti, T. Isono, H. Ozeki and L. Savoldi, "Prediction, experimental results and analysis of the ITER TF insert coil quench propagation tests, using the 4C code," *Supercond. Sci. Technol.,* vol. 31, no. 3, Mar. 2018.

[43] NEMO Group, "4C," [Online]. Available: http://www.nemo.polito.it/research/software/4c. [Accessed 29 November 2018].

[44] R. Zanino, S. De Palo and L. Bottura, "A two fluid-code for the thermo-hydraulic transient analysis of CICC superconducting magnets," *J. Fusion Energy,* vol. 14, pp. 25-40, 1995.

[45] R. Zanino, L. Bottura, L. Savoldi and C. Rosso, "Mithrandir + : a two-channel model for thermal-hydraulic analysis of cable-in-conduit super-conductors cooled with helium I or II," *Cryogenics,* vol. 38, pp. 525-531, 1998.

[46] FreeFem++. [Online]. Available: https://freefem.org/. [Accessed 29 November 2018].

[47] S. Mattson, H. Elmqvist and M. Otter, "Physical system modeling with Modelica," *Control Engineering Practice,* vol. 6, pp. 501-510, 1998.

[48] P. Fritzson, Principles of object-oriented modeling and simulation with Modelica 2.1, Wiley, 2003.

[49] Dassault Systèmes®, "Dymola," 2018. [Online]. Available: https://www.3ds.com/products-services/catia/products/dymola/. [Accessed 29 November 2018].

[50] F. Casella and A. Leva, "Modelling of thermo-hydraulic power generation processes," *Math. Comput. Model Dyn.,* vol. 12, pp. 19-33, 2006.

[51] F. Casella and A. Leva, "Modelica Open Library for Power Plant Simulation: Design and Experimental," in *Proceedings of the 3rd International Modelica Conference*, Linkoping, Sweden, 2003.

[52] R. Zanino, S. Giors and L. Richard Savoldi, "CFD modeling of ITER cable-in-conduit superconductors. Part III: Correlation for the central channel friction factor," in *Proc. 21st Int. Cryogenic Eng. Conf.*, Prague (Czech Republic), 2006.

[53] H. Katheder, "Optimum thermohydraulic operation regime for cable in conduit superconductors (CICS)," *Cryogenics,* vol. 34, pp. 595-598, 1994.

[54] T. Isono, *Personal communication,* February 15, 2016.

[55] R. Bonifetto, A. Kholia, B. Renard, K. Risse, L. Savoldi Richard and R. Zanino, "Modeling the W7-X superconducting coil cool-down using the 4C code," *Fus. Eng. Des.,* vol. 86, pp. 1549-1552, 2011.

[56] R. Zanino, N. Mitchell and L. Savoldi Richard, "Analysis and interpretation of the full set (2000-2002) of Tcs tests in conductor 1A of the ITER central solenoid model coil," *Cryogenics,* vol. 43, pp. 179-197, 2003.

[57] A. Brighenti, R. Bonifetto, T. Isono, K. Kawano, G. Russo, L. Savoldi and R. Zanino, "Overview of the hydraulic characteristics of the ITER Central Solenoid Model Coil conductors after 15 years of test campaigns," *IOP Conf. Ser.: Mater. Sci. Eng.,* vol. 278, 2017.

[58] B. Turck and L. Zani, "A macroscopic model for coupling current losses in cables made of multistages of superconducting strands and its experimental validation," *Cryogenics,* vol. 50, no. 8, pp. 443-449, 2010.

[59] A. Louzguiti, L. Zani, D. Ciazynski, B. Turck and F. Topin, "Development of an analytical-oriented extensive model for AC coupling losses in multilayer superconducting composites," *IEEE Trans. Appl. Supercond.,* vol. 26, no. 3, Apr. 2016.

[60] D. Bessette and F. Gauthier, *Private communication,* 2015.

[61] ITER IO, "ITER design description document (DDD) 11-7 magnets, conductor," ITER_D_2NBKXY v1.2, 2009.

[62] M. Ciotti, A. Nijhuis, P. L. Ribani, L. Savoldi Richard and R. Zanino, "Thelma code electromagnetic model of ITER superconducting cable application to the ENEA stability experiment," *Supercond. Sci. Technol.,* vol. 19, no. 10, pp. 987-997, Oct. 2006.

[63] M. Breschi, A. Macchiagodena, P. L. Ribani, F. Bellina, F. Stacchi, S. Izquierdo Bermudez and H. Bajas, "Experimental and Numerical

Investigation on Losses in Electrodynamic Transients in a Nb3Sn Prototype Racetrack Coil," *IEEE Trans. Appl. Supercond.,* vol. 28, no. 3, Apr. 2018.

[64] M. Breschi, L. Cavallucci, P. L. Ribani, C. Calzolaio and S. Sanfilippo, "Analysis of losses in superconducting magnets based on the Nb3Sn Rutherford cable configuration for future gantries," *Supercond. Sci. Technol.,* vol. 31, no. 1, Jan. 2018.

[65] M. Breschi, M. Bianchi, A. C. Ricchiuto, P. L. Ribani and A. Devred, "Analysis of AC Losses in a CS Conductor Sample for the ITER Project," *IEEE Trans. Appl. Supercond.,* vol. 28, no. 3, Apr. 2018.

[66] D. Bessette, "Assessment of the Effective strain vs IxB of the TFJA4 Sample Hitachi leg," ITER IDM 33VBNJ v1.2, 2010.

[67] L. Bottura and B. Bordini, "Jc (B, T, ε) Parameterization for the ITER Nb3Sn Production," *IEEE Trans. Appl. Supercond.,* vol. 19, no. 3, pp. 1521-1524, Jun. 2009.

[68] L. Savoldi Richard, R. Bonifetto, S. Carli, F. Froio, A. Foussat and R. Zanino, "Artificial Neural Network (ANN) modeling of the pulsed heat load during ITER CS magnet operation," *Cryogenics,* vol. 63, pp. 231-240, 2014.

[69] V. I. Tronza, S. A. Lelekhov, V. M. Patrikeev, S. A. Svertnev, D. S. Kaverin, M. V. Kochetov and V. S. Vysotsky, "Investigation of ITER TF Conductor Hydraulic Resistance," *IEEE Trans. Appl. Supercond.,* vol. 25, no. 3, Jun. 2015.

[70] N. Peng, L. Q. Liu, L. Serio, L. Y. Xiong and L. Zhang, "Thermo-hydraulic analysis of the gradual cool-down to 80 K of the ITER toroidal field coil," *Cryogenics,* vol. 49, pp. 402-406, 2009.

[71] L. Savoldi Richard, R. Bonifetto, U. Bottero, A. Foussat, N. Mitchell, K. Seo and R. Zanino, "Analysis of the Effects of the Nuclear Heat Load on the ITER TF Magnets Temperature Margin," *IEEE Trans. Appl. Supercond.,* vol. 24, no. 3, Jun. 2014.

[72] N. Mitchell, "ITER Organization, on behalf of the ITER, Domestic Agency and Supplier Magnet Teams," in *presented at the EUCAS Conference*, Geneva (Switzerland), 2017.

[73] N. Martovetsky, *Private communications,* 2017.

[74] A. Anghel, "QUELL experiment: analysis and interpretation of the quench," *Cryogenics,* vol. 38, pp. 459-466, 1998.

[75] R. Zanino, L. Bottura and C. Marinucci, "A comparison between 1- and 2-fluid simulations of the QUELL conductor," *IEEE Trans. Appl. Supercond.,* vol. 7, no. 2, Jun. 1997.

[76] L. Savoldi Richard, E. Salpietro and R. Zanino, "Inductively driven transients in the CS Insert Coil (II): Quench tests and analysis," *Adv. Cryogenic Eng.,* vol. 47, pp. 423-430, 2002.

[77] Y. Takahashi, K. Yoshida, Y. Nabara, M. Edaya and N. Mitchell, "Simulation of Quench Tests of the Central Solenoid Insert Coil in the ITER Central Solenoid Model Coil," *IEEE Trans. Appl. Supercond.,* vol. 16, no. 2, Jun. 2006.

[78] T. Inaguchi, M. Hasegawa, N. Koizumi, T. Isono, K. Hamada, M. Sugimoto and Y. Takahashi, "Quench analysis of an ITER 13T-40kA Nb3Sn coil (CS insert)," *Cryogenics,* vol. 44, no. 2, pp. 121-130, 2004.

[79] L. Savoldi Richard, A. Portone and R. Zanino, "Tests and Analysis of Quench Propagation in the ITER Toroidal Field Conductor Insert," *IEEE Trans. Appl. Supercond.,* vol. 13, no. 2, Jun. 2003.

[80] R. Zanino, R. Bonifetto and L. Savoldi Richard, "Analysis of quench propagation in the ITER poloidal field conductor insert (PFCI)," *IEEE Trans. Appl. Supercond.,* vol. 20, no. 3, Jun. 2010.

[81] A. E. Khodak, N. Martovetsky, A. V. Smirnov and P. H. Titus, "Analysis of TF insert coil," *IEEE Trans. Appl. Supercond.,* vol. 24, no. 3, Jun. 2014.

[82] J. W. Lue, L. Dresner, S. W. Schwenterly, C. T. Wilson and M. S. Lubell, "Investigating thermal hydraulic quenchback in a cable-in-conduit superconductor," *IEEE Trans. Appl. Supercond.,* vol. 3, no. 1, Mar. 1993.

[83] E. S. Drexler, R. P. Reed and N. J. Simon, "Properties of copper and copper alloys at cryogenic temperatures," in *NIST Monograph 177*, Washington, DC, Rep. DC 20402-9325, U.S. Government Printing Office, Feb. 1992.

[84] D. Bessette, *Private communication,* 2017.

[85] M. Bagnasco, D. Bessette, L. Bottura, C. Marinucci and C. Rosso, "Progress in the Integrated Simulation of Thermal-Hydraulic Operation of the ITER Magnet System," *IEEE Trans. Appl. Supercond.,* vol. 20, no. 3, Jun. 2010.

[86] L. Savoldi, R. Bonifetto, A. Brighenti, V. Corato, L. Muzzi, S. Turtù, R. Zanino and A. Zappatore, "Quench propagation in a TF coil of the EU DEMO," *Fusion Sci. Technol.,* vol. 72, no. 3, pp. 439-448, 2017.

[87] L. Savoldi, L. Bottura and R. Zanino, "Simulation of thermalhydraulic transients in two-channel CICC with self-consistent boundary conditions," *Adv. Cryog. Eng,* vol. 45, pp. 697-704, 2000.

[88] A. Devred, D. Bessette, P. Bruzzone, K. Hamada, T. Isono, N. Martovetsky, N. Mitchell, Y. Nunova, K. Okuno, I. Pong, W. Reiersen, C. M. Rey, B. Stepanov, Y. Takahashi and A. Vostner, "Status of the Conductor Qualification for the ITER Central Solenoid," *IEEE Trans. Appl. Supercond.,* vol. 23, no. 3, Jun. 2013.

[89] ITER IO, "ITER Newsline 122 - Packing a punch," 12 March 2010. [Online]. Available: https://www.iter.org/newsline/122/182. [Accessed 9 November 2018].

[90] K. Seo, *Personal communication,* January 28, 2014.

[91] K. Seo, *Personal communication,* January 29, 2014.

[92] G. Rolando, A. Devred and A. Nijhuis, "Temperature and current margin of ITER central solenoid conductor designs during a 15 MA plasma scenario," *Supercond. Sci. Technol.,* vol. 27, no. 2, Dec. 2014.

[93] C. Sborchia, Y. Fu, R. Gallix, C. Jong, J. Knaster and N. Mitchell, "Design and Specifications of the ITER TF Coils," *IEEE Trans. Appl. Supercond.,* vol. 18, no. 2, Jun. 2008.

[94] Fusion For Energy (F4E), "Winding the final conductor for Europe's ITER Toroidal coils," 9 June 2017. [Online]. Available: http://fusionforenergy.europa.eu/mediacorner/newsview.aspx?content=1135. [Accessed 13 November 2018].

[95] Fusion For Energy (F4E), "Europe has manufactured the most high-tech magnet in history!," 19 May 2017. [Online]. Available: http://fusionforenergy.europa.eu/mediacorner/newsview.aspx?content=1128. [Accessed 13 November 2018].

[96] Fusion For Energy (F4E), "Operation Insertion accomplished," 12 December 2018. [Online]. Available: https://f4e.europa.eu/mediacorner/newsview.aspx?content=1296. [Accessed 21 January 2019].

[97] ITER IO, "ITER Newsline 70 - Coping with extreme stress," 23 Febraury 2009. [Online]. Available: https://www.iter.org/newsline/70/264. [Accessed 13 November 2018].

[98] L. Savoldi Richard, R. Bonifetto, A. Foussat, N. Mitchell, K. Seo and R. Zanino, "Mitigation of the Temperature Margin Reduction due to the Nuclear Radiation on the ITER TF coils," *IEEE Trans. Appl. Supercond.,* vol. 23, no. 3, Jun. 2013.

[99] R. Zanino, D. Bessette and L. Savoldi Richard, "Quench analysis of an ITER TF coil," *Fus. Eng. Des.,* vol. 85, pp. 752-760, 2010.

[100] L. Savoldi Richard, D. Bessette, R. Bonifetto and R. Zanino, "Parametric Analysis of the ITER TF Fast Discharge Using the 4C Code," *IEEE Trans. Appl. Supercond.,* vol. 22, no. 3, Jun. 2012.

[101] R. Bonifetto, F. Buonora, L. Savoldi Richard and R. Zanino, "4C Code Simulation and Benchmark of ITER TF Magnet Cool-Down From 300 K to 80 K," *IEEE Trans. Appl. Supercond.,* vol. 22, no. 3, Jun. 2012.

[102] A. Foussat, *Private communications,* July 16, 2012.

[103] K. Seo, *Personal communication,* December 24, 2012.

[104] R. Maekawa, K. Ooba, M. Nobutoki and T. Mito, "Dynamic simulation of the helium refrigerator/liquefier for LHD," *Cryogenics,* vol. 45, pp. 199-211, 2005.

[105] C. Deschildre, A. Barraud, P. Bonnay, P. Briend, A. Girard, J. M. Poncet, P. Roussel and S. E. Sequeira, "Dynamic simulation of an helium refrigerator," *Adv. Cryog. Eng.,* vol. 53, pp. 475-482, 2008.

[106] B. Bradu, P. Gayet and S. Niculescu, "A process and control simulator for large scale cryogenic plants," *Cryogenic Engineering Practice,* vol. 17, pp. 1388-1397, 2009.

[107] http://www.alphysica.com. [Online].

[108] https://supermagnet.sourceforge.io. [Online].

[109] R. Bonifetto, K. Kawano, L. Savoldi, A. Tancredi and R. Zanino, "Development and test of a Modelica dynamic model of the ITER CSMC He refrigerator," in *presented at Cryogenic Engineering Conference*, Madison (USA), 2017.

[110] R. Bonifetto, L. Savoldi, A. Tancredi and R. Zanino, "Development and test of a dynamic model of the ITER CSMC He refrigerator Part II: from 80 to 4 K," in *presented at CHATS on Applied Superconductivity*, Sendai (Japan), 2017.

[111] R. Bonifetto, A. Brighenti, L. Savoldi and R. Zanino, "Coupling superconducting magnet and refrigerator thermal-hydraulic models for nuclear fusion applications," in *International Cryogenic Engineering Conference*, Oxford (UK), 2018.